A NOVEL 3D TRANSCRANIAL COLOR DOPPLER SYSTEM: TOWARDS STROKE RISK ASSESSMENT

LI SHUAI

PhD

The Hong Kong Polytechnic University

2024

The Hong Kong Polytechnic University
Department of Biomedical Engineering

A Novel 3D Transcranial Color Doppler System: Towards Stroke Risk Assessment

Li Shuai

A thesis submitted in partial fulfillment of the requirements for the degree of Doctor of Philosophy

December 2023

CERTIFICATE OF ORIGINALITY

I hereby declare that this thesis is my own work and that, to the best of my knowledge and belief, it reproduces no material previously published or written, nor material that has been accepted for the award of any other degree or diploma, except where due acknowledgment has been made in the text.

_____(Signed)

LI Shuai (Name of Student)

Abstract

Stroke, being the second most prevalent cause of mortality on a global scale, presents a significant threat to approximately one-quarter of the world's population, potentially posing risks of crippling and lasting disability. The Circle of Willis (CoW) is an essential anatomical structure that plays a crucial role in maintaining a consistent and uninterrupted blood flow to the brain, hence serving as a protective mechanism against the occurrence of stroke. Among the available imaging modalities, transcranial color-coded Doppler (TCCD) has gained increasing popularity in clinical settings owing to its cost-effective and radiation-free nature for assessing potential obstructions inside the CoW. Recently, 3D TCCD was developed to address the inherent limitations of 2D TCCD; examples include 3D power Doppler imaging and 3D color flow imaging.

Nevertheless, these existing 3D approaches still suffer from certain limitations, either in terms of a deficient rate of vascular recognition or the lack of hemodynamic information. Besides, the issue of color overrepresentation is a significant obstacle to achieving anatomical precision in 3D TCCD. On top of that, there exist scarce studies on 3D TCCD reporting any quantitative difference in transcranial 3D reconstruction, which might indirectly imply a lack of confidence in the accuracy of the reconstructed objective. All of them are crucial in the context of precision medicine.

In Chapter 2, we developed a novel 3D TCCD imaging system, called ultrasound brain angiography (UBA), using a commercial single-crystal phased array transducer to improve the Doppler sensitivity and an advanced color mode of directional color power imaging (dCPI) that integrates good sensitivity and the directional information. Subsequently, this new system was

adopted for the following three chapters, with an overall objective to determine the feasibility and clinical values of UBA. In Chapter 3, the developed UBA system was tested on vascular phantoms, where the UBA system was used to investigate the influences of several factors, including vascular diameter, flow velocity, Doppler interrogation depth, and settings of color gain and velocity scale, on the occurrence of color overrepresentation in 3D displays. In Chapter 4, the developed UBA system was evaluated on healthy older adults in aspects of CoW vascular detection rate and its capacity to capture hemodynamics. In Chapter 5, the structural similarity of the reconstructed UBA images was compared against the gold standard of magnetic resonance angiography (MRA) on human subjects.

In summary, the UBA system was successfully developed and tested on phantoms and human subjects. It was found to outperform the existing 3D TCCD techniques in aspects of vascular detection rate, with a high structural similarity agreement of CoW compared with the standard MRA. Apart from this, it offers CoW hemodynamic information, including blood flow direction and velocity, potentially assisting clinicians in assessing the presence of blood flow abnormalities. Overall, the findings of this study are of great value in enhancing the diagnostic performance of current 3D TCCD ultrasound imaging for assessing CoW integrity and, hence, pave the way towards stroke risk assessments in patients in the long run.

Publications and Intellectual Property Arising from the Thesis

Journal papers:

[1] **S. Li**, Q. T. K. Shea, Y. T. Ling, and Y. P. Zheng, "Investigation of 3D Vessel Enlargement under Doppler Imaging with Phantoms: Towards Reconstruction of Circle of Willis," Ultrasonics, 2024. doi: 10.1016/j.ultras.2024.107332. Accepted.

[2] **S. Li**, C. P. Y Wan, Q. T. K. Shea, Y. T. Ling, X. Y. Chen, and Y. P. Zheng, "A Novel 3D Transcranial Color Doppler System Enhances Vascular Detection Rate with Hemodynamic Captures," Computers in Biology and Medicine, CIBM-D-23-13146. Submitted

Participated in Conference:

[1] **S. Li**, C. P. Y Wan, Q. T. K. Shea, Y. T. Ling, X. Y. Chen, and Y. P. Zheng. "A Novel 3D Transcranial Color Doppler System Enhances Vascular Detection Rate with Hemodynamic Captures," HKIE Biomedical Engineering Conference BME2023, 2023. (Oral presentation)

[2] **S. Li**, Q. T. K. Shea, Y. T. Ling, and Y. P. Zheng, "Development and Verification of a 3D Ultrasound Imaging System for the Cerebral Arteries," PAIR Annual Conference 2023, 2023. (Poster presentation)

Intellectual property:

[1] **S. Li**, Q. T. K. Shea, and Y. P. Zheng, "经颅超声应用装置," 202310572635.8, 19 May 2023. (PCT/CN2023/095361)

[2] Q. T. K. Shea, **S. Li**, and Y. P. Zheng, "头部超声图像的生成方法、装置、终端设备及存储介质," 202310980516.6, 4 Aug 2023. (PCT/CN2023/111289)

Other Publications and Intellectual Property Co-authored During the Ph.D. Study

Journal papers:

[1] H.Y. Kang, W. Zhang, **S. Li**, X.Y. Wang, Y. Sun, X Sun, F.X. Li, C Hou, S.K, Lam, and Y. P. Zheng, "A Comprehensive Benchmarking of A U-Net based Model for Midbrain Auto-segmentation on Transcranial Sonography," Computer Methods and Programs in Biomedicine, CMPB-D-23-03494. Submitted

[2] P. Palanisamy, **S. Li** (Co-first author), Q. T. K. Shea, M. M. C. Li, L. W. H. Cheung, L. Qin, S. K. H. Chow, and Y. P. Zheng, "Characterization of LIPUS Parameters Suitable for Hip Bone Fracture," Ultrasound in Medicine & Biology, UMB-D-23-00778. Submitted

[3] P. Palanisamy, M. Alam, **S. Li, S**. K. H. Chow, and Y. P. Zheng, "Low-Intensity Pulsed Ultrasound Stimulation for Bone Fractures Healing: A Review," Journal of Ultrasound in Medicine, vol: 41, no: 3, pp: 547-563, March 2022. doi: 10.1002/jum.15738.

[4] R. T. L. Zhu, P. Z. Lyu, **S. Li**, C. Y. Tong, Y. T. Ling, and C. Z. H. Ma, "How Does Lower Limb Respond to Unexpected Balance Perturbations? New Insights from Synchronized Human Kinetics, Kinematics, Muscle Electromyography (EMG) and Mechanomyography (MMG) Data", Biosensors, vol. 12, no. 6, p. 430, June 2022. doi: 10.3390/bios12060430.

[5] R. U. Ahmed, M. Alam, **S. Li**, P. Palanisamy, H. Zhong, and Y. P. Zheng, "A novel therapeutic approach of ultrasound stimulation to restore forelimb functions following cervical cord injury in rats," Journal of Neurorestoratology, vol. 11, no. 6, 10067, June 2023. doi: 0.1016/j.jnrt.2023.100067

[6] R. U. Ahmed, V. R. Edgerton, **S. Li**, Y. P. Zheng, and M. Alam, "Buspirone Dose-Response on Facilitating Forelimb Functional Recovery in Cervical Spinal Cord Injured Rats," Dose-Response, vol: 19, no: 1, 2021. doi: 10.1177/1559325821998136.

[7] **S. Li**, M. Alam, R. U. Ahmed, H. Zhong, X. Y. Wang, S. Ng, and Y. P. Zheng, "Ultrasound-driven piezoelectric current activates spinal cord neurocircuits and restores locomotion in rats with spinal cord injury," Bioelectronic medicine, vol. 6, no. 1, pp. 1-9, December 2020. doi: 10.1186/s42234-020-00048-2.

Intellectual property:

[1] **S. Li**, N. S. Tharu, and Y. P. Zheng, "一种控制康复训练的方法、控制装置及控制系统," 202310337623.7, 31 March 2023. (PCT/CN2023/085512)

[2] **S. Li**, Y. P. Zheng, M. Alam, and P. Palanisamy, "Bone Stimulator and Bone Stimulation System for Bone Fracture Healing", 16 Sep 2020. (PAT-1248 SFHK Ref: P21199PCT00)

Acknowledgments

I extend my sincere appreciation to my supervisor, Ir. Professor ZHENG Yongping, for his substantial encouragement and support throughout this work.

I would like to thank all the members of our research team, particularly Dr. Shea, Dr. Ling, and Dr. Lam for their suggestions and valuable comments, and Ms. Wan for her assistance with the experiments. I am also grateful to the subjects who graciously dedicated their time and patience throughout the subject test.

Finally, my family and my wife, Sun Yu, deserve my deepest gratitude for their support and care.

Table of Contents

List of Figures

List of Tables

List of Abbreviation

Abbreviation	Explanation
ACA	Anterior cerebral artery
ACoA	Anterior communicating artery
AHA	the American Heart Association
BOLD	Blood oxygen level-dependent
COM port	Communication port
CoW	Circle of Willis
CSF	Cerebrospinal fluid
CT	Computed tomography
CTA	Computed tomography angiography
CTP	CT perfusion
dCPI	Directional color power image
DSA	Digital subtraction angiography
ECG	Electrocardiogram
FDA	the Food and Drug Administration
fMRI	Functional MRI
ICA	Internal carotid arteries
IDE	Integrated Development Environment
ISF	Interstitial fluid
MCA	Middle cerebral artery
MRA	Magnetic resonance angiography
MRI	Magnetic resonance image
NSF	Nephrogenic systemic fibrosis
PAI	Photoacoustic imaging
PCA	Posterior cerebral artery
PCoA	Posterior communicating artery
PET	Positron emission tomography
PI	Pulsatility index
ROI	Region of interest
rpm	Revolutions per minute
SNR	Signal-to-noise ratio
SPECT	Single-photon emission computed tomography
TCCS/TCCD	Transcranial color (coded) sonography/Doppler
TCD	Transcranial Doppler
TE	Echo time
TIA	Transient ischemic attack
TR	Repetition time
UI	User interface
VS	Microsoft Visual Studio
VTK	Visualization Toolkit

Chapter 1 Introduction

1.1 Stroke

Stroke, as the second-leading cause of death, manifests in 12.2 million incident cases and 6.55 million deaths yearly (Feigin et al., 2021), and 25% of the population worldwide will suffer from stroke once in their lifetime (Feigin et al., 2022). In China, stroke causes approximately 1.6 million deaths each year (Li & Zhang, 2019), which puts an enormous disease burden on the healthcare system in that 3,010,204 inpatients with stroke were admitted to 1,853 tertiary care hospitals during 2018 (Wang et al., 2020). Stroke is the consequence of an interruption of blood flow to the brain, and subsequently the brain cells die due to the lack of oxygen supply.

1.1.1 Type of stroke

Based on the classic definition and characterization of stroke, stroke is mainly classified as ischemic stroke and hemorrhagic stroke (shown in **Figure 1-1**), where ischemic stroke is the more prevalent type that accounts for 87% of all stroke cases (Virani et al., 2021), and intracerebral hemorrhage is the more prominent type in hemorrhagic strokes (Xi et al., 2006). Ischemic stroke is the consequence of obstructed blood supply to the brain, which leads to brain cell death due to a lack of oxygen and nutrient supply. The obstruction of a blood vessel is pathophysiologically defined as focal cerebral, spinal, or retinal infarction (Sacco et al., 2013). Hemorrhagic stroke is caused by a ruptured blood vessel in the brain so that blood spills into the brain tissue and promotes brain cell death; it is categorized into intracerebral hemorrhage and subarachnoid hemorrhage according to the bleeding location in the brain, as intracerebral hemorrhage is bleeding into the

brain parenchyma, and subarachnoid hemorrhage is bleeding into the subarachnoid space (Sacco et al., 2013).

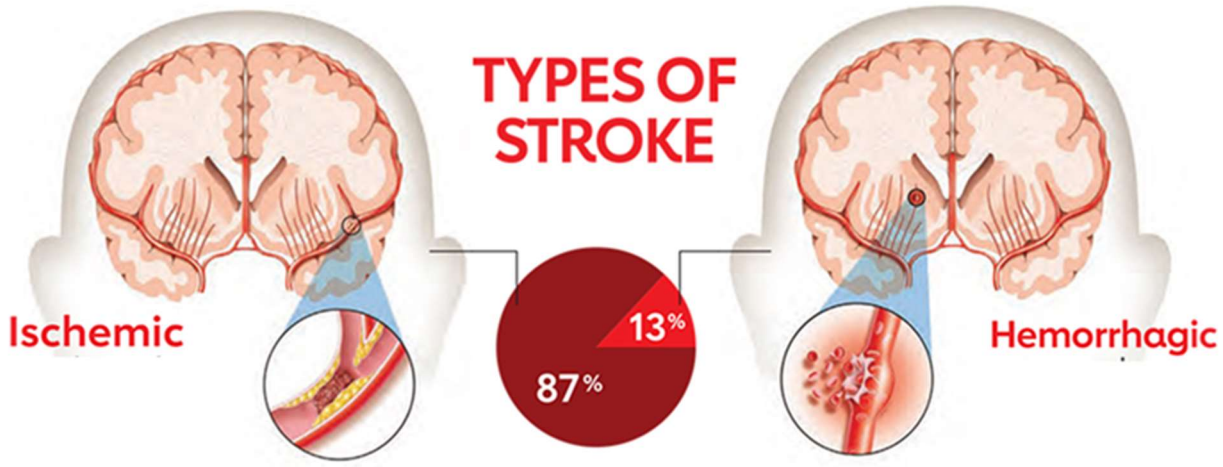

Figure 1-1. Types of stroke and their proportion (Virani et al., 2021).

In addition to the presence of ischemic and hemorrhagic stroke, the latest scientific statement of transient ischemic attack (TIA) was updated in 2009 (Easton et al., 2009). TIA is also named "mini-stroke" as it presents similar symptoms of a stroke but lasts for a relatively short time, and there is no acute infarction that may lead to a permanent brain injury. However, TIA should be treated as a warning of a future stroke because one-third of TIA sufferers eventually develop a stroke within one year (Khare, 2016).

1.1.2 Signs and symptoms of a stroke

Considering the limited public knowledge regarding stroke warning signs and their rapid recognition, the Brain Attack Coalition has created five warning signs, the "suddens", and the American Heart Association (AHA) uses it for public stroke education (Kleindorfer et al., 2007) (shown in **Figure 1-2**). The "suddens" include: **1.** Sudden numbness or weakness of the face, arm, or leg, especially on one side of the body; **2.** Sudden confusion, trouble speaking or understanding;

3. Sudden trouble seeing in one or both eyes; **4.** Sudden trouble walking, dizziness, loss of balance or coordination; **5.** Sudden severe headache with no known cause.

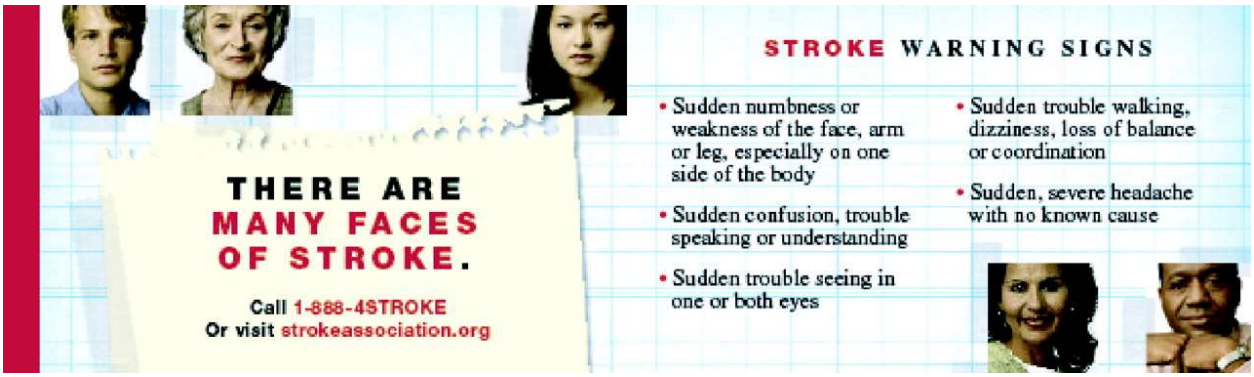

Figure 1-2. Five stroke warning signs, the "suddens", previously adopted by the AHA (Kleindorfer et al., 2007).

However, the contents of the "suddens" were too lengthy, and it was difficult for the general public to remember. In order to simplify the information, "FAST" was utilized to deliver three common warning signs and one action. "FAST" means **f**ace drooping, **a**rm numbness/weakness, **s**peech difficulty, and **t**ime to call an ambulance, and this idea was inspired by a study reported in 1999 (Kothari et al., 1999). The details of FAST are shown in **Figure 1-3**.

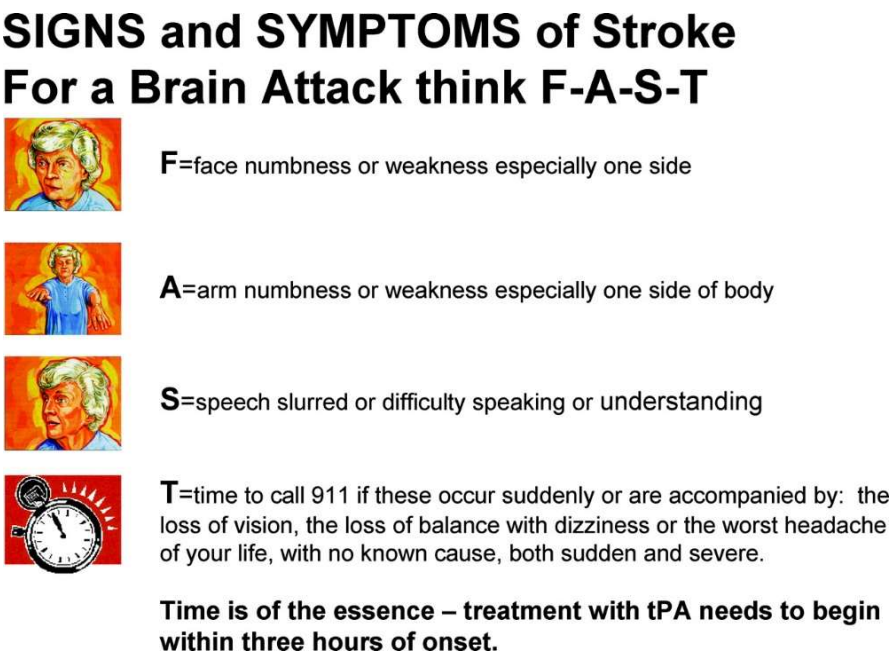

Figure 1-3. FAST for stroke warning signs (Kleindorfer et al., 2007).

1.1.3 Stroke syndromes

In fact, the symptoms of a stroke are complicated, and the combination of various clinical symptoms is called a syndrome. A specific syndrome of the stroke helps identify the injured part of the brain, and most stroke syndromes are related to the cerebral arteries (Balami et al., 2013), shown in **Table 1-1**.

Table 1-1. Stroke syndromes arranged by vascular territory. (Balami et al., 2013)

Types of arteries	Syndromes of stroke
Middle cerebral artery	Middle cerebral artery: complete Middle cerebral artery: superior division Middle cerebral artery: inferior division Gerstmann syndrome Ataxic hemiparesis
Posterior cerebral artery	Posterior cerebral artery: unilateral occipital Balint syndrome Cortical blindness (Anton syndrome) Weber syndrome Alexia without agraphia Thalamic pain syndrome (Dejerine–Roussy syndrome)
Anterior inferior cerebellar artery	Lateral pontine syndrome (Marie–Foix syndrome)
Posterior inferior cerebellar artery	Lateral medullary syndrome (Wallenberg syndrome)
Basilar artery	Locked-in syndrome Lateral pontine syndrome (Marie–Foix syndrome) Ventral pontine syndrome (Raymond syndrome) Ventral pontine syndrome (Millard–Gubler syndrome Inferior medial pontine syndrome (Foville syndrome) Ataxic hemiparesis Cortical blindness (Anton syndrome) Medial medullary syndrome (Dejerine syndrome)
Vertebral artery	Medial medullary syndrome (Dejerine syndrome) Lateral medullary syndrome (Wallenberg syndrome)
Anterior spinal artery	ASAS
Posterior spinal artery	PSAS

1.1.4 Risk factors and causes

Stroke is a heterogeneous syndrome; different pathogeneses of stroke indicate different risk factors. Identification of these factors is essential for prescribing appropriate and timely intervention strategies to reduce the risk of stroke and may provide efficient treatment after stroke (Members et al., 2012). In the past decades, researchers have studied and listed many stroke risk factors, and these factors are sorted into nonmodifiable risk factors and modifiable risk factors (Boehme et al., 2017; O'donnell et al., 2010), as indicated in **Table 1-2**. Nonmodifiable risk factors for both ischemic and hemorrhagic strokes are age, sex, race, and genetics. Age is the most important factor in that the stroke incidence doubles for every decade after 55 years old (Members et al., 2012). Even though the risk of gender still relies on age, women are more likely to develop a stroke at a young age, while men have a relatively higher risk of stroke when older (Kapral et al., 2005). Throughout the lifetime of an individual, women are at a greater risk of developing stroke than men because of their longer life span (Reeves et al., 2009). Hence, stroke is generally described as an aging disease. Racial disparities also influence the risk of stroke; for example, African Americans have been shown to exhibit a doubled risk of stroke incidence compared to white Americans (Cruz-Flores et al., 2011). As for genetics, it is nonmodifiable to consider the risk with regard to parental or family history (Seshadri et al., 2010), and it is potentially modifiable because of gene-environment interactions (Matarin et al., 2008).

Modifiable risk factors can be grouped as medical conditions and behavioral factors (Boehme et al., 2017), and some overlaps were found in ischemic and hemorrhagic strokes. The most important factor by far is hypertension (O'donnell et al., 2010). Relatively high blood pressure, even within the normal range, indicates a higher stroke risk (Stansbury et al., 2005). Although hypertension is more likely to contribute to hemorrhagic stroke, it can still induce ischemic stroke

by causing atherosclerotic disease. Meanwhile, hypertension is highly relative to age, as older people (aged >65) are mostly diagnosed as hypertensive (Chobanian, 2003). Diabetes mellitus is identified as an independent risk factor (Boehme et al., 2017). Diabetic or prediabetic patients have a high risk of stroke, and the duration of the diabetes mellitus also increases the risk of stroke (Banerjee et al., 2012; Sui et al., 2011). In an attempt to reduce the risk of stroke caused by diabetes mellitus, behavioral change plus medical therapy is recommended rather than just using glycemic control because glycemic control alone does not help decrease the risk (Anselmino et al., 2008; Gæde et al., 2008; Gray et al., 2007; Holman et al., 2008). Smoking, diet, waist-to-hip ratio (indicating body weight or obesity) and alcohol consumption are associated with an increased risk of stroke and interact with other factors, such as hypertension and diabetes mellitus (Appel et al., 2006; Lu et al., 2014; Rantakömi et al., 2013; Strazzullo et al., 2009; Suk et al., 2003; Thun et al., 2000; Wannamethee & Shaper, 1996). Additionally, exposure to secondhand smoke can also increase the risk of stroke (Malek et al., 2015). There are some differences in the modifiable risk factors among ischemic stroke because more etiological subtypes represent more causes of ischemic stroke (Adams Jr et al., 1993), while hemorrhagic strokes can be either due to intracerebral hemorrhage or subarachnoid hemorrhage. Moreover, it was reported that around one-third of ischemic strokes are cryptogenic because of unknown causes (Kleindorfer et al., 2021).

Table 1-2. Nonmodifiable and modifiable risk factors of stroke. (Boehme et al., 2017)

Type of stroke	Nonmodifiable risk factors	Modifiable risk factors
Ischemic stroke	Age Sex Race/ethnicity Genetics	Hypertension Current smoking Waist-to-hip ratio Diet Physical inactivity Hyperlipidemia Diabetes mellitus Alcohol consumption Cardiac causes Apolipoprotein B to A1 Genetics
Hemorrhagic stroke	Age Sex Race/ethnicity Genetics	Hypertension Current smoking Waist-to-hip ratio Alcohol consumption Diet Genetics

1.2 Cerebral vasculature

Cerebral vasculature consists of arterial, capillary, and venous systems, which assure constant brain perfusion and a sufficient supply of oxygen and nutrients to the brain cells (Agarwal & Carare, 2021). The cerebral arterial system mainly supplies oxygenated blood and nutrients to the brain cells, and it contains 15-20% of cardiac output (Xing et al., 2017). The network of cerebral arteries has a unique anatomy. The arterial blood passing through the paired internal carotid arteries (ICA) supplies the anterior brain, and the brainstem and posterior brain are supplied by vertebral arteries. If any blockage occurs in the supply arteries, the Circle of Willis (CoW) interconnects the anterior and posterior cerebral circulations to provide an alternative circulation path to the brain (Chandra et al., 2017). The details are shown in **Figure 1-4**. In addition to the

function of oxygen and nutrient supply, the perivascular spaces of cortical arteries also provide a pathway to drain interstitial fluid (ISF) (Agarwal & Carare, 2021).

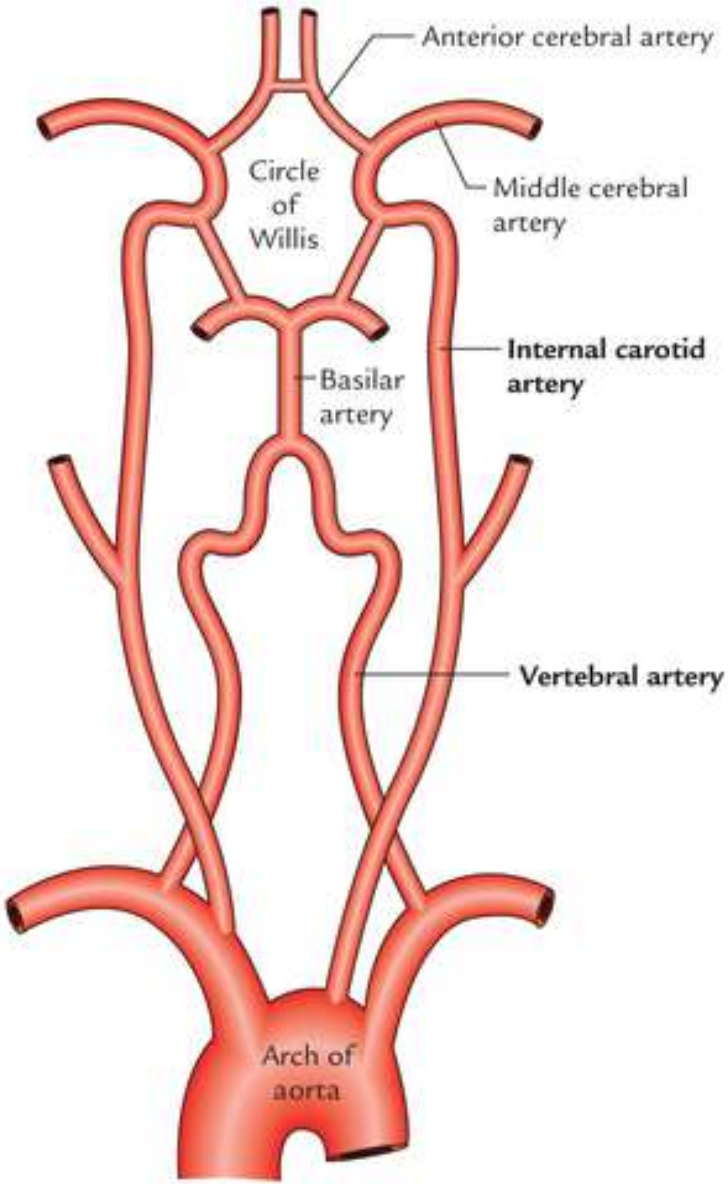

Figure 1-4. Main cerebral arteries for cerebral circulation. (https://neupsykey.com/blood-supply-of-the-brain-3/)

Cerebral capillaries and the venous system are important sites for circulation (production, absorption, and drainage) of ISF and CSF, where arterial blood, venous blood, cerebrospinal fluid (CSF), and interstitial fluid (ISF) are the four extracellular fluids in the brain (Agarwal et al., 2019).

1.2.1 The Circle of Willis (CoW)

Thomas Willis gave the first detailed description of this unique anatomy in 1664; it was, therefore, named as the Circle of Willis (Cavalcanti et al., 2009). The function of the CoW is well known for maintaining cerebral blood flow to the brain even if occlusion or stenosis occurs in the cerebral arteries (Chandra et al., 2017). In this case, the CoW may play an important role in reducing the incidence of stroke events. The structure of the CoW includes: middle cerebral arteries (MCAs), internal carotid arteries (ICAs), anterior cerebral arteries (ACAs), posterior cerebral arteries (PCAs), posterior communicating arteries (PCoAs), and anterior communicating artery (ACoA) (Rosner et al., 2018), as illustrated in **Figure 1-5**. ACA and PCA have multiple segments, A1-A5 for ACA and P1-P4 for PCA. A1 to A5 are pre-communicating, post-communicating, precallosal, supracallosal, and postcallosal segments, respectively (Kakou et al., 2000; Perlmutter & Rhoton, 1978). P1 to P4 are pre-communicating, post-communicating, quadrigeminal, and cortical segments (Cereda & Carrera, 2012). The anatomical structures are shown in **Figure 1-6** and **Figure 1-7**, and A1, A2, P1, and P2 are primary segments in the CoW.

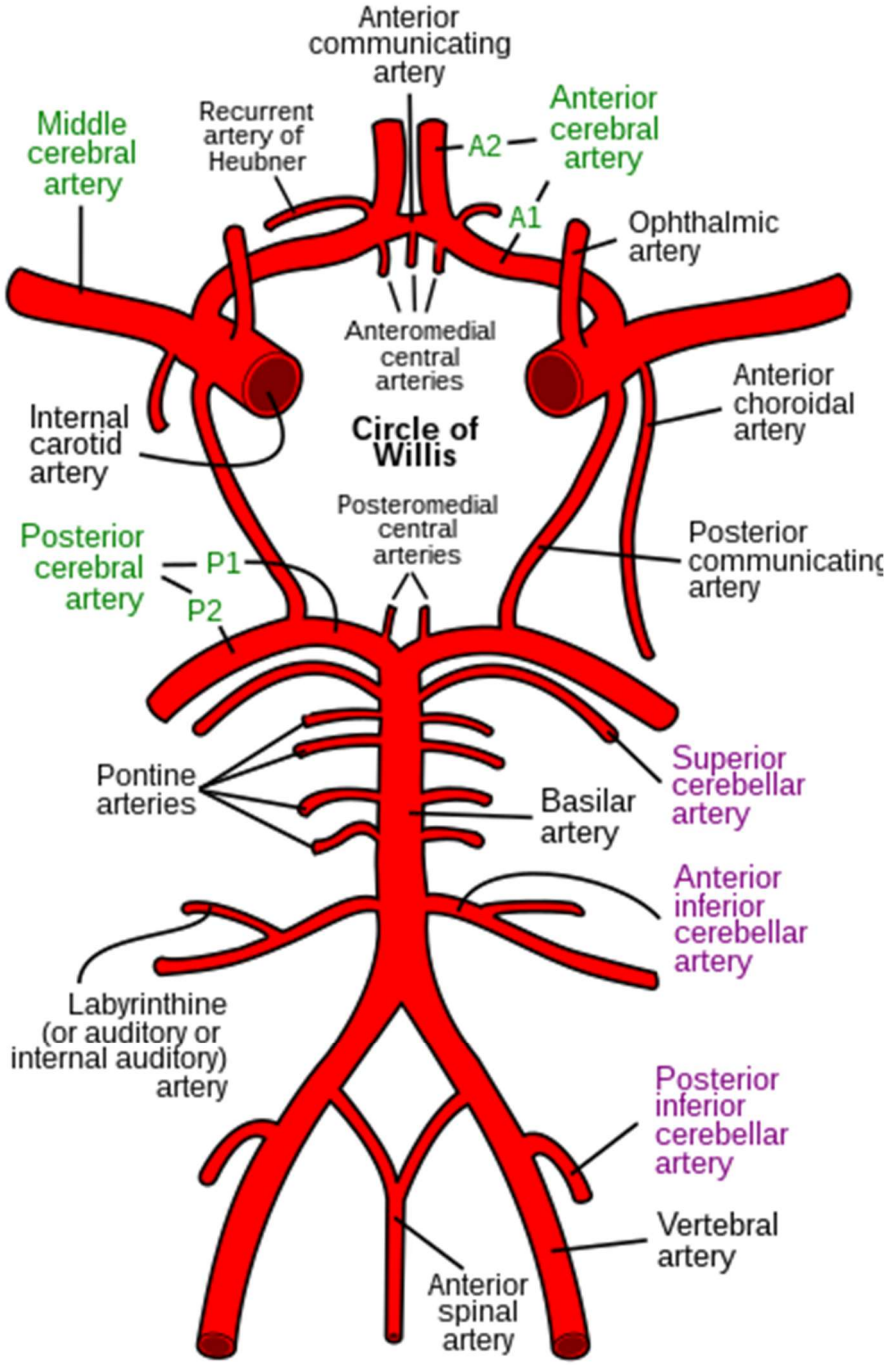

Figure 1-5. The anatomy and embryology of brain arterial circulation. (https://en.m.wikipedia.org/wiki/File:Circle_of_Willis_en.svg)

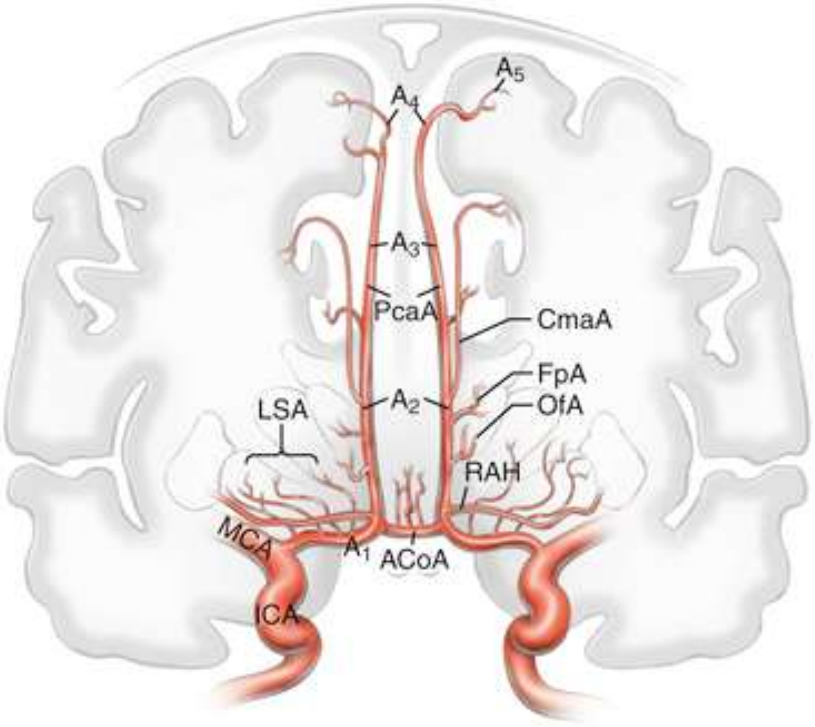

Figure 1-6. Segments in ACA, A1-A5. (https://neupsykey.com/anterior-communicating-artery-aneurysms-2/)

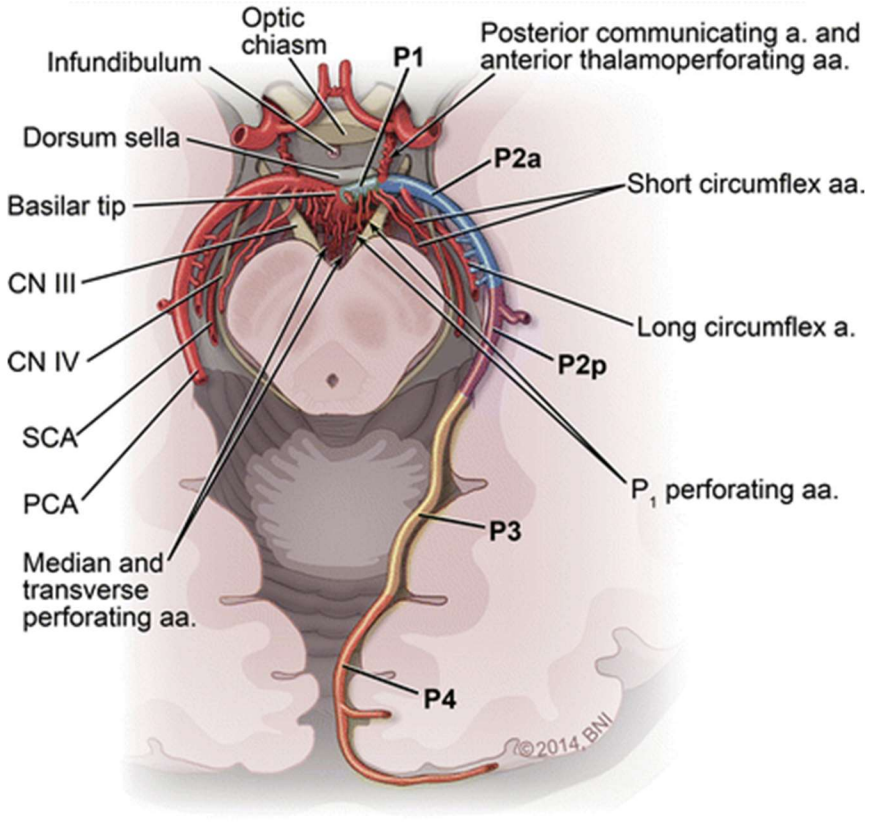

Figure 1-7. Segments in PCA, P1-P4. (https://neupsykey.com/microsurgical-management-of-posterior-fossa-vascular-lesions/)

1.2.2 Variations of CoW and stroke

A CoW with an intact anatomical structure can help redistribute the blood flow to maintain adequate cerebral perfusion. However, it was reported in 1998 that only 21% of people had a complete CoW (Krabbe-Hartkamp et al., 1998), and only 34.5% of cases were detected with classic anatomy of the CoW in 1,413 brains (Bergman et al., 2005). Some studies also reported the percentage values of incomplete CoW by investigating in different countries (De Silva et al., 2009; Li et al., 2011; Maaly & Ismail, 2011; Nordon David & Rodrigues Junior, 2012; Riggs & Rupp, 1963), as shown in **Table 1-3**. The anatomic variation of the CoW is classified as hypoplastic and absent, and one standard to consider hypoplasia of components in the circle is arteries less than 1 mm and communicating arteries less than 0.5 mm (Vrselja et al., 2014), while another is 0.8 mm as the general threshold to judge the hypoplasia in no matter what type of artery it is (Banga et al., 2018). Multiple variants have been found in the anterior and posterior parts of the CoW (**Figure 1-8**), and if the segments are absent in both anterior and posterior parts, the MCA would be isolated without any interconnection (**Figure 1-9**).

Table 1-3. The completeness of the Circle of Willis

Population	Method	Sample size (N)	Incomplete (%)
China (Li et al., 2011)	Autopsy	170	73.0
Egypt (Maaly & Ismail, 2011)	CT	250	53.3
Sir Lanka (De Silva et al., 2009)	MRA	225	85.5
Brazil (Nordon David & Rodrigues Junior, 2012)	Autopsy	50	54.0
USA (Riggs & Rupp, 1963)	Autopsy	994	80.7

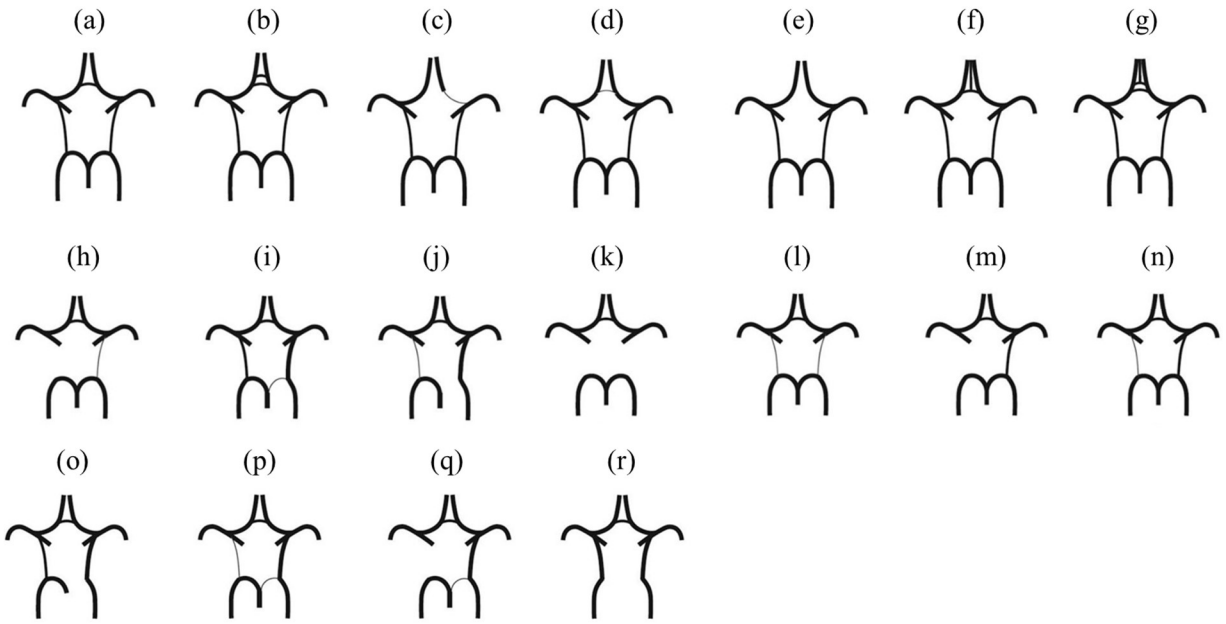

Figure 1-8. Variations of anterior and posterior parts of the CoW (Forgo et al., 2018). (a) normal structure (b) two ACoAs (c) unilateral hypoplasia of ACA A1 (d) hypoplasia of ACoA. (e) absence of ACoA (f) medial artery of the corpus callosum arising from ACoA. (g) medial artery of the corpus callosum arising from ACoA with two ACoAs. (h) hypoplasia of PCoA on one side, and absent contralateral PCoA. (i) hypoplasia of PCA P1. (j) absence of PCA P1 and hypoplasia of PCoA on the contralateral side. (k) bilateral absence of PCoAs. (l) bilateral hypoplasia of PCA P1. (m) unilateral absence of PCoA. (n) unilateral hypoplasia of PCoA. (o) unilateral absence of PCA P1 (p) hypoplasia of PCoA and hypoplasia of PCA P1 on the contralateral side. (q) absence of PCoA and hypoplasia of PCoA on the contralateral side. (r) bilateral absence of PCA P1.

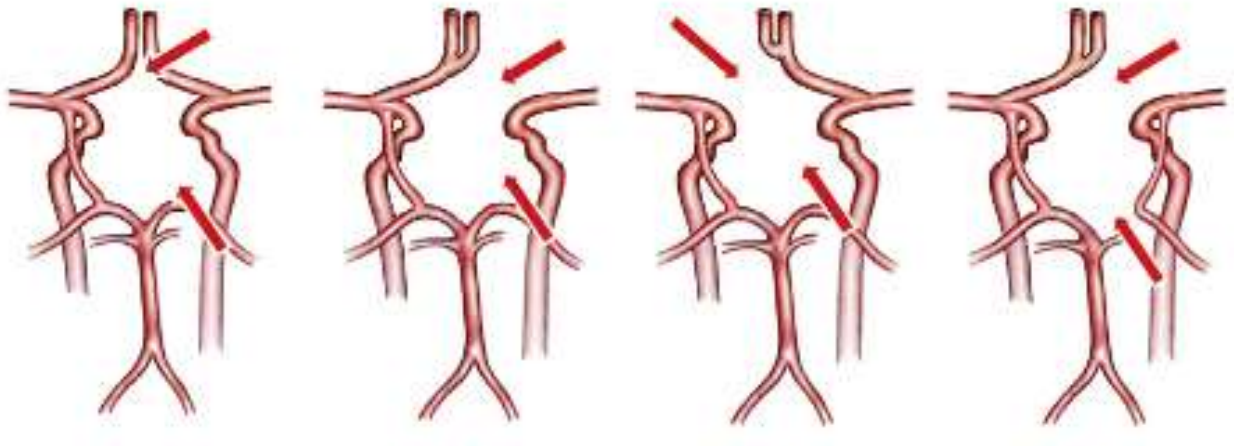

Figure 1-9. Four most frequent types of isolated MCA.

Recently, a comparatively high prevalence of variants was detected in stroke patients (De Caro et al., 2021), and the variants may also be associated with intraplaque hemorrhage of carotid plaques (Zhou et al., 2018). The relation between the completeness of the CoW and the risk of

ischemic stroke was studied in 2015, and it was reported that the variants occurring in both anterior and posterior parts of the CoW are related to future anterior circulation stroke (van Seeters et al., 2015). Hence, an incomplete circle may be an independent risk factor for stroke.

1.3 Imaging modalities for stroke screening (clinical or preclinical use)

The brain is the most sophisticated and complex organ in the human body and controls most activities. To better understand the structural and hemodynamic information of cerebral arteries, several existing imaging techniques are reviewed in this section.

1.3.1 MRI-related imaging modalities (MRA and fMRI)

MRI is a common imaging modality to diagnose and manage stroke (Burgess & Kidwell, 2011), and some related applications, such as magnetic resonance angiography (MRA) and functional MRI (fMRI), have been applied for stroke assessment. MRA is classified as contrast-enhanced MRA and non-contrast MRA, where contrast-enhanced MRA requires injection of a contrast agent while non-contrast MRA does not (Edelman & Koktzoglou, 2019). Contrast-enhanced MRA was first introduced in 1994 with the use of the gadolinium-based contrast agent (Prince, 1994), and the agent was claimed to be entirely safe even at double and triple doses (Hany et al., 1998). However, a study overturned the belief and linked the gadolinium-based contrast agent to nephrogenic systemic fibrosis (NSF) in 2006 (Grobner, 2006). In 2007, the U.S. Food and Drug Administration (FDA) even applied a black box warning on the gadolinium-based contrast agent (US-FDA, 2007). A replaceable contrast agent (ferumoxytol) was studied to show a great improvement in contrast-enhanced MRA (Hope et al., 2015; Li et al., 2005), but the cost was still high and has not received FDA approval yet. Although contrast-enhanced MRA provides excellent

image quality, the cost of contrast agents and safety issues have stimulated the clinical use of non-enhanced MRA over contrast-enhanced MRA. In fact, non-enhanced MRA has been reported for over three decades (Alfidi et al., 1987). However, its advancement has been hindered by the technological challenges in achieving a greater signal-to-noise ratio (SNR), faster and more powerful magnetic field gradients, and shorter echo time (TE) and repetition time (TR) (Wheaton & Miyazaki, 2012). Presently, the non-enhanced MRA is widely available for clinical use, which is known as the time of flight (TOF) sequence, but it exhibited a relatively lower diagnostic accuracy compared to the contrast-enhanced MRA in acute ischemic stroke (Boujan et al., 2018). Furthermore, the non-enhanced MRA still incurs high medical expenditure for patients even without the added cost of contrast agents, and there exists a poor synchronization of image acquisition with the timing of the blood flow that causes a loss of capturing slow blood flow (Edelman & Koktzoglou, 2019).

fMRI works as a gold standard of functional brain imaging that can measure blood oxygen level-dependent (BOLD) signals. The major principle of fMRI is the detection of changes associated with blood flow, on the ground that deoxygenated hemoglobin is paramagnetic and oxygenated hemoglobin is diamagnetic (Logothetis, 2008). fMRI has been studied to reveal and predict the recovery of motor cortices after therapeutic interventions (Dong et al., 2006; Lv et al., 2021; Ward et al., 2003).

1.3.2 CT-related imaging modalities (CTA and CT perfusion)

Computed tomography (CT) is another common imaging modality for stroke diagnosis and management (Kidwell & Wintermark, 2008). A CT scan can be conducted with or without a contrast agent or dye, which is also classified as contrast-enhanced and non-enhanced CT (Becks et al., 2019). In the evaluation of stroke, CT angiography (CTA) and CT perfusion (CTP) are the

two contrast-enhanced procedures for clinical use, and non-enhanced CT is generally used for emergencies (Aviv et al., 2007; Mousa et al., 2013). By contrast, CTA seems to be preferable for detecting severe stenosis in cerebral arteries, and CTP is more favorable for distinguishing between ischemia and infarction in the brain (Sabarudin et al., 2014). It is well-known that the benefits of CT scans are a relatively lower cost, shorter scan times, and higher spatial resolution. Despite this, the drawbacks of CT scans are huge. Exposure to ionizing radiation can cause a potential risk of cancer induction, although a reduced dose is suggested to be used after improvement (Lell et al., 2015). And iodinated contrast agents may exert side effects for patients with impaired renal function, which may in turn cause allergic reactions and tissue damage (Davenport et al., 2020). Moreover, vascular calcifications can cause substantial blooming artifacts, which may exaggerate the severity of stenosis (Ouwendijk et al., 2006).

1.3.3 Ultrasound-related imaging modalities (TCD, TCCD, and PAI)

Ultrasound-related diagnostic applications are popular owing to their non-invasiveness, good time resolution, excellent portability, and low-cost features. Among these applications, the transcranial Doppler (TCD) uses low-frequency pulsed ultrasound waves generated via a single-element transducer to detect the velocity of blood flow in the cerebral vessels, and the first successful trial of TCD was reported in 1982 (Aaslid et al., 1982). To ensure the penetration of ultrasound through the skull, three cranial windows, orbital, temporal, and foraminal windows, are utilized for the TCD examination (**Figure 1-10**). Measurements, including the peak systolic and diastolic velocities, mean flow velocity, resistive index (RI), and pulsatility index (PI), are routinely calculated and displayed on the TCD device (please refer to the typical ultrasound Doppler spectra in **Figure 1-11**). Hence, TCD is recommended as a useful tool for stroke management, and can be traced back to 1991 (Reutern, 1991). However, the inaccuracy of TCD

can be up to 20% (Sarkar et al., 2007). Although the targeted cerebral vessel can be identified by considering probe location, target depth, and flow direction, it could still be affected by the CoW variations or any parallel vessels with the same flow direction as the targeted vessel.

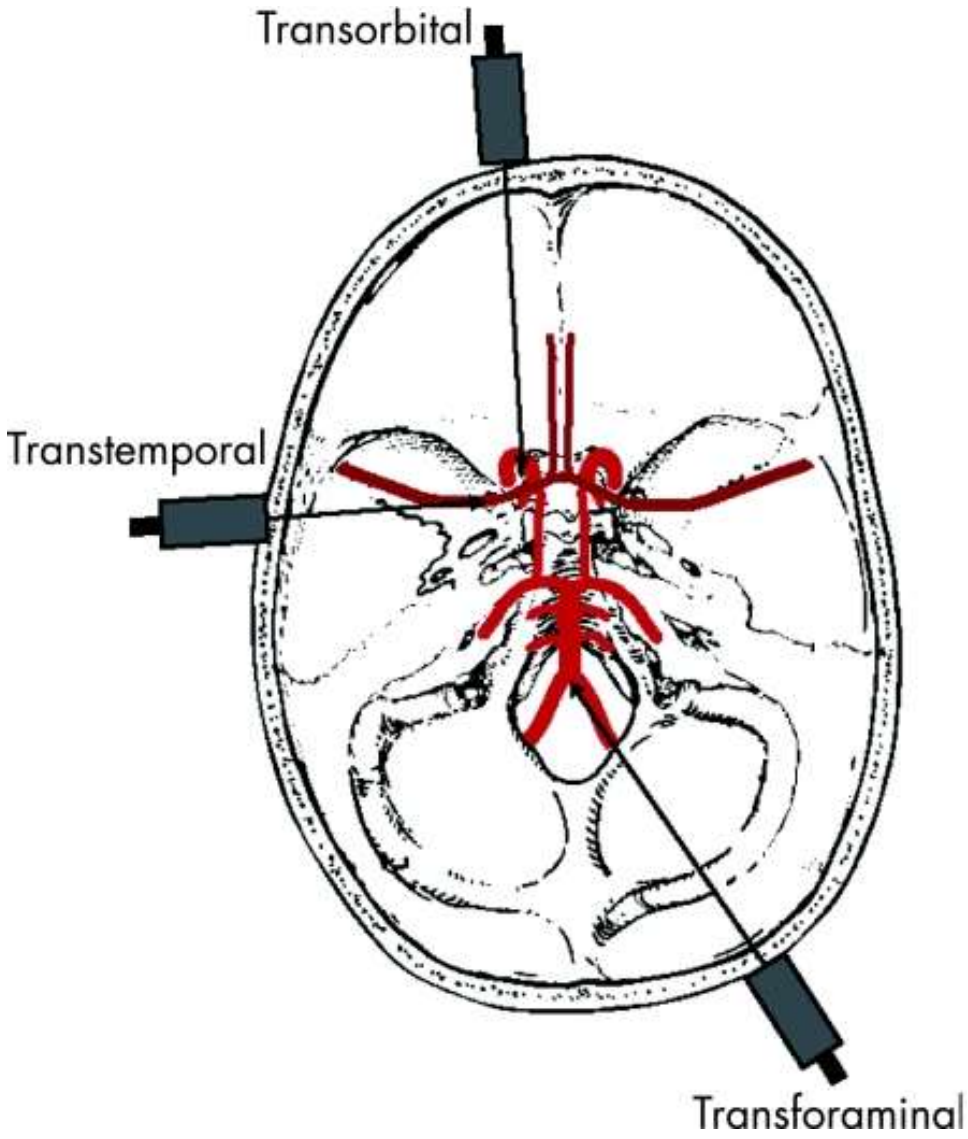

Figure 1-10. Three main windows to access the intracranial arteries (Sarkar et al., 2007).

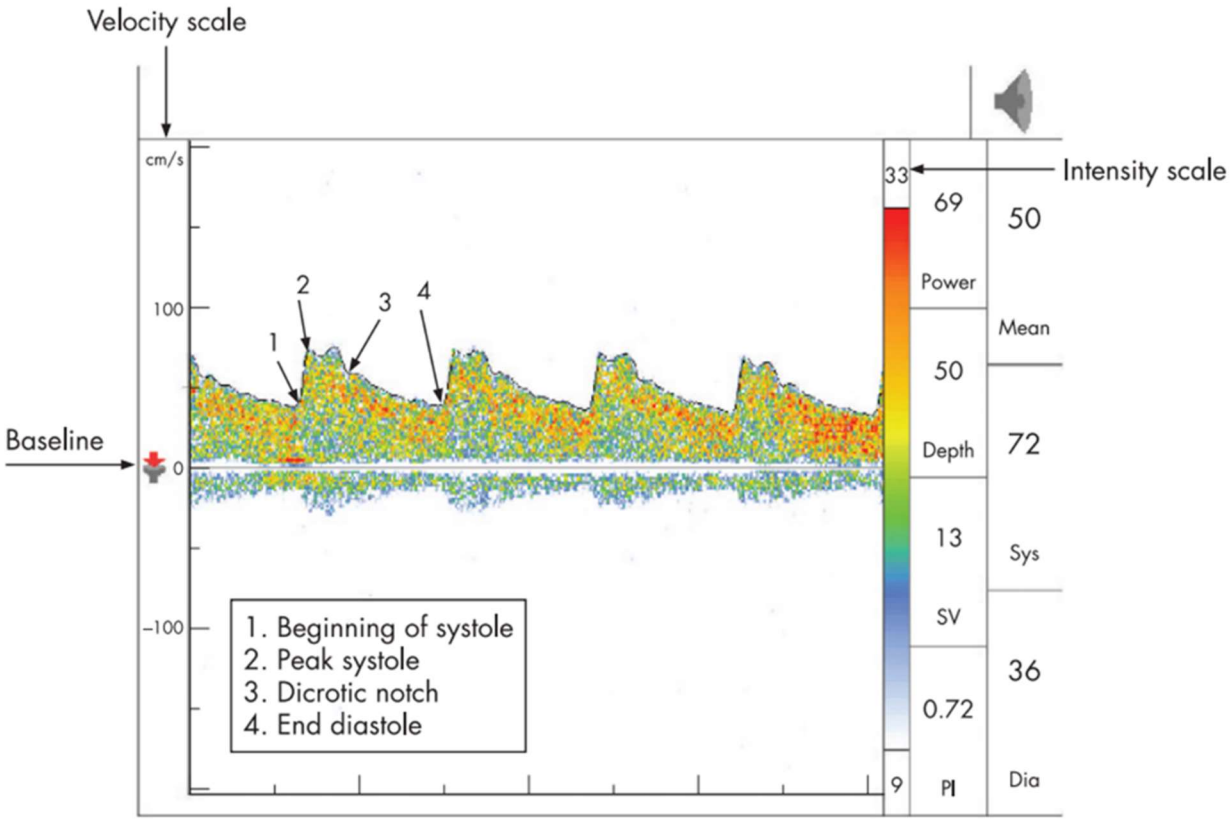

Figure 1-11. The typical Doppler spectra of TCD with velocity and intensity scale, and the related measurements are marked by the numbers (Sarkar et al., 2007).

Transcranial Color Doppler/Duplex sonography (TCCD/TCCS) is a technology combining the Doppler color image with the B-mode image to display the intracranial vascular structures, as illuminated in **Figure 1-12**. There are two standard modes of Doppler color imaging; one is color flow imaging (CFI), and the other is color power imaging (CPI) or power Doppler imaging (PDI). The color-coded images present different information of Doppler signal in different color imaging modes, as shown in **Figure 1-13**. The Doppler intensity is indicated in the power map by tracking the amplitude of the Doppler signal, while the Doppler spectrum is analyzed in the mode of CFI to encode the direction and velocity of the blood flow. Although the mode of CPI/PDI has a better ability to contain noise and is less affected by phase interference effects and angular cosine effects

(Kollmann, 2015), an absence of hemodynamic information about velocity and direction has largely impeded its clinical utility on TCCD.

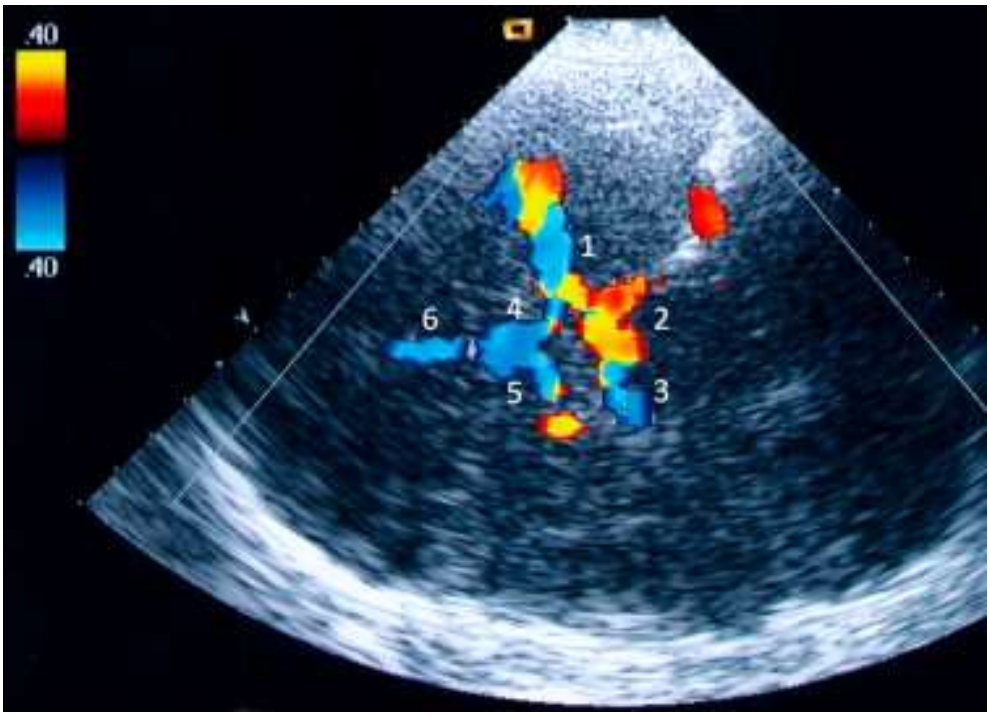

Figure 1-12. The typical image of TCCD, MCA=1, ipsilateral PCA=2, contralateral PCA=3, A1 segment of the ipsilateral ACA=4, A1 segment of the contralateral ACA=5 (Bartels, 2012).

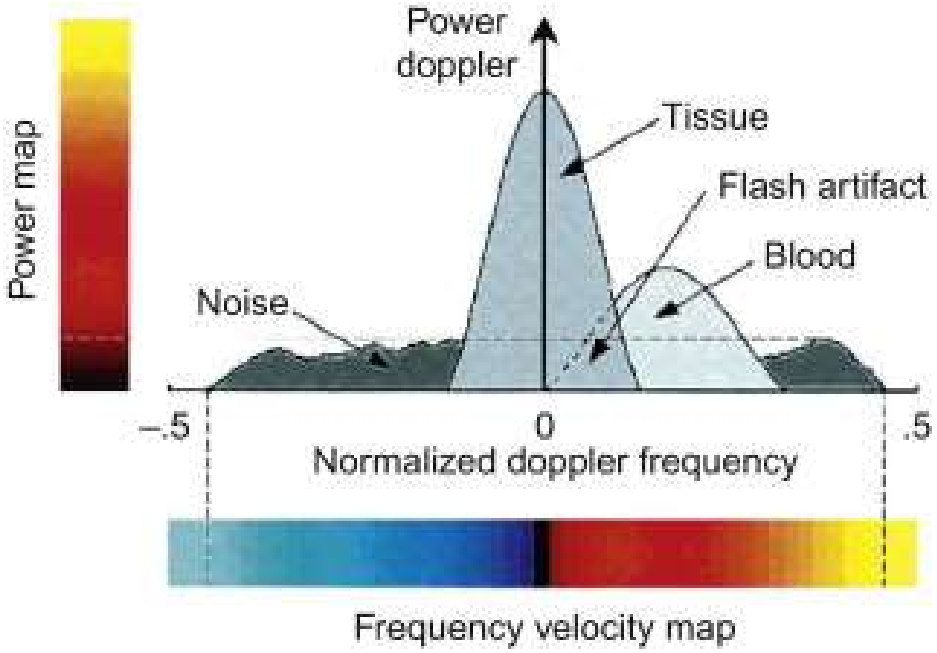

Figure 1-13. The color-coded images present different information of Doppler signal in different color imaging modes (Kollmann, 2015).

TCCD was developed in the late 1980s and was first used on adults in 1990 (Berland et al., 1988; Bogdahn et al., 1990; FURUHATA, 1989; Schöning et al., 1988). It demonstrates an advantage over conventional transcranial sonography in that cerebrovascular structures can be portrayed in the proper anatomical relationships to parenchymal structures. Similar to TCD, TCCD also needs to image the cerebral vessels through cranial windows. A low-frequency (1.6 MHz to 3.5 MHz) phased array ultrasound probe is generally attached to the cranial windows, and the imaging mode of CFI is used for TCCD (Zipper & Stolz, 2002). Since TCCD has a good ability to show the collaterals of the CoW (Hoksbergen et al., 2003), it has been applied in the clinic to image these vessels of the CoW at their anatomical location and indicate their hemodynamic captures. Certainly, TCCD can also be enhanced by injection of contrast agents (Baumgartner et al., 1997).

In stroke management, TCCD is reported to differentiate hemorrhagic stroke from ischemic stroke (Maurer et al., 1998). The role of TCCD in hemorrhagic stroke is to identify the location and size of intracranial hematomas, and it has even been reported to yield comparable accuracies to CT (Kukulska-Pawluczuk et al., 2012; Santamarina Pérez et al., 2009; Seidel et al., 1993). TCCD has also proved to be useful in detecting early hematoma expansion (Ovesen et al., 2014). Hence, TCCD is recommended as an alternative imaging modality when CTA or MRA is not readily available in stroke management (Olatunji et al., 2015). Moreover, TCCD has also been reported to diagnose, screen, treat, and prognosticate ischemic stroke (Allendoerfer et al., 2006; Baumgartner et al., 1999; Gerriets et al., 2000; Tang et al., 2005).

Photoacoustic imaging (PAI), also called optoacoustic or thermoacoustic imaging, is an emerging technique that irradiates a pulsed laser to the target tissue and then detects ultrasound signals from the imaged tissue to construct images (Xu & Wang, 2006). The generated ultrasound

signals are relative to the optical absorption coefficient of the tissue, and PAI requires a contrast agent for deeper structures (Fu et al., 2019). In fact, PAI is applicable to image blood vessels owing to the high optical absorption of blood hemoglobin and deoxyhemoglobin (Laviña, 2016). Although PAI has been used for stroke studies (Deng et al., 2012; Kneipp et al., 2014; Yang et al., 2021), it is still in the preclinical stage. After all, the main challenge is the high attenuation of the human skull.

1.3.4 Other imaging modalities (DSA, PET, and SPECT)

Digital subtraction angiography (DSA) is a fluoroscopy technique to visualize the structure of blood vessels by removing other surrounding tissues (Harrington et al., 1982). The fluoroscope unit with a radiological source, X-rays or MRI, is used to collect images before and after the injection of contrast medium, which are called pre-contrast images (mask images) and post-contrast images (Hentsch et al., 2003). Then, the interfering information can be removed by subtracting the mask image. DSA is the gold standard for diagnosing intracranial aneurysms because of its high resolution of 0.1 to 0.2 mm in the two-dimensional image (Brisman et al., 2006; Philipp et al., 2017). In addition, a 3D view of blood vessels can be obtained by rotational angiography (Anxionnat et al., 2001; Tanoue et al., 2000). Nevertheless, the disadvantages of DSA include the requirement of contrast medium and the nature of invasive intervention.

Positron emission tomography (PET) and single-photon emission computed tomography (SPECT) are molecular imaging techniques that can reveal the physiological processes in the brain (Lu & Yuan, 2015). The functional imaging generated by PET and SPECT has become an important part of multimodality imaging systems, such as PET/MRI, PET/CT, and SPECT/CT, to evaluate a variety of diseases (de Galiza Barbosa et al., 2016; Ell, 2006; Garrigue et al., 2016; Jadvar & Colletti, 2014; Schöder et al., 2003). Recently, PET was utilized to study ischemic stroke

by detecting the physiological processes under hypoxia and inflammation (Baskin et al., 2015; Heiss, 2014; Moraga et al., 2016).

1.4 Three-dimensional transcranial color Doppler (3D TCCD)

Among various imaging modalities, TCCD has been well adopted in clinics as a low-cost and radiation-free tool to examine the vascular normality in the CoW. Still, its lack of sufficient dimensional information is a major shortcoming compared with MRA and CTA. To acquire more spatial information, 3D Power Doppler Imaging (3D-PDI) (Bauer et al., 1998; Delcker & Turowski, 1997; Klötzsch et al., 1999; Klötzsch et al., 2002; Schminke et al., 2000) and 3D Color Flow Imaging via a 2D matrix array transducer (3D-CFI via a 2D-array transducer) (Ivancevich et al., 2008; Lindsey et al., 2009) have been developed to build a 3D view of the cerebral vessels in the CoW.

To obtain a real-time 3D image, the 3D-PDI generally uses a mechanical way of tilting a phased array ultrasound transducer to acquire 2D images through the temporal bone window, as shown in **Figure 1-14** (Delcker & Turowski, 1997). These 2D images are collected from different axial scanning planes, and a magnetic position sensor is assembled to the phased array ultrasound transducer to record the spatial orientation of the transducer in three dimensions (x, y, z axes). The assembled electromagnetic position sensor is an electromagnetic receiver in a composite magnetic field, which is generated by an array of three coils, and the transmitter is placed within one meter from the subjects (Delcker & Turowski, 1997). The data collection is conducted for 30-40 seconds, and 150 ultrasound images under the mode of PDI are captured. After the data collection, these images are off-line processed to extract the color-coded information and then reconstructed into a

3D view of the CoW according to the special information, as shown in **Figure 1-15** (Bauer et al., 1998).

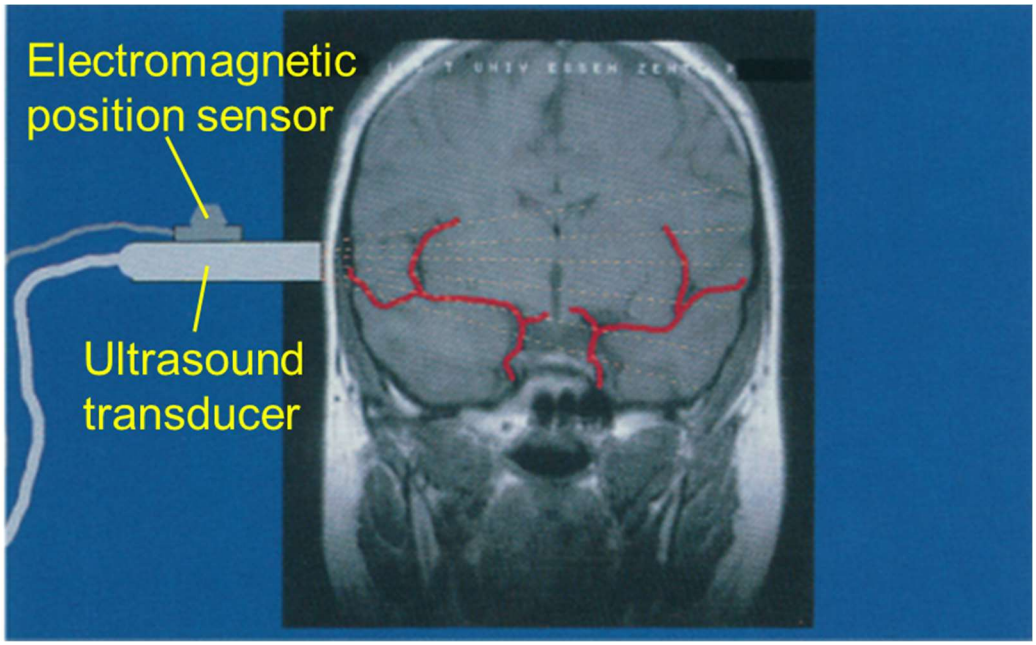

Figure 1-14. The scanning technique used for the data acquisition of 3D-PDI (Delcker & Turowski, 1997).

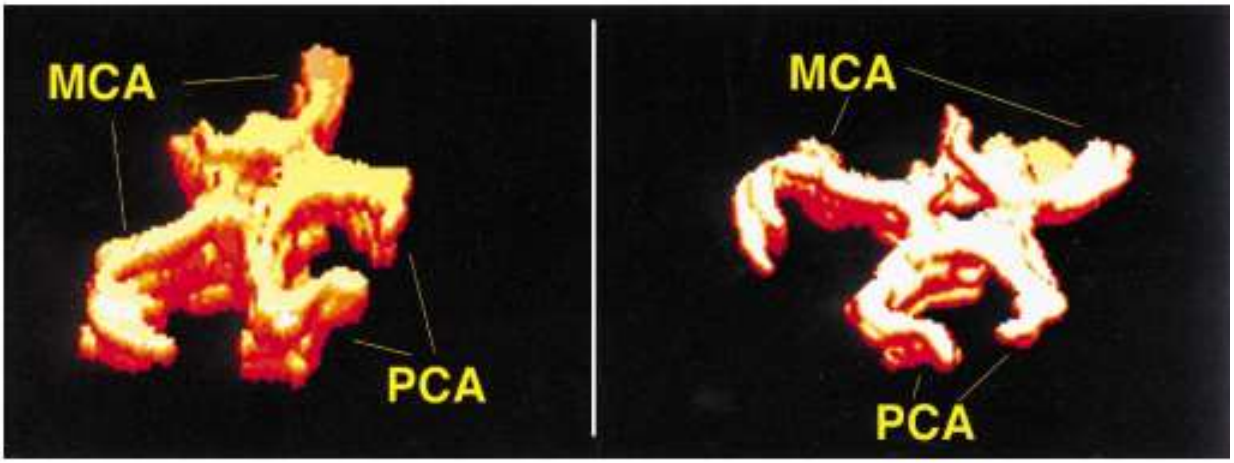

Figure 1-15. The three-dimensional view of the Circle of Willis generated by 3D-PDI with contrast enhancement (Bauer et al., 1998).

To evaluate the diagnostic value provided by 3D-PDI, Delcker and Turowski reported the visualization of some important cerebral arteries in the CoW (Delcker & Turowski, 1997). The detection rates of these vessels are listed in **Table 1-4** and **Table 1-5**. In their study, the proportions were separately analyzed on the ipsilateral and contralateral sides before and after the contrast

injection, where the ipsilateral and contralateral sides were referred to the insonated temporal bone window. The results demonstrated a greater visualization of vessels on the ipsilateral side, and the contrast agent could outstandingly enhance the performance of the 3D-PDI (Delcker & Turowski, 1997). Hence, some related studies in later years used the contrast-enhanced 3D-PDI to determine whether there was any structural change in the CoW, such as intracranial stenosis (Baumgartner et al., 1999; Klötzsch et al., 2002) and cerebral aneurysms (Klötzsch et al., 1999).

Table 1-4. The detection rate of cerebral arteries on the ipsilateral side of imaging with and without contrast agent (Delcker & Turowski, 1997).

Artery	Without Contrast (%)	With Contrast (%)	Difference (%)
MCA	90	100	10
ACA	90	100	10
PCA	60	100	40
PCoA	60	100	40

Table 1-5. The detection rate of cerebral arteries on the contralateral side of imaging with and without contrast agent (Delcker & Turowski, 1997).

Artery	Without Contrast (%)	With Contrast (%)	Difference (%)
MCA	30	80	50
ACA	60	90	30
PCA	20	100	80
PCoA	20	100	80

In the application of 3D-CFI via the 2D-array transducer, a 2D matrix array transducer operating at a central frequency of 2.5 MHz with 512 transmitters and 256 receiver channels is utilized to generate 3D ultrasound images under the imaging mode of CFI (Ivancevich et al., 2008). Analogous to the 1D array transducer, the principle of the 2D matrix array transducer is to obtain a volumetric scan by deriving the acoustic beam steering in azimuth and elevation dimensions (Yen et al., 2000). As illustrated in **Figure 1-16**, a pyramidal shape of a diverging beam is

generated by the 2D matrix array transducer, and then the volumetric echo and Doppler information is captured through the receiver channels for later offline processing and visualization of the cerebral vessels. In Ivancevich's study, a 65-degree pyramid was set to scan the temporal bone window for the subjects, and the reconstructed CoW is shown in **Figure 1-17** (Ivancevich et al., 2008).

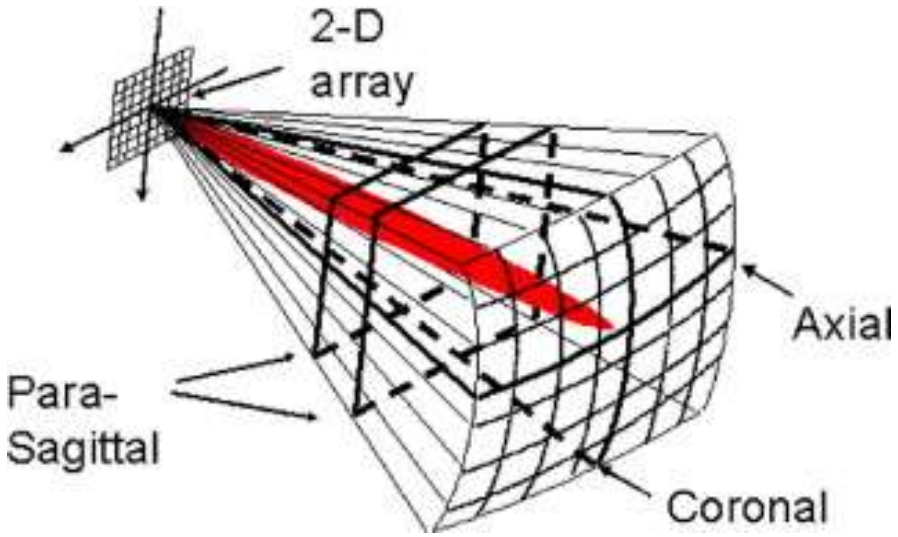

Figure 1-16. The principle of volumetric scan using the 2D matrix array transducer, as well as steerable spectral Doppler (red) (Ivancevich et al., 2008).

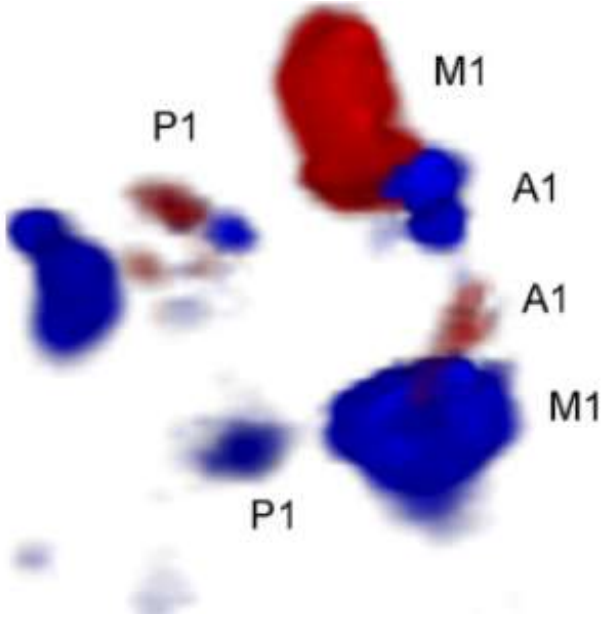

Figure 1-17. The three-dimensional view of the CoW generated by 3D-CFI via a 2D-array transducer (Ivancevich et al., 2008).

The detection rates of the cerebral vessels were also analyzed, and the percentages are listed in **Table 1-6**. The values of proportion were also separately analyzed on the ipsilateral and contralateral sides, where the ipsilateral and contralateral sides were referred to the insonated temporal bone window. The results analogously demonstrate a greater visualization of vessels on the ipsilateral side, but it may be difficult to detect the ICA and ACA-A2, even enhanced by the contrast injection.

Table 1-6. The enhanced detection rate of cerebral arteries on the ipsilateral side and contralateral side (Ivancevich et al., 2008).

Vessel	Detection rate* (%)	
	Ipsilateral side	Contralateral side
ICA	29.0	0
MCA	100.0	88.0
ACA-A1	88.0	71.0
ACA-A2	35.0	0
PCA-P1	82.0	71.0
PCA-P2	77.0	12.0

*Used the contrast agent

In the current clinical use, both structural and hemodynamic information is critical to assess the normality and integrity of the cerebral vessels using the conventional 2D TCCD. Although the techniques of 3D TCCD are rich in spatial information, they still suffer either from an inadequate vascular detection rate or lack of hemodynamic information. 3D-PDI is capable of delivering a clear visualization of the CoW, which is demonstrated in **Figure 1-15**, **Table 1-4**, and **Table 1-5**, as the detection rates of the cerebral vessels were higher than 80%. However, there are probably constraints on 3D-PDI using tilting scanning for data acquisition. Tilting scanning is one of the common mechanical ways to achieve 3D ultrasound imaging, as shown in **Figure 1-18**. Unlike the other two scanning methods, tilting scanning may give a non-isotropic resolution caused by diverse

imaging distances at the different tilt axes (Huang & Zeng, 2017). Meanwhile, the bounded tilting angle may restrict the 3D-PDI from a more integral visualization of the cerebral arteries, as the detection rates of ICAs are not included in the tables. Indeed, the main shortcoming of the 3D-PDI lies in the lack of hemodynamic information in the cerebral vessels, even though lightness may be used to identify the velocity of the blood flow. As for the 3D-CFI via a 2D-array transducer, the limitation seems to be an unsatisfactory Doppler sensitivity because of the undesirable values of enhanced detection rates compared with those of 3D-PDI.

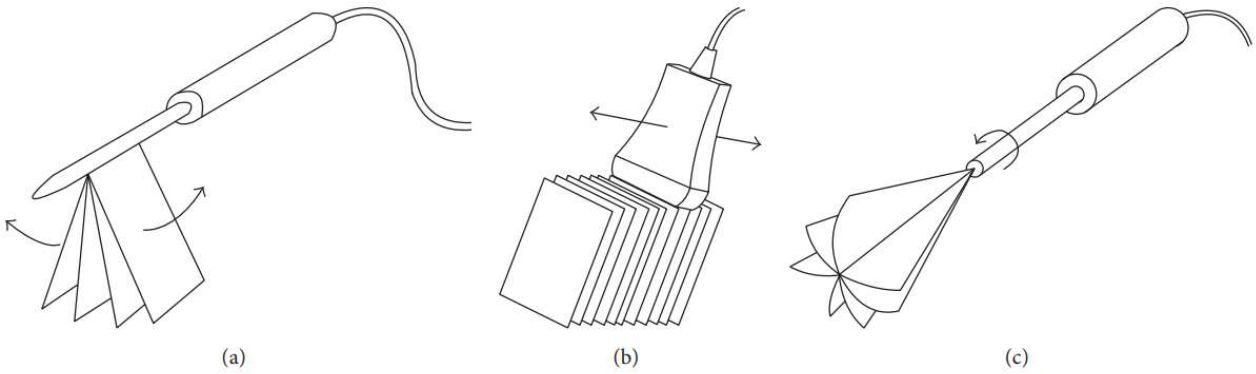

Figure 1-18. Three types of mechanical scanning: (a) tilting scanning; (b) linear scanning; (c) rotational scanning (Huang & Zeng, 2017).

On the other hand, the issue of color overrepresentation/enlargement presents a challenge to the anatomical precision depicted in TCCD, as shown in **Figure 1-19**. This may be attributed to the intricate path of ultrasound transmission within the skull and the relatively stronger Doppler signal resulting from the faster blood flow in the small cerebral vessels. This overrepresentation or enlargement can be controlled by various interrelated or separate elements, including imaging depth, transducer frequency, velocity scale, color gain, frame rate, and depth of Doppler interrogation, among others (Maulik, 2005). Meanwhile, CFI has poor noise containment compared with CPI/PDI, leading to a larger overrepresentation of color (Kollmann, 2015).

Similarly, a color overrepresentation/enlargement is seen in the 3D image; however, no analysis was conducted in these 3D TCCD studies.

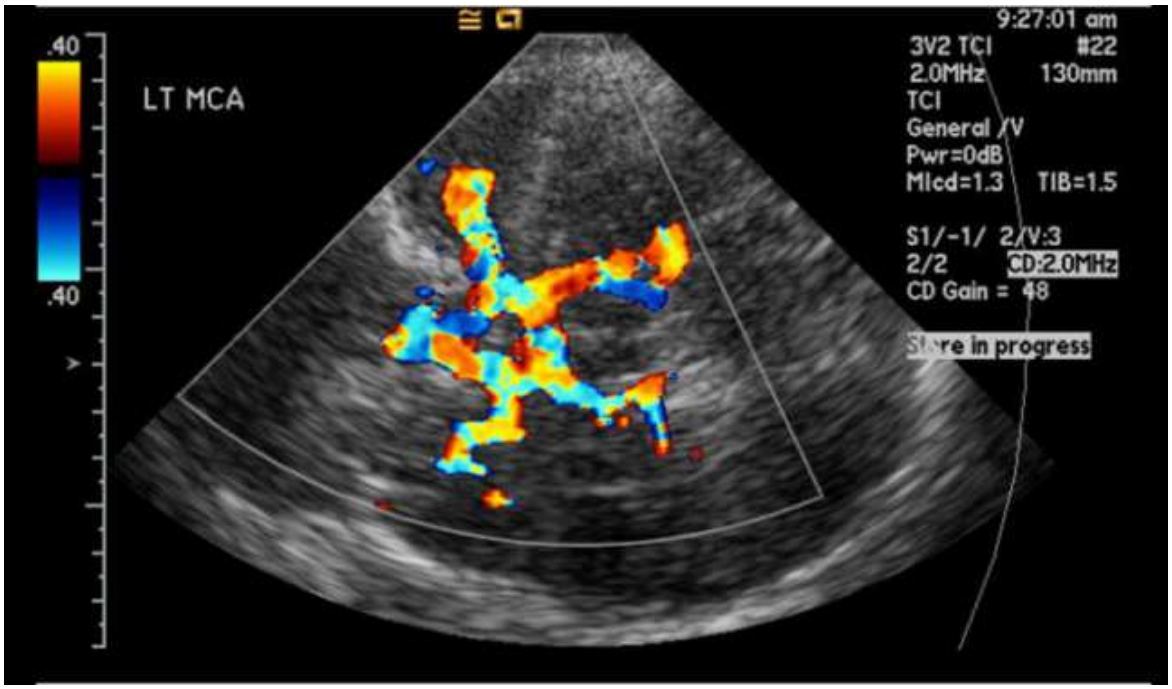

Figure 1-19. Conventional TCCD examination on fetus under CFI mode.

1.5 Aim and objectives

In summary, the existing 3D TCCD techniques, 3D-PDI and 3D-CFI via a 2D-array transducer, suffer either from a lack of hemodynamic information or inadequate vascular detection rates. Meanwhile, the issue of color overrepresentation/enlargement in 2D TCCD also exist in the 3D image. What is more, these 3D TCCD studies lacked quantitative analysis in regard to transcranial 3D reconstruction.

This proposed study aims to develop a new 3D TCCD imaging system called ultrasound brain angiography-UBA (**Chapter 2**) and to determine its feasibility and clinical values working

as a clinical application for stroke risk assessment (**Chapter 3-5**). The following are the objectives of this thesis:

- To figure out the effect of several factors, such as vascular diameter, flow velocity, Doppler interrogation depth, and settings of color gain and velocity scale, on the occurrence of color overrepresentation/enlargement in the 3D reconstruction generated by UBA. **(Chapter 3)**
- To determine the improved performance of the UBA system by evaluating its captured vascular detection rates and hemodynamic information, like the direction and velocity of the blood flow. **(Chapter 4)**
- To expose the quantitative difference in transcranial 3D reconstruction generated by UBA systems. **(Chapter 5)**

1.6 Summary

This chapter introduced the background information about stroke and reviewed most commonly used imaging modalities in stroke-related studies. Among these imaging modalities, conventional TCCD has been more frequently adopted in clinics as a low-cost and radiation-free tool to examine the normality and integrity of the cerebral vessels in the CoW. Still, it is limited by insufficient spatial information. The existing techniques of 3D TCCD can supplement more spatial information, but there are still some limitations of inadequate vascular detection rate, lack of hemodynamic information, few investigations on the phenomenon of overrepresentation/enlargement, and lack of quantitative analysis in transcranial 3D reconstruction. This thesis aims to address these issues by developing a new 3D TCCD imaging system (i.e., the UBA system) and to determine its feasibility and clinical value.

Chapter 2 System Development for 3D TCCD: Ultrasound Brain Angiography (UBA)

This chapter provides the details of the system development, which was later used for the experiment in **Chapter 3**, **Chapter 4**, and **Chapter 5**.

2.1 Overall structure of the system

Figure 2-1 indicates the systematic diagram of the developed ultrasound brain angiography UBA. The UBA imaging system includes two parts: hardware and software. The function of the hardware part is to collect the ultrasound color images for further 3D reconstruction. In this study, rotational scanning was used for data acquisition rather than tilting scanning, which can provide a more comprehensive view of imaging (Huang & Zeng, 2017). Also, a mode of directional color power imaging (dCPI) was applied to add directional information to the power imaging mode. Meanwhile, a single-crystal-made phased array transducer was utilized for better Doppler sensitivity. The software part is to establish 3D visualization by using some imaging processing methods and a customized algorithm of 3D reconstruction. The details of each part are described below.

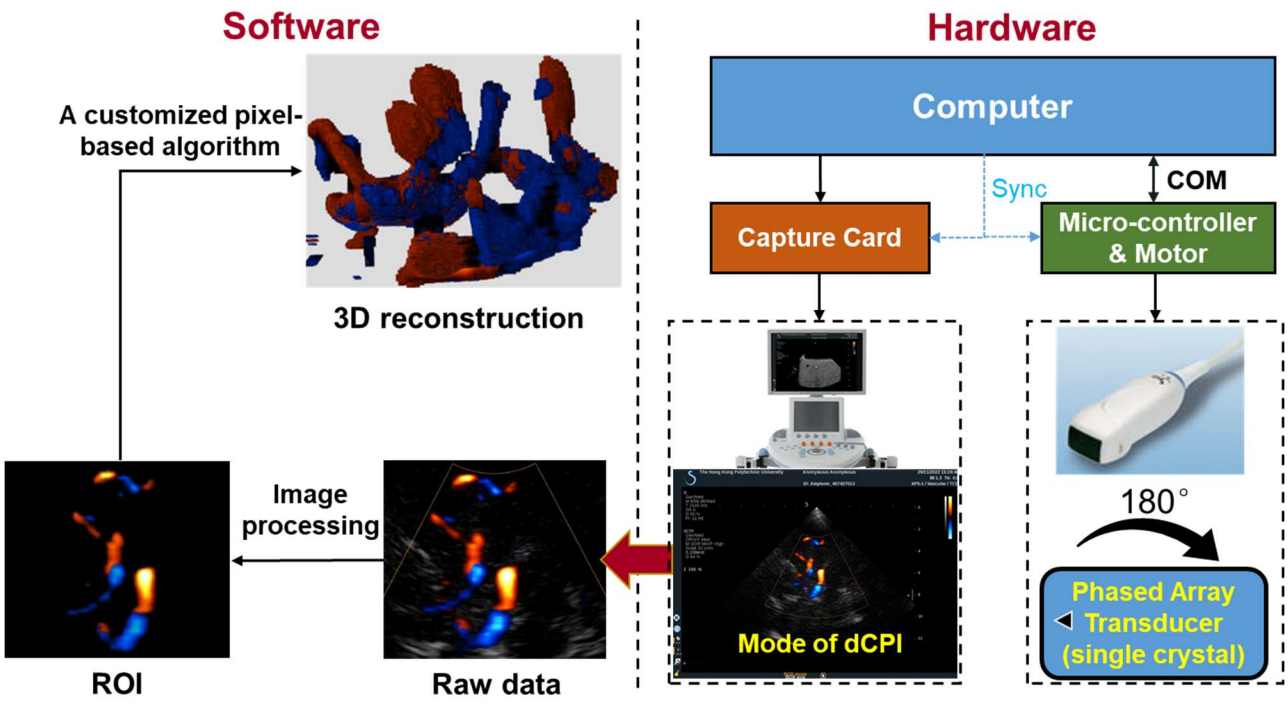

Figure 2-1. The diagram of the UBA system including the software part and the hardware part.

2.2 Hardware design

Figure 2-2 shows the diagram of the hardware part, which includes ultrasound imaging equipment and a rotating probe carrier as the primary components. The ultrasound probe of the equipment was clamped on top of the rotating probe carrier. Scanning was performed using ultrasound imaging equipment (Aixplorer model, SuperSonic Imagine, France) with a commercial single-crystal phased array ultrasound probe (XP5-1, 96 transducer elements and 1-5 MHz of bandwidth). This transducer possesses a broader fractional bandwidth, greater Doppler sensitivity, better lateral resolution, lower sidelobes, and less noise in contrast to the commonly used material of lead zirconate titanate (PZT) (Ye, 2008). The relatively low-frequency range ensures the penetration of ultrasound through the skull.

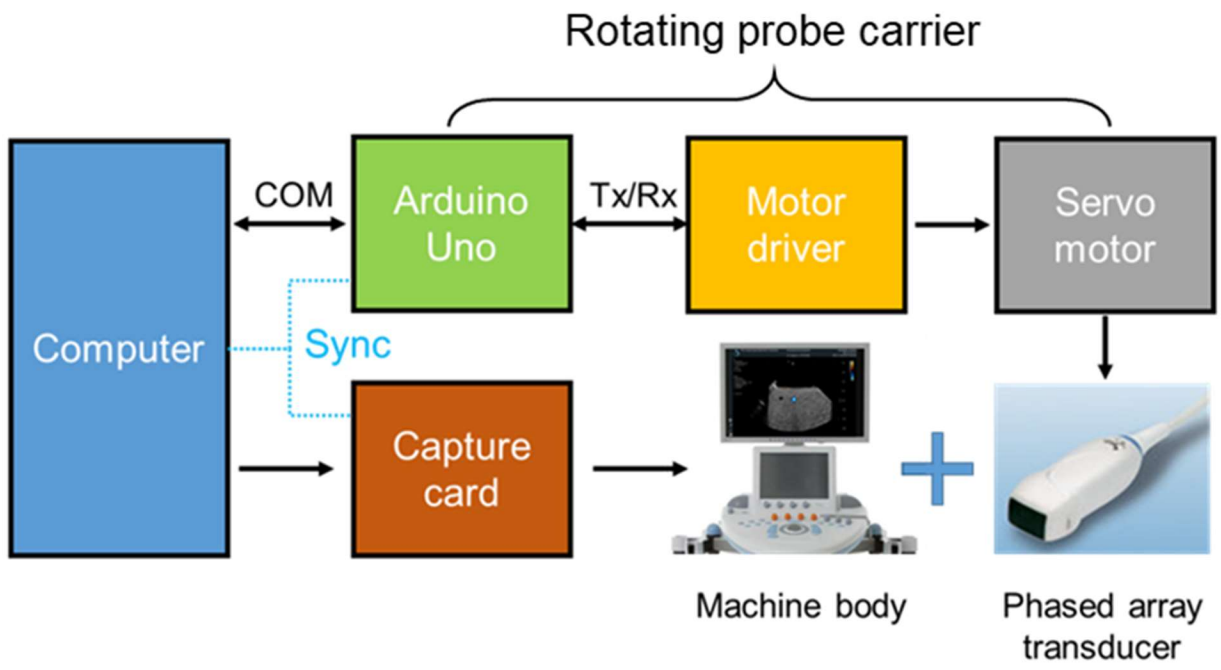

Figure 2-2. The diagram of the hardware part, COM port is the communication port between computer and microcontroller and Tx/Rx is the serial communication between microcontroller and motor driver.

The purpose of the rotating probe carrier is to execute the rotational scanning for 3D data acquisition, and it consists of a single-chip microcontroller (Arduino Uno, Italy), a servo motor (LX-225 model, Hiwonder, China), and a motor driver module. The motor carries the ultrasound probe, rotating it clockwise 180 degrees. The accuracy of the servo motor is 0.24° as a default setting, and the frame rate of ultrasound imaging equipment ranges from 11 to 17 Hz. For adequate slices of 3D reconstruction, the microcontroller was programmed to control the servo motor using a rotating speed of 2 deg/sec. Thus, more than 900 slices were collected for 3D reconstruction within around 90 seconds. The Arduino Uno communicated with the servo motor through the motor driver, as all the commands of control were integrated into the motor driver module. To access the motor driver module, a program library called LobotServiController (downloaded from GitHub) was added to the Arduino Integrated Development Environment (IDE), as all Arduino codes were conducted on the Arduino IDE. Arduino Uno controlled the motor driver module via serial communication with a baud of 115200 for motor rotation. Meanwhile, the position

information, including the rotation time and angle of the servo motor was sent back to the microcontroller. A rechargeable lithium battery was used to power the rotating probe carrier.

Regarding image data collection, a video capture card was used to collect ultrasound color Doppler images by recording the displayed ultrasound images. We used a color mode of directional color power imaging (dCPI), which is an advanced imaging mode integrating the good sensitivity of CPI/PDI with the directional information of CFI (Hoskins et al., 2019). The ultrasound echo was demodulated, filtered, and estimated to obtain the mean Doppler frequency and the amplitude of the Doppler signal. Thus, the directional information of blood flow was obtained from the mean Doppler frequency, and used to color-code the amplitude-related power data (Hoskins et al., 2019).

2.3 Software design

Two applications were developed for data collection and 3D reconstruction, respectively, and both were built using an IDE of Microsoft Visual Studio (VS) using C++ language. The application of data collection was to record ultrasound Doppler images and trigger the rotation of the probe carrier simultaneously. Once the capture card started to capture the ultrasound image, the COM port connecting to Arduino Uno was turned on and sent the command to rotate. All the captured images were formed into a video file in AVI format, and the position information was saved in a txt file.

The set of image processing methods is shown in **Figure 2-3**. In the 3D reconstruction, the 2D image data within the Doppler ROI was converted into a 3D space. ROI, the color area, was extracted by using a set of image processing methods. The raw image was converted from RGB level to gray level first, and then a connected-component labeling algorithm was used to remove

the labels, color bar, and machine logo from the image. The remaining B-mode ultrasound grayscale generally had the same red, green, and blue values in the decimal code of the RGB level, shown in **Figure 2-4**. Hence, removing the background B-mode images (grays) could be efficiently conducted by subtracting the minimum of the decimal coded values. Although it could also remove the white color from a region of high flow velocity, since the high-velocity region only exists at the center of the vessel, the white color could be refilled into the center of the vessel by identifying the outline of the vessel. Meanwhile, some noises, such as the fan-shaped outline, can be eliminated by morphological opening.

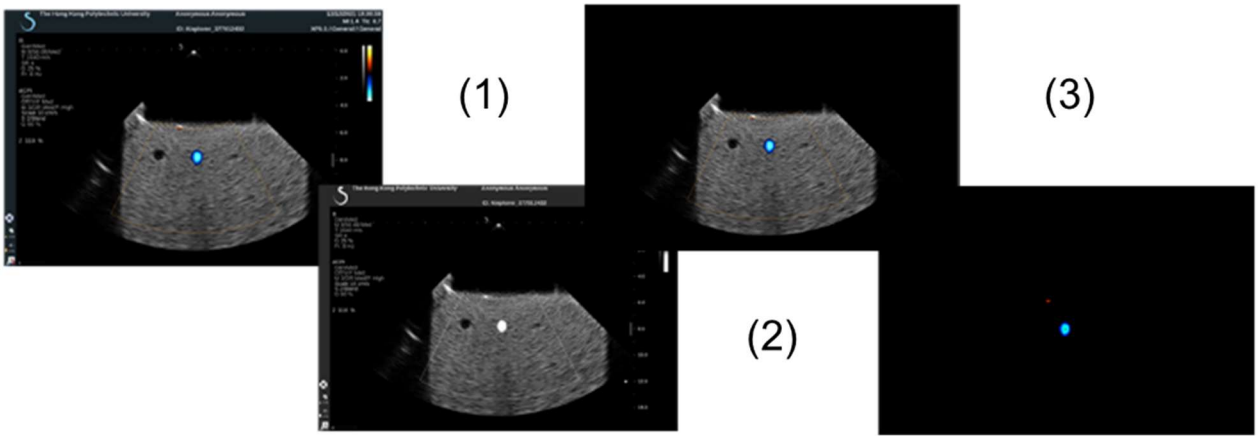

Figure 2-3. The process of image processing methods. Step (1) was to convert the raw image from RGB level to gray level; step (2) used the algorithm of connected-component labeling to keep the useful information in the image; step (3) was to remove B-mode background and the fan-shaped outline.

Figure 2-4. Gray levels with the same red, green, and blue values.

After obtaining the ROI from each ultrasound Doppler image, the pixels in a 2-dimensional image were mapped to voxels in a 3D view using a customized pixel-based algorithm. The revolution axis of the rotating probe carrier was designed to match the middle line of images. The size of each image was 1535*1080 (x, y), equivalent to a resolution of 1.80 mm per pixel. To make the coordinates of all points always positive, the origin was located at the bottom left corner, and the axis of rotation was the middle line of the images (as shown in **Figure 2-5**). Thus, the maximum dimension of the voxels was 1535*1080*1535 (Nx*Ny*Nz). The customized equations of transfer quoted the rotation matrix (Weisstein, 2003) on the y-axis as shown below (1)-(6) and **Figure 2-6** and **Figure 2-7**, where θ represents the rotated angle; X1, Y1, and Z1 indicate the coordinates of the voxel; x and y indicate the coordinates of the pixel; w is the width of the image. Y1 would be kept the same as y since the rotating axis is parallel to the y-axis, and Z1 would be fixed at w/2 at the initial angle.

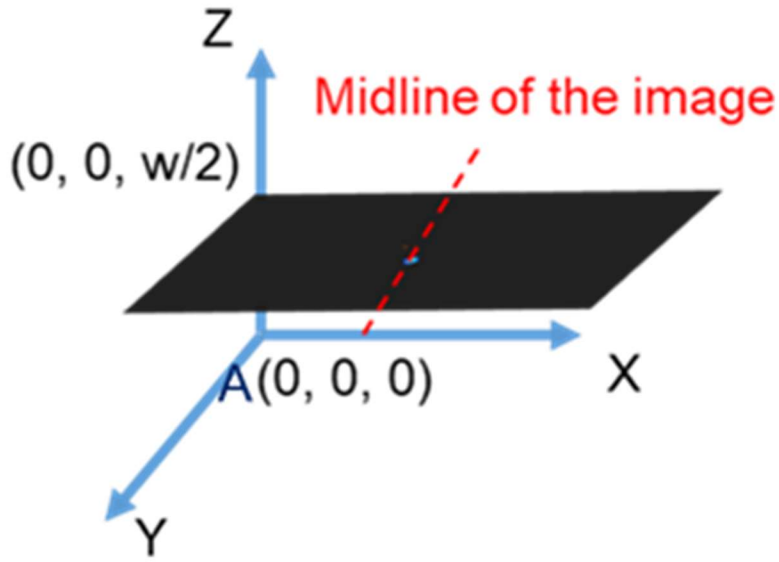

Figure 2-5. The diagram indicates the concept of making the coordinates of all points always positive in the three-dimensional view.

If $\theta \leqslant 90°$:

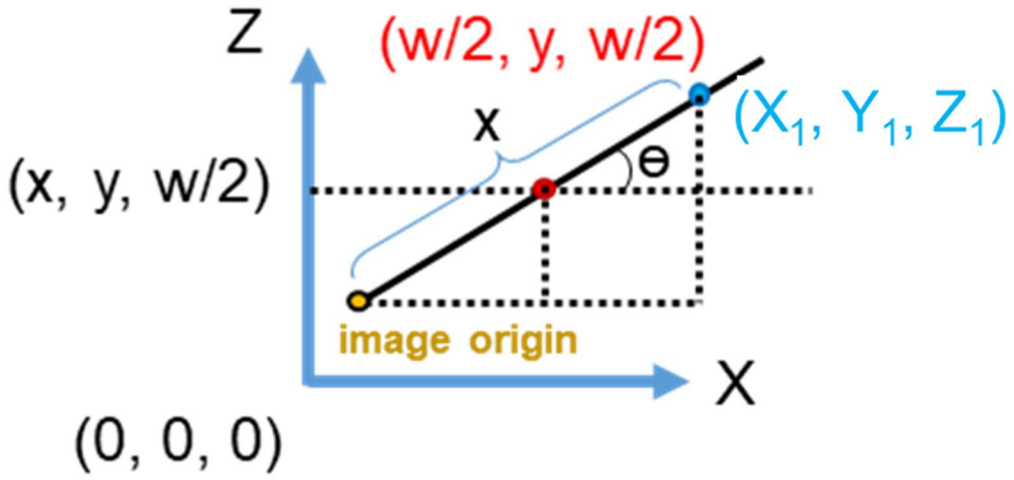

Figure 2-6. This diagram explains the derivation of converting the coordinates from 2D to 3D when the rotated angle is less than 90 degrees.

$$X_1 = x \times \cos(\theta) + w \times (1 - \cos(\theta)) / 2. \quad (1)$$

$$Y_1 = y. \quad (2)$$

$$Z_1 = x \times \sin(\theta) + w \times (1 - \sin(\theta)) / 2. \quad (3)$$

If $\theta > 90°$:

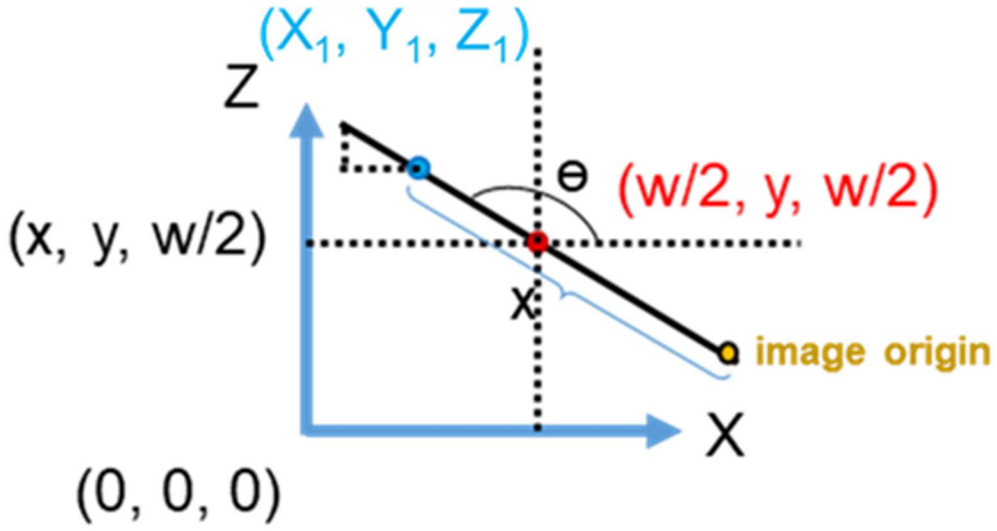

Figure 2-7. This diagram explains the derivation of converting the coordinates from 2D to 3D when the rotated angle is larger than 90 degrees.

$$X_1 = w / 2 – (x - w / 2) \times \cos (\pi - \theta). \quad (4)$$

$$Y_1 = y. \quad (5)$$

$$Z_1 = (x – w /2) \times \sin (\pi - \theta) + w / 2. \quad (6)$$

In these applications, an open-source computer vision library (OpenCV) was used to process the images. The Visualization Toolkit (VTK) was used to construct and display the 3D view by creating a point cloud, comprising more than 0.9 million points. The user interface (UI) was developed by adding a widget toolkit (Qt). **Figure 2-8** shows the reconstructed objective and the user interface.

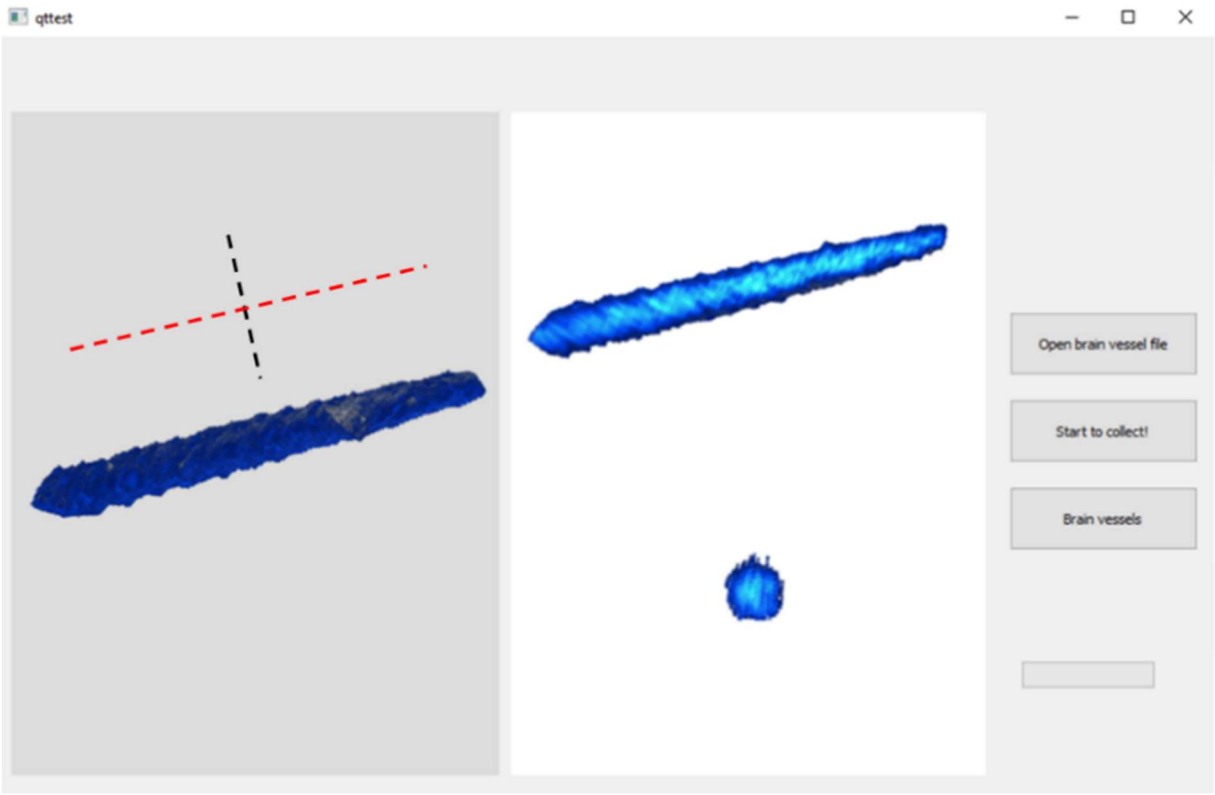

Figure 2-8. The user interface can display the constructed objective in different cross-sectional views; the black and red dashed lines indicate the sectional planes.

2.4 Summary

This section provides an overview of the components and processes involved in the development of the system. In summary, the system comprised two parts: hardware and software. The hardware part required the application of a single-crystal phased array ultrasound probe. The probe utilized in this study comprised a total of 96 array elements, possessing a bandwidth that spanned from 1 to 5 MHz. In order to implement the rotational scanning technique, a servo motor of the LX-225 model was utilized. The rotation was executed with a 180-degree angle at a consistent velocity of 2 degrees per second. The color Doppler images obtained using the color mode of dCPI were gathered simultaneously during the rotation of the probe for later offline image processing and three-dimensional reconstruction. It is noteworthy that the dCPI color mode is an

advanced mode that combines the good sensitivity of CPI/PDI with the directional information offered by CFI. In the software part, a sequence of image processing methods was employed to extract the region of interest from the raw images. Following that, a customized methodology relying on pixel analysis was employed to produce a point cloud depiction of the reconstructed objects accompanied by color labeling.

Chapter 3 Investigation of 3D Vessel Reconstruction Under Doppler Imaging with Phantoms

(This chapter was modified from our accepted paper "S. Li, Q. T. K. Shea, Y. T. Ling, and Y. P. Zheng, Investigation of 3D Vessel Reconstruction under Doppler Imaging with Phantoms: Towards Reconstruction of Circle of Willis, Ultrasonics, 2024. doi: 10.1016/j.ultras.2024.107332.".)

3.1 Introduction

As introduced in **Chapter 1**, early prediction for stroke is necessary due to around 85% of strokes causing death and disability (Donkor, 2018). The cause of stroke is multifactorial and its symptoms are mainly linked to the cerebral arteries (Balami et al., 2013), especially the Circle of Willis (CoW). Even in the event that one of the cerebral arteries becomes occluded or stenotic, the CoW guarantees adequate cerebral blood flow to the brain (Chandra et al., 2017). Blood flow can be directed forward or backward by the pressure created by an obstruction, allowing the blood to reach equivalent brain areas. However, variations and incompleteness of the CoW are widespread, and a number of studies have revealed a notable range of incomplete CoW in various nations, from 50–80% (De Silva et al., 2009; Eftekhar et al., 2006; Kapoor et al., 2008; Li et al., 2011; Maaly & Ismail, 2011; Nordon David & Rodrigues Junior, 2012; Riggs & Rupp, 1963). Meanwhile, a few different kinds of variations have been linked to hemorrhage and ischemic stroke (Banga et al., 2018; De Caro et al., 2021; van Seeters et al., 2015; Vrselja et al., 2014; Zhou et al., 2018).

Therefore, reducing the risk of stroke occurrences is largely dependent on the detection of structural and hemodynamic alterations in the CoW.

Transcranial color-coded Doppler (TCCD) is a clinical tool for stroke screening because of its ability to monitor real-time hemodynamic and structural information in the CoW. Also, TCCD is indispensable in comparison to other widely used imaging modalities like computed tomography angiography (CTA) and magnetic resonance angiography (MRA) because of its non-invasiveness, cheap cost, and being radiation-free (Davenport et al., 2020; Edelman & Koktzoglou, 2019; Lell et al., 2015). TCCD images the inside of the skull through the orbital, temporal, and occipital windows utilizing a phased array transducer (Carrizosa, 2021). Color flow imaging (CFI) is the general color mode used by TCCD, which denotes a frequency shift in the Doppler signal. Color power imaging (CPI), also known as power Doppler imaging (PDI), is another color mode that represents the amplitude change in the Doppler signal (Kollmann, 2015).

Unlike CTA and MRA, however, TCCD is limited by low anatomical precision and a lack of spatial information. To turn TCCD into a 3D level, a 2D array transducer (Ivancevich et al., 2008; Lindsey et al., 2009) or a 1D phased array transducer with mechanical tilting scanning methods (Bauer et al., 1998; Delcker & Turowski, 1997; Huang & Zeng, 2017; Klötzsch et al., 1999; Klötzsch et al., 2002) have been created in the previous few decades. These two approaches use CFI and PDI color modes, respectively; for ease of comprehension, this work refers to them as 3D-CFI via a 2D-array transducer and 3D-PDI. However, color overrepresentation/enlargement poses a challenge to the anatomical accuracy presented in TCCD; this is possibly caused by the complex transmission path of ultrasound inside the skull and greater Doppler signal from relatively high-speed blood flow in small cerebral vessels. The overrepresentation can be influenced by a number of interdependent or independent factors, such as imaging depth, transducer frequency,

velocity scale, color gain, frame rate, and depth of Doppler interrogation, among others (Maulik, 2005). Nevertheless, the application of these controls and the ensuing modifications to the color maps differ between devices. Moreover, because of the non-visualized vessels in B-mode and the need for a single customized parameter setting to display multiple vessels at once, it is challenging to modify all these parameters in TCCD. Therefore, it is acceptable to adjust the velocity scale and color gain settings to guarantee the imaging sufficiency of TCCD in commercial ultrasonography equipment and ease of use. In contrast to CPI/PDI, poor noise containment in CFI results in a larger color overrepresentation (Kollmann, 2015). In the 3D view, there would likewise be an overrepresentation; nevertheless, no quantitative analysis was conducted in these 3D TCCD studies.

This study presents a unique 3D reconstruction method for transcranial three-dimensional color Doppler. To improve the Doppler sensitivity, a phased array transducer composed of a single crystal was employed. Moreover, we used an advanced color mode of directional CPI (dCPI) that integrated better sensitivity of CPI/PDI with the directional information provided by CFI (Hoskins et al., 2019). In order to provide more information regarding the reconstructed CoW, the data collection process used the mechanical technique of rotating scanning, as opposed to tilting scanning. **The aim of this chapter was to examine the effect of several factors, such as vascular diameter, flow velocity, Doppler interrogation depth, and settings of color gain and velocity scale, on the occurrence of color overrepresentation in the 3D reconstruction.**

In this section, a phantom study was conducted. The variables of vascular diameter (2 mm, 4 mm, 6 mm), flow velocity (20.33 cm/s, 29.67 cm/s, 38.91 cm/s, 50.24 cm/s), Doppler interrogation depth (3 cm, 6 cm, 9 cm), setting of speed/velocity scale (matched group and unmatched group), and setting of color gain (matched group and unmatched group), were investigated to determine

their effects on color overrepresentation. Then, the absolute error and ratio of the reconstructed diameter to the actual diameter were calculated for comparison. The findings can be utilized as a point of reference for future research on the reconstruction of the CoW or other relevant subjects.

3.2 Materials and methods

3.2.1 System of Ultrasound Brain Angiography (UBA)

Chapter 2 introduces the details of the system development. In the hardware part, the imaging transducer involved the utilization of a single-crystal phased array ultrasound probe. This probe consisted of 96 elements with a bandwidth ranging from 1 to 5 MHz. To achieve the rotating scanning, a servo motor was employed. The rotation was performed over a 180-degree angle at a constant speed of 2 degrees per second. The ultrasound images collected under the color mode of dCPI were acquired concurrently throughout the rotation of the probe for subsequent offline image processing and three-dimensional reconstruction. In the software part, a series of image processing methods was conducted to extract the region of interest (ROI) from the raw images. Subsequently, a tailored approach based on pixel analysis was utilized to generate a point cloud representation of the CoW with color coding.

3.2.2 Experimental setup

Given the objective of constructing a three-dimensional representation of blood flow, a setup was devised to validate the UBA system, as depicted in **Figure 3-1**. In this test, a peristaltic pump (Masterflex L/S, Germany) was used to generate the controlled flow of fluid at a consistent volume speed. The volume speed could be modified by manipulating the number of revolutions per minute (rpm), allowing for adjustments of the pump. Next, the fluid traversed a flowmeter (Gilmont

Accucal, Germany) prior to entering the vascular phantom (ATS-524, CRIS, USA), with the flowmeter serving as a benchmark for measuring the volumetric flow rate. The vascular phantom was positioned within a tank filled with water in order to facilitate convenient adjustments of angle and distance, while ensuring consistent coupling. Following this, the flow was subsequently redirected back to the peristaltic pump, thereby completing a closed-loop system. During the process of collecting data, the upper part of the phased-array probe was immersed in water and oriented at a 30° angle towards the vascular phantom. Subsequently, the probe carrier executed a 180° clockwise rotation of the phased array probe, thereby recording dCPI images simultaneously.

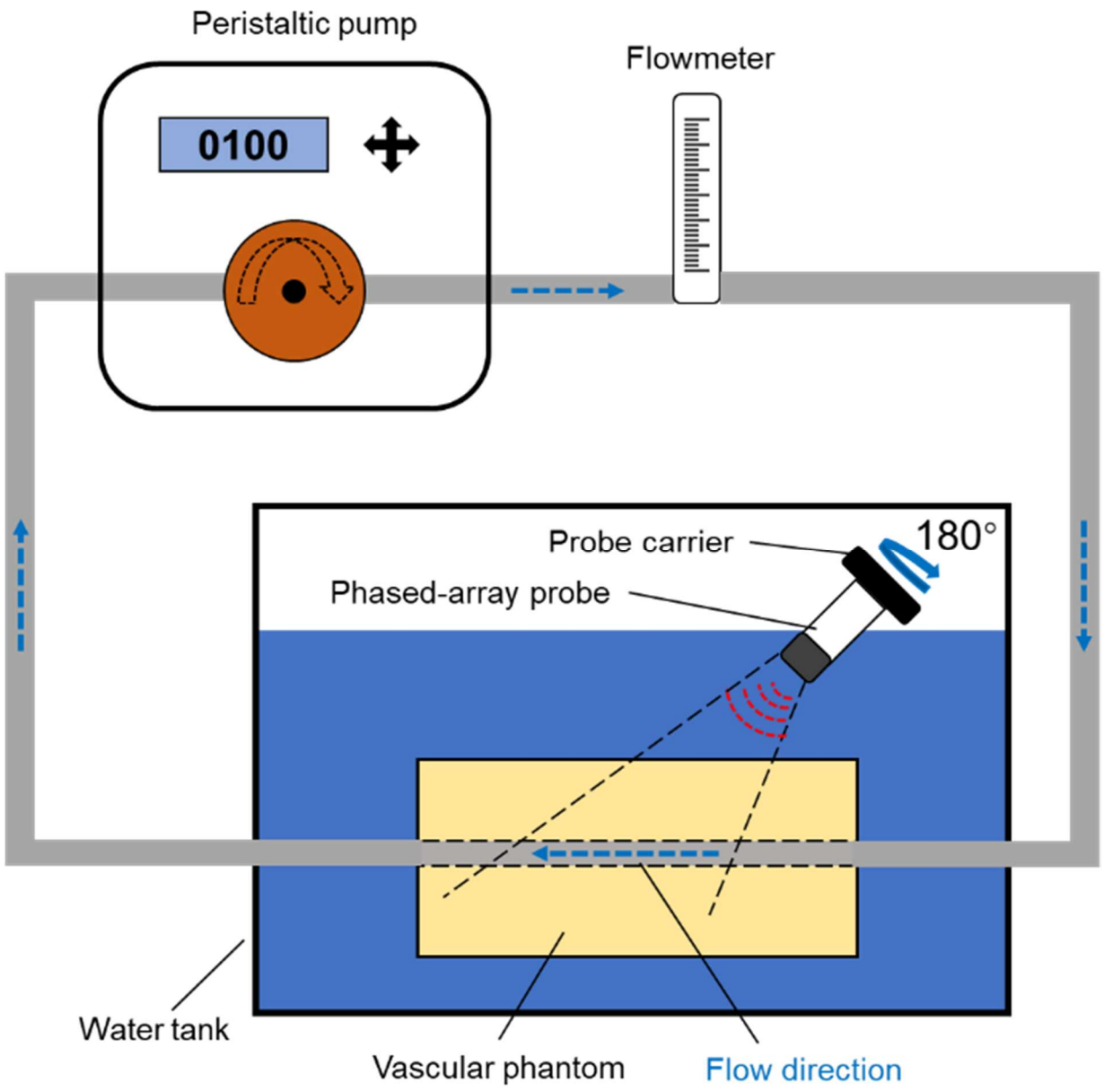

Figure 3-1. The experimental setup for system verification.

3.2.3 Variables for verification and some measurements

This study mainly investigated three variables, namely vascular diameter, flow velocity, and depth between the ultrasound probe and the vessel. The vascular phantom was comprised of four channels, with corresponding diameters of 2, 4, 6, and 8 mm, respectively. To validate the system, channels with diameters of 2 mm, 4 mm, and 6 mm were utilized, considering that the diameter of

the terminal ICA can reach up to 4.6 mm (Rai et al., 2013). The blood flow velocity in the CoW exhibited a considerable variation, ranging from 36 ± 12 cm/s to 62 ± 12 cm/s (Aaslid et al., 1982; Hennerici et al., 1987). Therefore, we assumed that the flow velocities ranging from 20-50 cm/s in tubes of varying diameters were intended to mimic the velocity of blood flow in cerebral arteries. The rotational speed (rpm) of the peristaltic pump was found to have the capability to regulate the velocity of flow. The specific rpm values can be found in **Table 3-1**. Concurrently, the velocity of the flow was evaluated utilizing the pulse-wave Doppler mode, whereby measurements were obtained at the proximal, middle, and distal segments of the vascular conduit, and subsequently averaged. It is essential to acknowledge that, alongside flow velocity, the change of the speed scale could influence the pulse repetition frequency (PRF), hence causing changes in the range of velocities depicted in the image. Two distinct groups were employed in order to ascertain the effect of the speed scale, namely the matching scale and the constant scale. As for the matching scale, the speed scale was adjusted to be in proximity to the pumped flow velocity, but the constant scale had a fixed speed scale and was only set near the minimum pumped flow velocity.

Table 3-1. The rpm setting for different vascular diameter channels.

Diameter (mm)	Flow velocity (cm/s)	rpm setting
6	21.42	57
	31.29	103
	42.18	132
	50.26	188
4	20.33	28
	29.67	52
	38.91	61
	50.24	84
2	52.78	27

Furthermore, in order to replicate the positioning of arteries in the CoW, three Doppler interrogation depths were chosen: 30 mm, 60 mm, and 90 mm. This decision was based on the fact that these arteries are often situated at a depth ranging from around 30 mm to 80 mm from the temporal window, as indicated by previous research (Alexandrov et al., 2007).

3.2.4 Data analysis and statistics

The format of 3D data was converted from ".vtp" to ".xyz" to minimize the file size and convenient for later calculations by the utilization of a customized script developed in MATLAB (MathWorks Inc., Natick, MA, USA). The statistical analyses were performed using GraphPad Prism software (GraphPad Software Inc., LaJolla, CA, USA). In order to determine the dimensions of the reconstructed targets, a minimum of 100 slices were utilized to imitate circles (see **Figure 3-2**). Subsequently, the mean diameter of the imitated circles was calculated, and this average value was designated as the reconstructed diameter. In order to assess the dimensional variations in the reconstructed objects, we performed calculations to determine the absolute error and the ratio between the reconstructed diameter and the actual diameter. These metrics were then utilized for comparative analysis. The statistical significance of any observed differences was evaluated using a t-test.

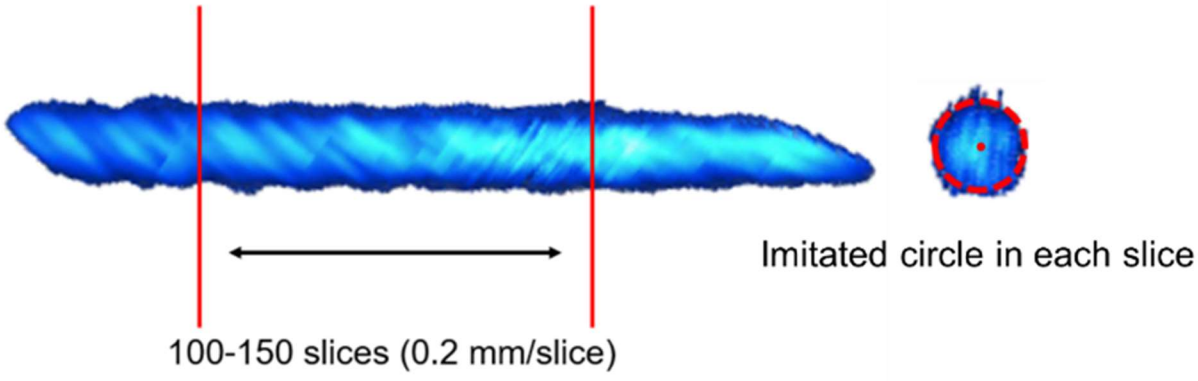

Figure 3-2. 100 to 150 slices in the middle part of the reconstructed objective were used to calculate the average diameters of the imitated circles.

3.3 Results

3.3.1 Reconstruction under different vascular diameters

A mean flow velocity of roughly 50 cm/s was pumped and subsequently delivered to three different channels with diameters of 2 mm, 4 mm, and 6 mm. The sectional planes depicting the reconstructed results are presented in **Figure 3-3**, while additional information can be found in **Table 3-2**. The reconstructed liquid flows exhibited larger diameters when compared to the actual diameter values. Specifically, diameters of 2 mm, 4 mm, and 6 mm were found to be increased to 4.43 mm, 5.64 mm, and 7.20 mm, respectively.

Table 3-2. The phantom channels under the velocity of around 50 cm/s (under 51 cm/s measuring scale).

Vascular channel (mm)	Flow speed (cm/s)	Reconstructed diameter (mm)	Absolute error (mm)	Ratio
2.00	52.78	4.43	2.43	2.21
4.00	50.24	5.64	1.64	1.41
6.00	50.26	7.20	1.20	1.20

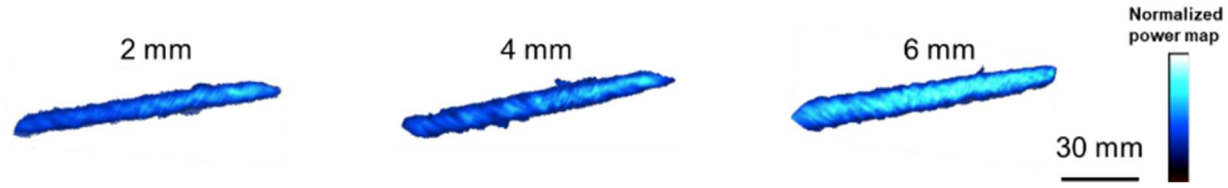

Figure 3-3. The sectional planes of the reconstructed vascular channels with different diameters.

3.3.2 Reconstruction under different flow velocities

In order to closely replicate flow velocities of 21 cm/s, 31 cm/s, 41 cm/s, and 51 cm/s, we established four specific flow speeds: 20.33 cm/s, 29.67 cm/s, 38.91 cm/s, and 50.24 cm/s. The four velocities traversed the vascular channel with a diameter of 4 mm, and the outcomes of the reconstruction process are depicted in **Figure 3-4**. More relevant information can be found in **Table 3-3**. It is worth noting that no significant difference was observed in the reconstructed diameters when comparing absolute error and ratio values across varying flow velocities.

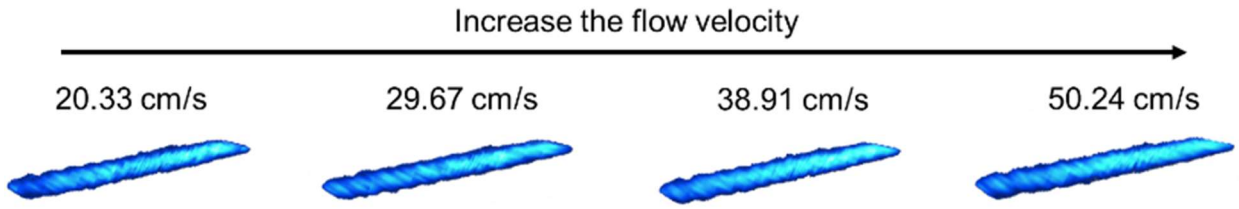

Figure 3-4. The sectional planes of the reconstructed vascular channel (4mm) with different flow velocities.

Table 3-3. The 4 mm channel under different flow velocities under a 21 cm/s measuring scale.

Flow speed (cm/s)	Reconstructed diameter (mm)	Absolute error (mm)	Ratio
20.33	6.01	2.01	1.50
29.67	6.24	2.24	1.56
38.91	6.46	2.46	1.62
50.24	6.32	2.32	1.58

This set of velocities utilized two velocity scale settings, namely the constant velocity scale and the matching velocity scale. Changes made to the velocity scale setting in commercial ultrasound systems have the potential to induce modifications to the pulse repetition frequency, thereby impacting the sensitivity of Doppler measurements. The constant velocity scale was adjusted to the lowest velocity scale of the ultrasonic equipment, which was 21 cm/s (the measuring scale indicated in **Table 3-3**). On the other hand, the matching velocity scale was employed to set up the measuring scale at 21 cm/s, 31 cm/s, 41 cm/s, and 51 cm/s to match the flow velocities. Under the setting of constant velocity scale, it was observed that there was an increased presence of bright region, as illustrated in the sectional planes depicted in **Figure 3-5 (a)**. The comparison was also performed by calculating the ratios between the reconstructed diameter and the real diameter, as depicted in **Figure 3-5 (b)**. The findings of this study suggest that the reconstructed diameter was observed to be bigger when using the constant velocity scale, whereas the use of the matched velocity scale helped to reduce the overrepresentation of diameter.

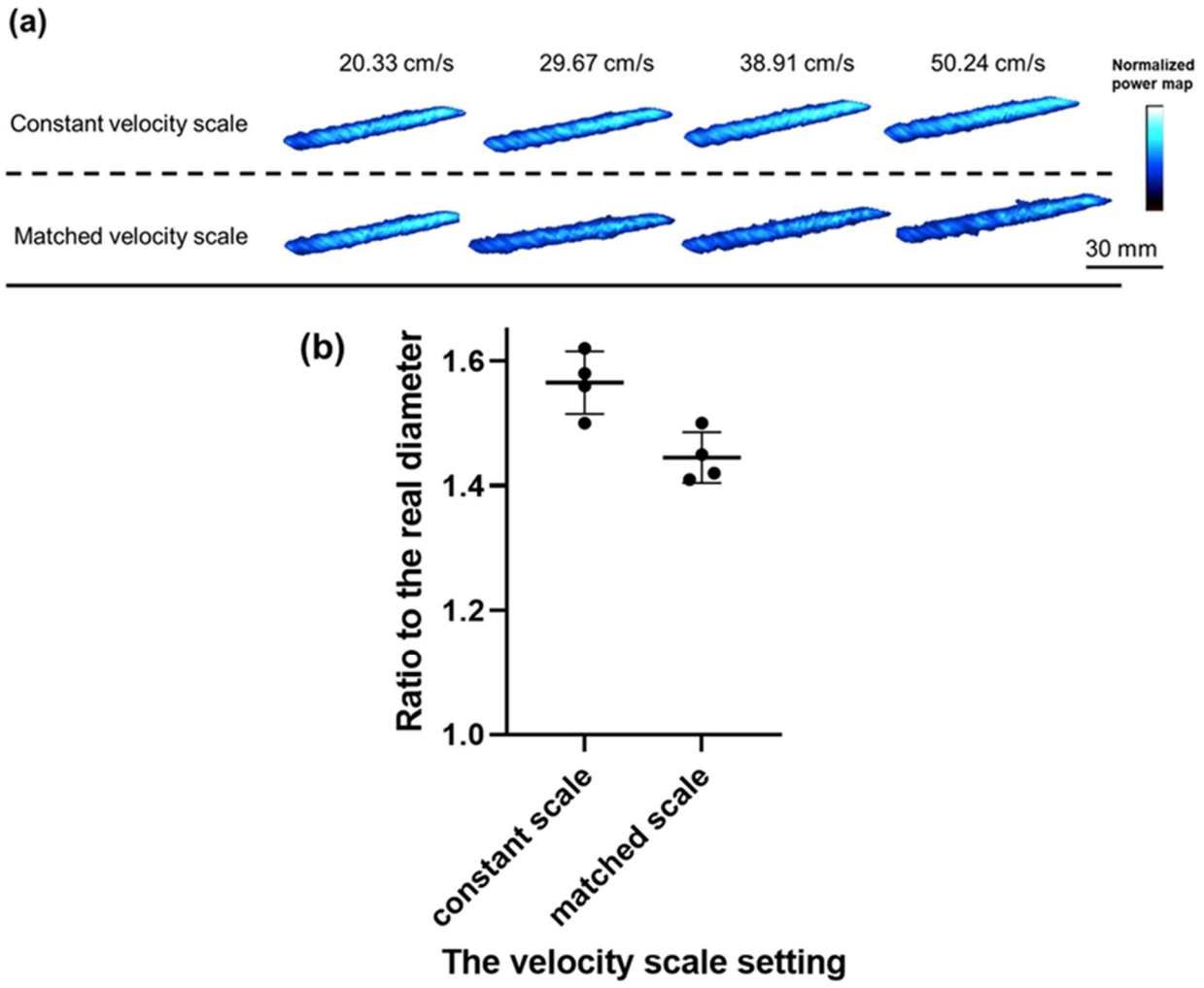

Figure 3-5. (a) Illustration of the sectional planes of the reconstructed objects (4 mm channel). The planes were scanned under two velocity scale settings, constant velocity scale (fixed at 21 cm/s) and matched velocity scale (21 cm/s, 31 cm/s, 41 cm/s, and 51 cm/s). The flow velocities for the scanning were 20.33 cm/s, 29.67 cm/s, 38.91 cm/s, and 50.24 cm/s, respectively. (b) Comparison between these two velocity scale settings in terms of the ratio of reconstructed diameter to the real diameter.

3.3.3 Reconstruction under different depths close to the ultrasound probe

To cover the distance range from the temporal window to the CoW, three depths were established at 3 cm, 6 cm, and 9 cm. The flow velocity was consistently maintained at an approximate value of 50 cm/s. The parameter settings remained constant throughout the experiment, and the gain was varied to optimize the visualization of the Doppler signal at a depth of 9 cm. A heightened color representation was observed during the scanning process when the vascular phantom was positioned in closer proximity to the ultrasonic transducer. Furthermore, it

was noticed that a more extensive region characterized by high flow velocity was present within the central color region, as depicted in **Figure 3-6 (a)**. A comparable occurrence was observed in the reconstructed objects, as depicted in **Figure 3-6 (b)**. The size of the reconstructed fluid expanded, and the velocity of the flow inside the fluid elevated as the proximity of the depth to the transducer grew. The start frame was alternatively denoted as the start location in the experiment. The quantified diameter of the reconstructed flow is depicted in **Figure 3-6 (c)**, revealing that a greater ratio value was seen when the depth was in closer proximity to the probe.

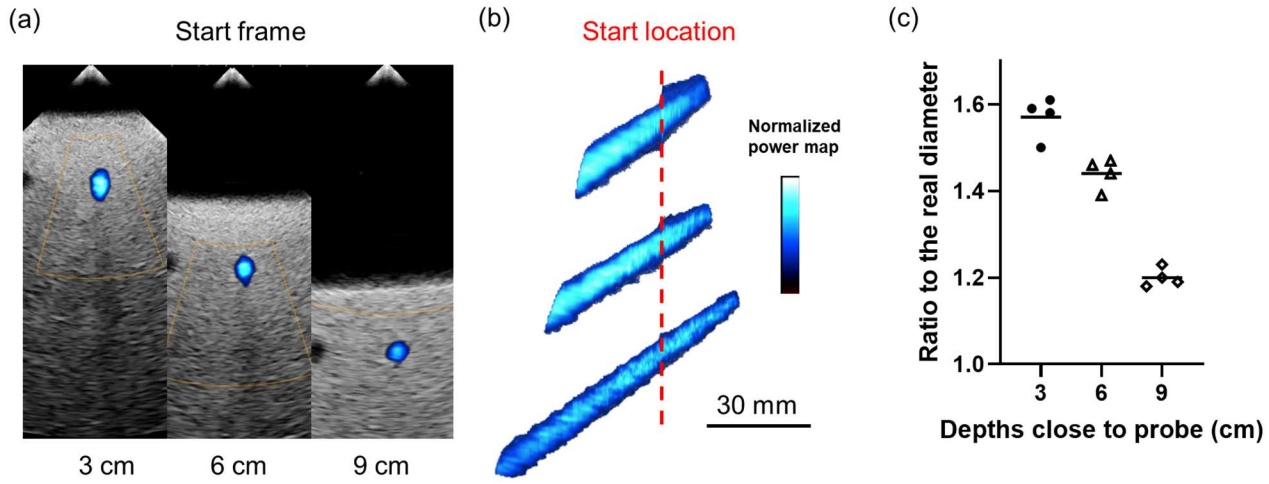

Figure 3-6. (a) Display of the starting frames of scanning at different depths. (b) Indication of the sectional views of the reconstructed objects measured at different depths, and here the start frame is referred to as the start location. (c) Comparison of the ratio values under different depths.

The increase in the size of color areas may contribute to the overrepresentation of the reconstructed objects. In light of the potential influence of the velocity scale setting on the size of the color area, we also investigated the effect of color gain on this adjustment. The color gain was standardized at a depth of 9 cm, with particular changes made for depths of 3 cm and 6 cm. The comparison of the ratio change is illustrated in **Figure 3-7 (a)** and **(b)**. It is worth noting that a statistically significant difference was consistently observed between the pre- and post-adjustment stages. These stages were referred to as the matched and unmatched settings of color gain, respectively.

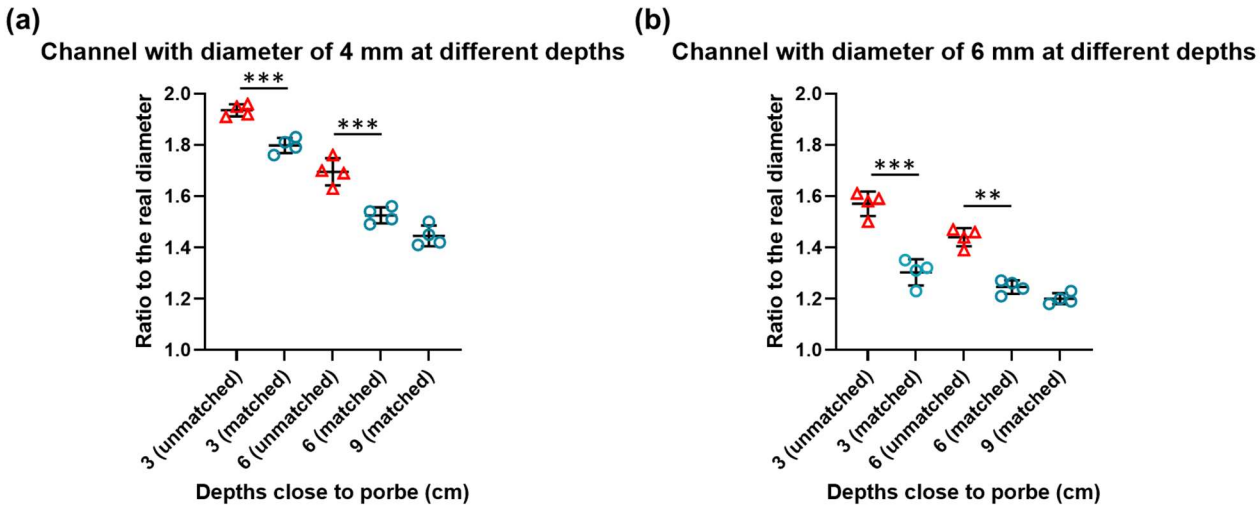

Figure 3-7. The ratio values in different depths with the matched or unmatched setting of color gain. (a) the channel with a diameter of 4 mm. (b) the channel with a diameter of 6 mm. The red color means "unmatched" and blue color is "matched".

3.4 Discussion

The objective of this work was to build an innovative three-dimensional ultrasonic imaging system and evaluate its accuracy in reconstructing brain vasculature. In order to simulate cerebrovascular conditions, three variables were examined in order to verify the accuracy of the reconstructed resolution. This was achieved by calculating the absolute error and the ratio between the reconstructed diameter and the actual diameter. The findings indicated a persistent phenomenon of color overrepresentation in the reconstructed objects. Conversely, the smaller diameter channel, specifically the 2 mm channel, exhibited larger values of absolute error and ratio. This phenomenon perhaps was attributed to the elevated internal pressure within the narrower vascular channel, resulting in the outward displacement of the elastic channel walls. The assumption made here can be supported by Barlow's formula ($P = 2St/D$). Given that all channels in the phantom possess identical material properties (S) and wall thickness (t), it can be inferred that a reduction in channel diameter (D) would lead to an increase in internal pressure (P).

Furthermore, it was noted that there was a relatively similar overrepresentation of reconstructed objects across various flow velocities. It is important to highlight that the set of flow velocities did not surpass the Nyquist threshold, as there was no occurrence of aliasing or Nyquist effect during the collection of data. There is a likelihood that the reconstructed flow size will exhibit relative constancy while solely altering the flow velocity within the Nyquist threshold. The ratio values exhibited a decreasing trend with increasing depth. The observed phenomenon might be attributed to the modification of the size of the interrogated (color) window and the alteration of the interrogated depth. Reducing the size of the window has the potential to improve the temporal resolution and raise the Doppler sensitivity. Meanwhile, the amplitude of the Doppler signal is reduced by a substantial increase in the depth of interrogation (Maulik, 2005). As illustrated in **Figure 3-6 (b)**, the system exhibited an automatic adaptation to a reduced color window when reaching a depth of 3 cm, so making the acquisition of a greater amount of Doppler information possible. As a result, the detection of amplitude flow information at a depth of 3 cm was found to be more abundant compared to depths of 6 cm and 9 cm. In the course of our investigation, it was seen that the selection of velocity scale had an effect on the dimensions of the reconstructed flow. Specifically, the ratio values within the matched scale group were found to be lower in comparison to those of the constant scale group. The alteration of the velocity scale can affect the PRF, whereby a higher velocity scale corresponds to a greater PRF but a reduced Doppler sensitivity (Maulik, 2005). Therefore, a greater amount of Doppler information was gathered in the constant scale group, potentially resulting in an increased reconstructed size. As for the color gain, the alteration in color gain resulted in a modification of the size of the reconstructed flow since it influenced the amplification of the Doppler signal (Maulik, 2005). Consequently, the unmatched

groups exhibited larger ratio values as a result of the inappropriate adjustment of color gain, which led to the inclusion of a greater number of noise components in the Doppler signal.

During the course of this work, it became apparent that 3D TCCD has a limitation in its ability to produce more accurate reconstructions. Nevertheless, it is conceivable that this limitation can be overcome through the refinement of interdependent or independent factors, or by implementing calibration methods that leverage ratio values. The ratio values, while subject to variation between different devices, can be derived through meticulous computations.

Limitations: The present study does not appear to take into account the curvature of vessels and realistically pulsating flow, which seems to be factored into replicating the complexity of the CoW. Actually, the effect of vessel curvature on the outcome of 3D reconstruction may not be influential, given that commercialized clinical ultrasonography systems are capable of detecting flow within curved vessels (Deane, 2017). In relation to the authentically pulsatile flow, it is expected that the human participant will be in a condition of rest during data collection, hence minimizing fluctuations in peak systolic velocity. The vessel phantom can thus be utilized to replicate the flow with a consistent velocity. Noteworthily, ultrasonic imaging operates as a linear system, wherein the output at a given time is solely dependent on the input at that specific time, and not influenced by the input/output of any preceding time. This enables us to streamline the problem by only considering a constant flow, and subsequently extend the findings under pulsated flow conditions. Furthermore, there is a lack of investigation into the potential effects of adjusting the wall filter setting. The wall filter, also referred to as a high-pass filter (Maulik, 2005), has the potential to affect the amplitude or intensity of the flow. The omission of the wall filter setting in this study was due to the absence of any vascular wall movement observed in the vessel phantom.

Therefore, the wall filter was adjusted to a moderate level in order to ensure a relatively low-flow condition throughout all experimental procedures.

3.5 Summary

Color overrepresentation poses a challenge to the anatomical accuracy presented in 2D TCCD, which would likewise be the same in 3D TCCD. The overrepresentation can be influenced by several interdependent or independent factors, such as imaging depth, transducer frequency, velocity scale, color gain, frame rate, and depth of Doppler interrogation, among others (Maulik, 2005). Nevertheless, the application of these controls and the ensuing modifications to the color maps differ between devices.

This study developed a novel 3D TCCD imaging system, called UBA, using a single-crystal phased array transducer to improve the Doppler sensitivity and an advanced color mode of directional CPI (dCPI) that integrated better sensitivity of CPI/PDI with the directional information provided by CFI (Hoskins et al., 2019).

This section aims to determine the effects of these factors on the phenomenon of color overrepresentation within our UBA system. Hence, an investigation was conducted to assess the effects of several factors, including vascular diameter, flow velocity, depth between the ultrasound probe and the vessel, speed/velocity scale, and color gain. The investigations were carried out utilizing the vascular phantom. In order to assess the precision of the reconstructed resolution, calculations were performed to determine the absolute error and the ratio between the reconstructed diameter and the actual diameter.

In summary, a persistent pattern of color overrepresentation was found in the reconstructed objects. The smaller diameter channel exhibited larger values of absolute error and ratio. A relatively similar color overrepresentation of reconstructed objects was detected across various flow velocities. The color overrepresentation exhibited a decreasing trend with increasing depth. Meanwhile, the setting of velocity scale and color affected the dimensions of the reconstructed flow.

Although this work still reported a relatively low precision of dimension measurements using 3D TCCD, this limitation can be potentially addressed by fine-tuning factors or implementing calibration methods that utilize ratio values. Therefore, this work provides valuable insights that can be utilized as a point of reference for future research on the reconstruction of the CoW or other relevant subjects.

Chapter 4 UBA System Enhances the Vascular Detection Rate with Hemodynamic Captures

(This chapter was modified from our under-review paper "S. Li, C. P. Y Wan, Q. T. K. Shea, Y. T. Ling, X. Y. Chen and Y. P. Zheng, A Novel 3D Transcranial Color Doppler System Enhances Vascular Detection Rate with Hemodynamic Captures, Computers in Biology and Medicine, CIBM-D-23-13146".)

4.1 Introduction

As introduced in the **Chapter 1**, the 3D TCCD has been developed as a solution that possesses the capability to generate a three-dimensional representation of the CoW and provide dimensional information. Utilizing a 1D transducer equipped with mechanical scanning techniques, including linear scanning, rotational scanning, and tilting scanning, or a 2D matrix array ultrasound transducer are the approaches to acquiring data for 3D TCCD (Huang & Zeng, 2017).

In the 1990s, 3D TCCD for human investigations was first reported. Image collection was conducted using a phased array transducer operating in color power imaging (CPI) mode. Data acquisition was accomplished through the mechanical scanning technique of tilting scanning (Bauer et al., 1998; Delcker & Turowski, 1997; Huang & Zeng, 2017; Klötzsch et al., 1999, 2002). This method is additionally referred to as 3D-PDI. Contrast agents, specifically microbubbles, were frequently employed in these 3D TCCD investigations to alleviate the challenge posed by the substantial attenuation that occurs during ultrasound penetration through the skull (Pinton et

al., 2012). The contrast agent increases the detection rates of cerebral arteries, such as MCAs, ACAs, and PCAs from 80% to 100% on the ipsilateral side and from 40% to 90% on the contralateral side, as determined by comparing the rates with and without contrast injection (Delcker & Turowski, 1997). Nevertheless, 3D-PDI is incapable of furnishing any data regarding the direction of blood flow, a critical factor in the diagnosis of cerebrovascular disorders. On the other hand, it has also been reported that a 2D matrix-array transducer can generate a three-dimensional view of the CoW when combined with an imaging mode of color flow imaging (CFI), in addition to 3D-PDI (Ivancevich et al., 2008; Lindsey et al., 2009). This method is additionally referred to as 3D-CFI via a 2D-array transducer. While employing CFI mode could provide additional hemodynamic information, the enhancement led by the contrast agent only resulted in an approximate 60% average detection rate (Ivancevich et al., 2008). The reduced detection rate observed in 3D-CFI via a 2D-array transducer could potentially be attributed to a moderated Doppler sensitivity. Therefore, these existing 3D TCCD techniques suffer either from a lack of hemodynamic information or inadequate vascular detection rate, both of which are crucial in the current medical era.

Our newly developed 3D TCCD system, ultrasound brain angiography (UBA), aims to overcome the abovementioned limitations by applying a phased array made of a single crystal and an imaging mode of directional CPI (dCPI). dCPI is an advanced imaging mode that combines the flow direction information provided by CFI with the high sensitivity of the Doppler amplitude signal supplied by CPI/DPI (Hoskins et al., 2019). Theoretically, UBA is capable of achieving improved sensitivity in detecting blood flow while simultaneously providing directional information. **The aim of this chapter was to determine the enhanced performance in the UBA**

system by evaluating its captured vascular detection rates and hemodynamic information, like the direction and velocity of the blood flow.

In this section, the UBA system was applied to 32 healthy older adults. The detection rates of cerebral vessels within the CoW were calculated and compared with previous studies, 3D-PDI and 3D-CFI via a 2D-array transducer. Meanwhile, hemodynamic information, such as the blood flow direction and velocity, was also evaluated using our UBA system. According to the results, UBA has a high potential for application in diagnosing clinical conditions associated with CoW abnormality.

4.2 Materials and methods

4.2.1 Subjects

Ethical approval was granted by the authority of the Human Subject Ethics Sub-committee (HSESC) of the Hong Kong Polytechnic University (HSEARS20201119002). A total of 32 elderly individuals, consisting of 21 men and 11 women, with a mean age of 65.8 ± 7.9 years, were recruited to undergo UBA scanning at the university campus. The exclusion criteria were individuals with an open wound surrounding the temporal bone, a history of head injury (past or current), stroke, Meniere's disease, pregnancy, epilepsy, ongoing cancer or thrombolytic treatment, and any previously documented contraindications to the use of transcranial ultrasonography. Following a comprehensive briefing on the research and experimental protocols, all the participants provided their informed consent by signing a formal document, which was presented to them in both written and spoken formats prior to the commencement of the tests.

4.2.2 UBA imaging system

The details of the UBA imaging system have been clearly described in **Chapter 2**. Briefly, a single-crystal phased array ultrasonic probe (XP5-1, SuperSonic Imagine, France) consisting of 96 elements and operating within a bandwidth of 1-5 MHz was subjected to a rotational motion of 180 degrees. The rotation was achieved by employing a servo motor (LX-225 model, Hiwonder, China) at a constant speed of 2 degrees per second. The images under directional color power imaging (dCPI) mode were acquired concurrently throughout the rotation of the probe for subsequent offline image processing and three-dimensional reconstruction. Significantly, the dCPI color mode is an innovative approach that merges better sensitivity of CPI/PDI with the directional information provided by CFI (Hoskins et al., 2019). A series of image processing techniques were employed to extract the ROI from the color Doppler images. Subsequently, a tailored algorithm based on pixel analysis was implemented to provide a point cloud representation of the CoW with color coding.

4.2.3 Data acquisition

A handheld scanning technique was achieved by utilizing a 3D-printed Nylon enclosure to assemble the ultrasonic probe and servo motor. The participants were instructed to assume a lateral recumbent position on the bed for the scanning procedure. Subsequently, the probe was positioned at the transtemporal acoustic window in order to identify an ideal scanning site, as depicted in **Figure 4-1**. The middle part of the temporal window was given preference for imaging purposes owing to its comparatively greater incidence of successful scanning among senior individuals (Chan et al., 2023). Then the best site was determined as the scanning plane where the anterior cerebral arteries (ACAs), posterior cerebral arteries (PCAs), and middle cerebral arteries (MCAs) were visible in the interrogation window. Upon assessing the sufficiency of the imaging, it is

necessary to steady the holder in order to provide a consistent and unchanging position. Ultimately, a comprehensive 3D ultrasound dataset was acquired by initiating the server motor and thereafter storing it in the computer. Furthermore, some participants were invited to undergo MRA scanning in order to serve as a point of reference in order to gain a more comprehensive understanding of the anatomical composition of the CoW in the context of UBA.

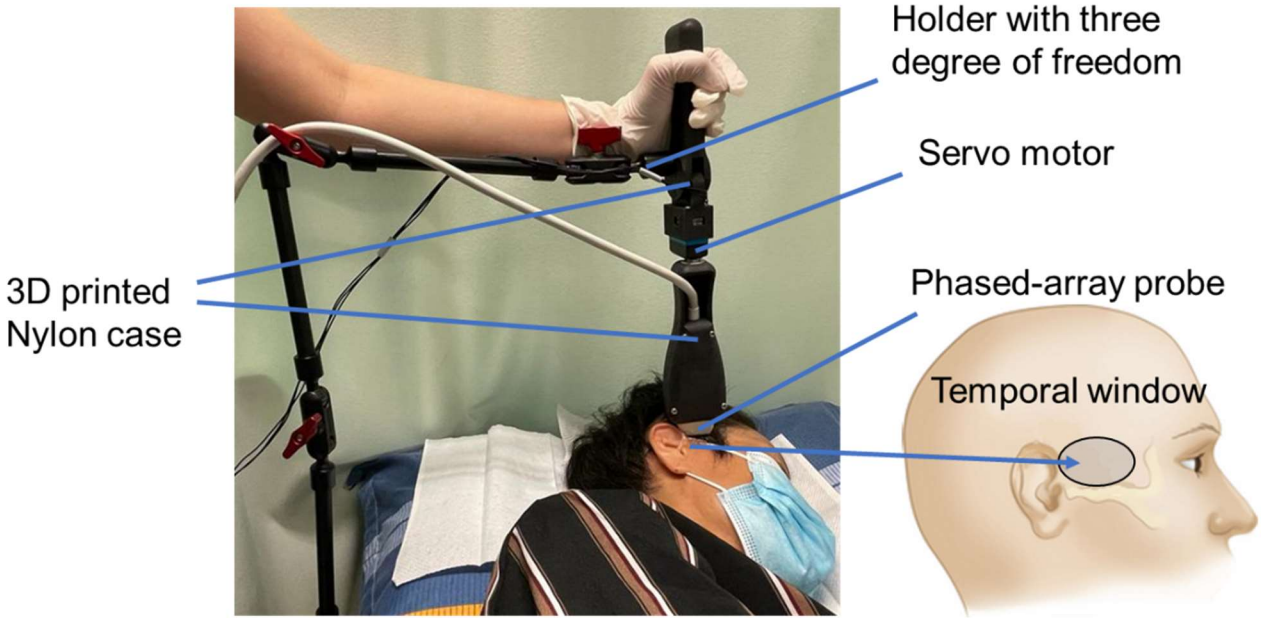

Figure 4-1. Handheld design and the setup for UBA data acquisition. The 3D printed Nylon case was used to assemble the servo motor and the phased array probe. During the data collection, the phased array probe was attached to the region of the temporal window (gray area). Ultrasound gel was applied to maintain acoustic coupling between the transducer and skin surface. The scanning probe was stabilized using the holder arm to minimize the movement during scanning for imaging.

4.2.4 Data analysis and statistics

The UBA data underwent processing in Visual Studio 2019, a software development platform developed by Microsoft Corporation, headquartered in Redmond, Washington, USA. The processing was carried out using the C++ programming language. Image processing was conducted using the open-source computer vision toolkit, OpenCV 4.5.3. The CoW was visualized in three dimensions using the Visualization Toolkit (VTK 9.1.0) through the generation of a point cloud. The user interface was constructed through the incorporation of a widget toolkit, specifically

Qt version 6.2.1. The analysis focused on the detection rates and flow direction of the cerebral arteries within the CoW, specifically examining the ipsilateral and contralateral sides in relation to the transducer. The detection rates of vessels were calculated by counting the cerebral vessels detected in the reconstructed CoW, and this operation was conducted by an ultrasound doctor. The statistical analyses were conducted using GraphPad Prism 9 software (GraphPad Software Inc., LaJolla, CA, USA).

4.3 Results

4.3.1 The anatomical structure of the CoW delivered by UBA

Figure 4-2 displays the representative visible structure of the cerebral arteries as generated by UBA and MRA. The cerebral arteries were identified in MRA images, as shown in **Figure 4-2 (a)**. **Figure 4-2 (b)** reveals a more distinct depiction of the CoW architecture on the ipsilateral side in comparison to the contralateral side. In the meantime, the detection rates pertaining to cerebral arteries were computed and are subsequently documented in **Table 4-1**. The rates of detecting ipsilateral vessels were found to be 87.5% for the ICA, 100% for the MCA, 96.9% for the ACA-A1, 56.3% for the ACA-A2, 90.6% for the PCA-P1, and 65.6% for the PCA-P2. The rates of detecting contralateral vessels were found to be 65.6% for the ICA, 31.3% for the MCA, 87.5% for the ACA-A1, 46.9% for the ACA-A2, 56.3% for the PCA-P1, and 3.1% for the PCA-P2. Based on the observed detection rates, it is evident that the ipsilateral vessels consistently exhibited higher values compared to their contralateral counterparts. The UBA system exhibited comparable detection rates on both the ipsilateral and contralateral sides when compared to non-enhanced 3D-PDI (Delcker & Turowski, 1997) and contrast-enhanced 3D-CFI (Ivancevich et al., 2008) (as shown in **Table 4-1**). On the ipsilateral side of the CoW, UBA showed higher detection rates for

the MCA at 100%, the ACA-A1 at 96.9%, and the PCA-P1 at 90.6%. In comparison, the 3D-PDI had detection rates of 90% for ipsilateral MCA, 90% for ipsilateral ACA-A1, and 60% for ipsilateral PCA-P1. The contrast-enhanced 3D-CFI via a 2D-array transducer had detection rates of 100% for ipsilateral MCA, 88% for ipsilateral ACA-A1, and 82% for ipsilateral PCA-P1. In terms of the contralateral side, the utilization of contrast-enhanced 3D-CFI via a 2D-array transducer yielded higher detection rates in comparison to non-enhanced UBA and 3D-PDI techniques, particularly in the case of the MCA. The detection rates for contralateral MCA were found to be 88% when using contrast-enhanced 3D-CFI via a 2D-array transducer. In comparison, non-enhanced UBA and 3D-PDI only detected approximately 30% for contralateral MCA. Significantly, UBA demonstrated commendable outcomes in both ipsilateral and contralateral internal ICA.

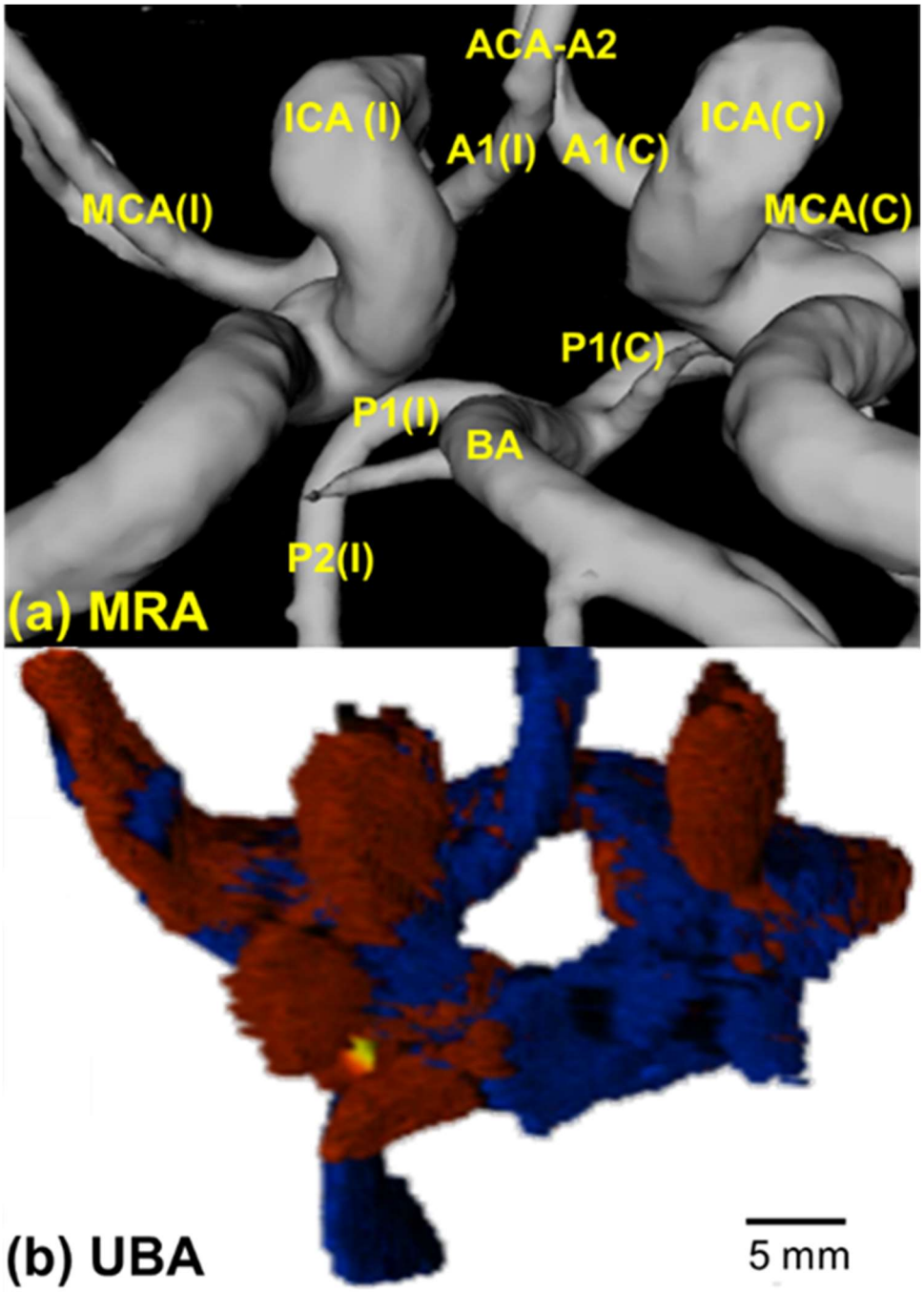

Figure 4-2. The anatomical structure of the CoW in a representative subject was imaged by both (a) MRA and (b) UBA. In contrast to MRA, most of the cerebral arteries were delivered by using UBA. I: ipsilateral side; C: contralateral side; A1: the A1 segment of ACA; P1: the P1 segment of PCA; P2: the P2 segment of PCA; BA: basilar artery.

Table 4-1. Detection rates of important cerebral arteries in the CoW using different imaging techniques.

Vessel (Ipsilateral)	Detection Rate (%)			Vessel (Contralateral)	Detection Rate (%)		
	UBA (n=32)	3D-PDI [1] (n=10)	2D array*[2] (n=17)		UBA (n=32)	3D-PDI[1] (n=10)	2D array*[2] (n=17)
ICA	87.5	Null^	29.0	ICA	65.6	Null^	0
MCA	100.0	90.0	100.0	MCA	31.3	30.0	88.0
ACA-A1	96.9		88.0	ACA-A1	87.5		71.0
		90.0				60.0	
ACA-A2	56.3		35.0	ACA-A2	46.9		0
PCA-P1	90.6		82.0	PCA-P1	56.3		71.0
		60.0				20.0	
PCA-P2	65.6		77.0	PCA-P2	3.1		12.0

*: with contrast injection; ^: not measured. [1]: Delcker & Turowski, 1997; [2]: Ivancevich et al., 2008.

4.3.2 The hemodynamics of the CoW delivered by UBA: the direction of blood flow

The determination of blood flow direction within the vessels was achieved through the manipulation of various vision planes, as depicted in **Figure 4-3**. These planes were marked by the presence of a green region or a green dotted line. The red color corresponded to the direction of blood flow towards the transducer, while the blue color denoted blood flow moving away from the transducer. **Figure 4-3 (a)** demonstrates a reversal of blood flow directions in the symmetrical components of the CoW. Specifically, the red hue indicates blood flow in the ipsilateral ACA-A1, whereas the blue color represents blood flow in the contralateral ACA-A1. The identical phenomenon was also observed in PCA-P1 and MCA. In ACA-A2, the presence of the blue color was observed, indicating the origin of blood from ACA-A1s and its subsequent flow towards the

upper region. The directional information was made apparent using UBA by adjusting the plane on a specific vessel, for example the ICA at the ipsilateral side (as shown in **Figure 4-3 (b)**). The plane adjustment is indicated by the green dotted line.

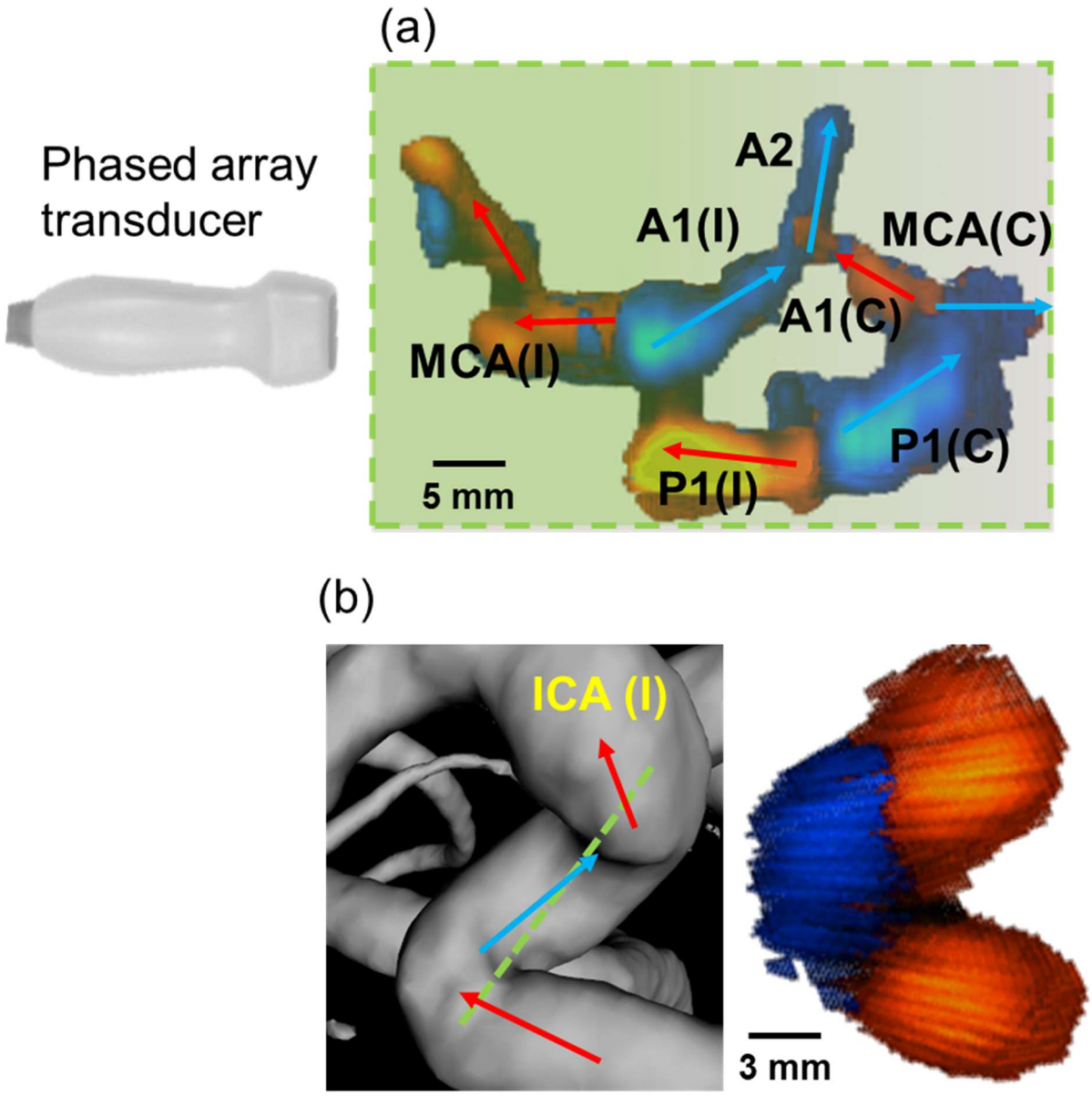

Figure 4-3. The directional information was detected using UBA on (a) the whole CoW and (b) a specific vessel, the ICA, at the ipsilateral side. Arrows with different colors are used to identify the directions of the blood flow in the vessels. The green region in (a) represents the coronal plane of the CoW for visualization, and the green dashed line in (b) is the sagittal plane of the vessel for visualization.

4.3.3 The hemodynamics of the CoW delivered by UBA: the velocity of blood flow

Within the context of Color Power Imaging (CPI), the luminosity of the color depicted in the color map corresponds to the magnitude of the Doppler signal, which is also indicative of the velocity. In order to investigate the effect of velocity variation on the observed color in the dCPI mode, the velocity scale was adjusted from 38 cm/s to 21 cm/s. Subsequently, the peak systolic velocity (PSV) was measured at the identical location inside the vessel. All the details are depicted in **Figure 4-4 (a)** and **(b)**. The center of the vessel had an average PSV of 54.66 cm/s. However, the phenomenon of aliasing was observed exclusively when the velocity scale was adjusted to 21 cm/s. Aliasing was also observed in the reconstructed blood flow, as evidenced by the presence of a bigger aliasing zone in the contralateral PCA-P1, as depicted in **Figure 4-4 (c)**.

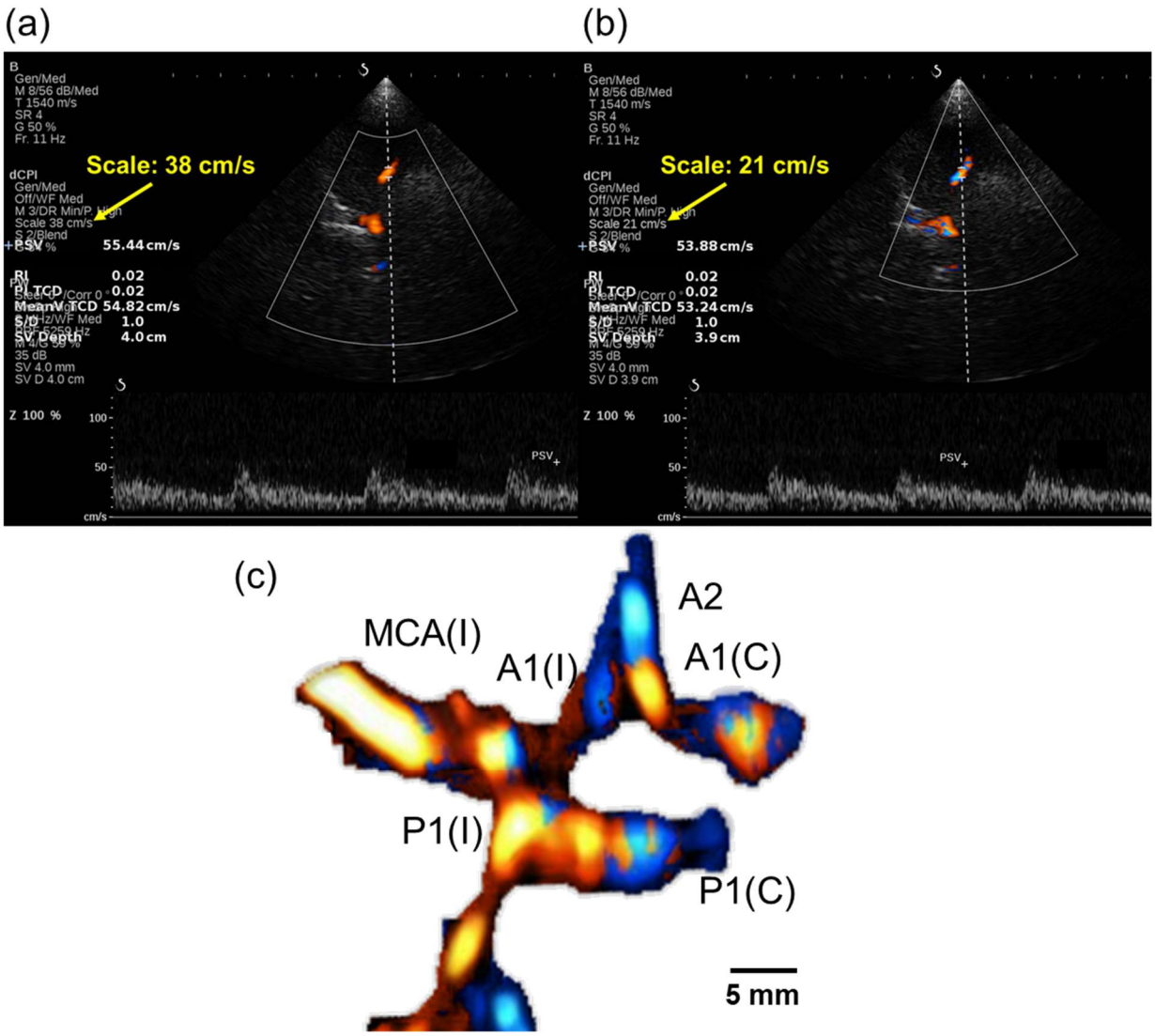

Figure 4-4. The presented colors were compared under different settings of the velocity scale, (a) 38 cm/s and (b) 21 cm/s. (c) The aliasing region was also detectable in the reconstructed CoW, and here a larger aliasing region was found in the contralateral PCA-P1 of a represented subject.

4.4 Discussion

The objective of this study was to examine the diagnostic efficacy of our newly developed 3D TCCD imaging system, which is called UBA. The utilization of 2D TCCD is a common practice in clinical settings to obtain both anatomical and hemodynamic data pertaining to the CoW. Therefore, the UBA imaging system underwent the same validation process to acquire

information. When compared to MRA, the novel system exhibited excellent capability to generate a comprehensive three-dimensional representation of the CoW. This visualization encompasses the internal carotid arteries, middle cerebral arteries, anterior cerebral arteries, and posterior cerebral arteries on both ipsilateral and contralateral sides. The study observed that the new technology demonstrated improved efficacy in identifying ipsilateral vessels in the visualization of cerebral arteries, when compared to previous approaches such as non-enhanced 3D-PDI and contrast-enhanced 3D-CFI via a 2D-array transducer (Delcker & Turowski, 1997; Ivancevich et al., 2008). Despite a significant decrease in the detection rate on the contralateral side, UBA yielded superior outcomes compared to non-enhanced 3D-PDI. The aforementioned decline can be mitigated through the administration of contrast injection, as the implementation of contrast-enhanced 3D-CFI via a 2D-array transducer yielded significantly improved results in terms of the detection rate on the contralateral side. Significantly, the notable capacity to detect ICAs distinguishes UBA as exceptional compared to other methodologies.

The coded colors allowed for the observation of hemodynamic information, such as blood flow direction and velocity. The novel methodology additionally facilitates the differentiation of blood flow directions from both a comprehensive perspective and inside individual vessels through the adjustment of visualization planes, as depicted in **Figure 4-3**. In order to better support the operators and doctors in detecting abnormalities in blood flow, a larger number of frames were collected for a comprehensive 3D reconstruction in UBA. Specifically, around 1,000 frames were utilized, which is more than six times the number of frames reported in 3D-PDI (around 150 frames). In addition to providing directional information, the velocity of blood flow might be determined by detecting the region of aliasing. The findings from **Figure 4-4 (a)** and **(b)** provide evidence that the imaging mode of dCPI remains constrained by the Nyquist limits. Aliasing is

observed when the velocity scale is reduced, because of the blood speed beyond the Nyquist threshold (Maulik, 2005). Therefore, the presence of any aliasing zone inside the three-dimensional CoW may indicate an increased velocity of blood flow within that particular location. It may be recommended to perform additional spectral Doppler examinations using either pulsed wave (PW) or continuous wave (CW) techniques in order to monitor the precise velocity of blood flow at the spot where aliasing occurs.

Limitation: The dCPI still shows a poor image resolution compared with the ultrasonic localization microscope (ULM) technology. The ULM was recently verified in a human patient, demonstrating its ability to map the cerebrovascular network with micrometer-scale resolution and analyze its hemodynamics in a 2D image (Demené et al., 2021). The utilization of this technology in 3D reconstruction would represent a significant advancement. Nevertheless, the challenging nature of this approach stemmed from the long duration of 24 seconds each frame during the acquisition process, as well as the requirement for the presence of microbubbles. This was further compounded by the necessity of capturing hundreds, or even thousands, of frames for the purpose of 3D reconstruction, while the effects of the contrast injection would only endure for a limited duration of minutes. Hence, the application of ULM for constructing a three-dimensional representation of the cerebrovascular network is not currently viable for clinical implementation in the near future. In contrast, the UBA system included ultrasonic imaging equipment that possessed dCPI functionality and a single-crystal phased array transducer. Therefore, it is unnecessary to create an entirely new system; rather, the focus should be on the implementation of scanning and processing techniques. Hence, it is plausible that UBA might be readily implemented in clinical settings, notwithstanding the need for more clinical investigations to establish its efficacy in diagnosing various illnesses associated with CoW abnormalities.

4.5 Summary

The existing 3D TCCD techniques, 3D-PDI and 3D-CFI via a 2D-array transducer, suffer either from a lack of hemodynamic information or inadequate vascular detection rate, both of which are crucial in the current medical era.

Our newly developed 3D TCCD system, UBA, aims to overcome the abovementioned limitations by applying a phased array made of a single crystal and an imaging mode of dCPI. dCPI is an advanced imaging mode that combines the flow direction information provided by CFI with the high sensitivity of the Doppler amplitude signal supplied by CPI/PDI. Theoretically, UBA is capable of achieving improved sensitivity in detecting blood flow while simultaneously providing directional information.

In this section, the UBA system was applied to 32 healthy elderly individuals, consisting of 21 men and 11 women, with a mean age of 65.8 years. The detection rates of cerebral vessels within the CoW were calculated and compared with previous 3D TCCD studies, non-enhanced 3D-PDI and contrast-enhanced 3D-CFI via a 2D-array transducer. Meanwhile, the hemodynamic information, such as the blood flow direction and velocity, was also evaluated using our UBA system.

In conclusion, our approach effectively depicted a significant portion of both ipsilateral and contralateral cerebral arteries in the CoW. The utilization of the UBA system resulted in superior detection rates for ipsilateral vessels as compared to the implementation of non-enhanced 3D-PDI and contrast-enhanced 3D-CFI via a 2D-array transducer. In addition, the UBA system also successfully captured and visualized 3D hemodynamic information, including flow direction and velocity. This information was effectively delivered utilizing coded color and aliasing regions. Therefore, the UBA approach fulfills the requirements for clinical application as it offers a

relatively thorough and dependable depiction of the anatomical structure of the CoW and provides its hemodynamics.

Chapter 5 Comparison of the Similarity Measure Between UBA and MRA for Evaluating the Performance of UBA

(This chapter was modified from our under-review paper "S. Li, C. P. Y Wan, Q. T. K. Shea, Y. T. Ling, X. Y. Chen and Y. P. Zheng, A Novel 3D Transcranial Color Doppler System Enhances Vascular Detection Rate with Hemodynamic Captures, Computers in Biology and Medicine, CIBM-D-23-13146".)

5.1 Introduction

Owing to its non-invasiveness, cost-effectiveness, higher accessibility, absence of ionizing radiation, and superior time resolution, 2D TCCD is used in clinics to assess the normalcy of the cerebral arteries in the Circle of Willis (CoW) by detecting the hemodynamics of visible structures, including blood flow velocity and direction (McKiernan & Selmes, 2017). Later, the techniques of 3D TCCD were developed to deliver high-dimensional information, such as 3D-PDI (Bauer et al., 1998; Delcker & Turowski, 1997; Huang & Zeng, 2017; Klötzsch et al., 1999, 2002) and 3D-CFI via a 2D-array transducer (Ivancevich et al., 2008; Lindsey et al., 2009). However, these techniques suffer from either a lack of hemodynamic information or inadequate vascular detection rate.

The objective of our recently created 3D TCCD system, named UBA, is to address the aforementioned limitations by utilizing a single-crystal phased array and employing an imaging mode known as dCPI. The dCPI imaging mode is an advanced technique that integrates the flow

direction information from CFI mode with better sensitivity of the Doppler amplitude signal obtained from the CPI/PDI mode (Hoskins et al., 2019). Therefore, the utilization of UBA can improve the sensitivity in the detection of blood flow, while also offering directional information, which have been proved in **Chapter 4**. However, few studies have examined the quantitative differences in transcranial 3D reconstruction using 3D TCCD systems. Therefore, there is an urgent need to quantitatively analyze the reconstructed CoW generated by 3D TCCD. **The aim of this chapter was to expose the quantitative difference in transcranial 3D reconstruction generated by UBA systems.**

In this section, a quantitative comparison was conducted between the UBA system and standardized cerebral Magnetic Resonance Angiography (MRA). A total of six out of 32 subjects were scanned via MRA. The procedure of skeletonization was employed to obtain the centerline of both UBA and MRA while ensuring the preservation of their topology. Subsequently, an assessment of performance of UBA was conducted through the utilization of a similarity metric, specifically the average Hausdorff distance. Our results would suggest the great reliability of UBA and strongly support its compatibility in future clinical applications.

5.2 Materials and methods

5.2.1 Optimal skeletonization in both UBA and MRA for further comparison

Prior to obtaining the skeletons of the cerebral blood flow reconstructed using both UBA and MRA, point clouds of MRA were standardized to conform to the same format as UBA. Consequently, distinct thresholding ranges of the grayscale were employed to segregate the cerebral blood flow region from the 3D MRA data (DICOM) for each participant. The required

thresholding ranges were provided by medical software (InVesalius 3, CTI Renato Archer, Campinas, Sao Paulo, Brazil), which was utilized for the reconstruction of anatomical structures within the human body, including brain vessels. The point cloud data set obtained using MRA exhibited a resolution of 0.30 mm/pixel along the z-axis and 0.48 mm/pixel along the x and y axes, where pixel refers to dots per millimeter (DPM). **Figure 5-1** displays the representative point clouds of UBA and MRA. **Figure 5-2** depicts the methodology employed to optimize the skeletonization process. The boundary of the point cloud produced by UBA was utilized to extract the region of interest from the point cloud of MRA. Both point clouds were then downsampled into a three-dimensional matrix by dividing the DPM of 0.33 mm per voxel, as depicted in **Figure 5-2 (a)** and **(b)**. The pre-skeletonization process involved extracting the centerline while maintaining the topological structure of the objects, as depicted in **Figure 5-2 (c)** and **(d)**. In order to facilitate a more rigorous quantitative comparison, certain outliers of branches in the skeletons were excluded, as depicted in **Figure 5-2 (e)** and **(f)**.

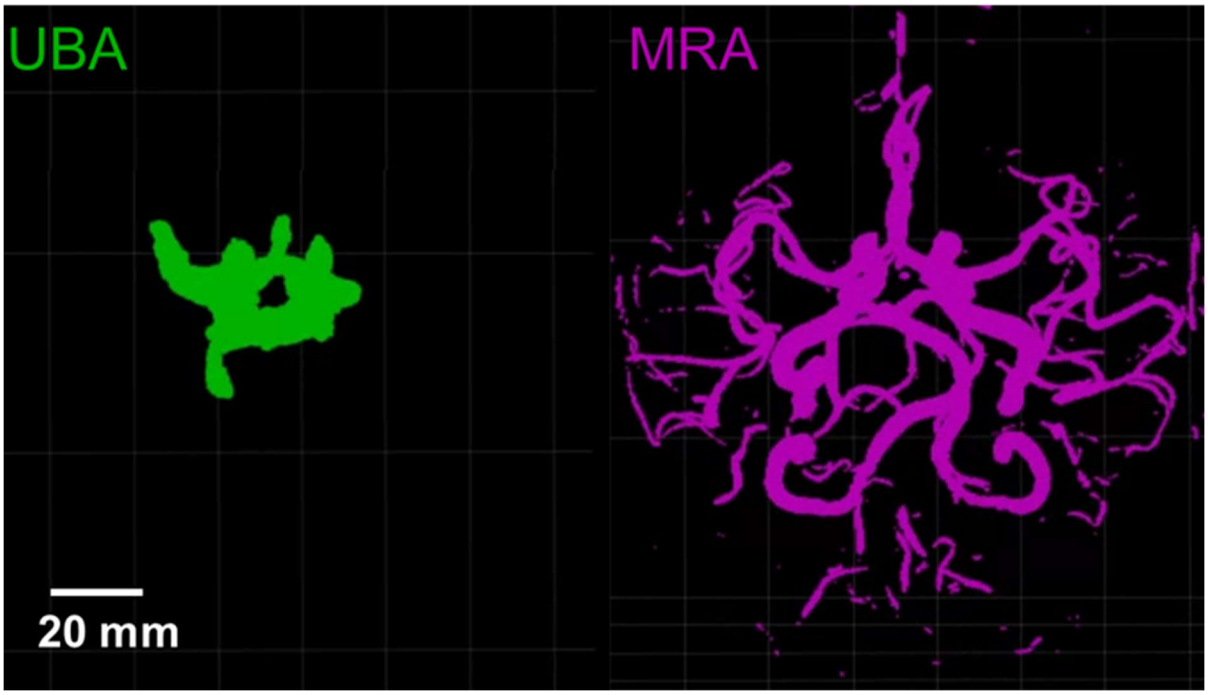

Figure 5-1. The real-scaled point clouds of UBA and MRA are marked with a scale bar.

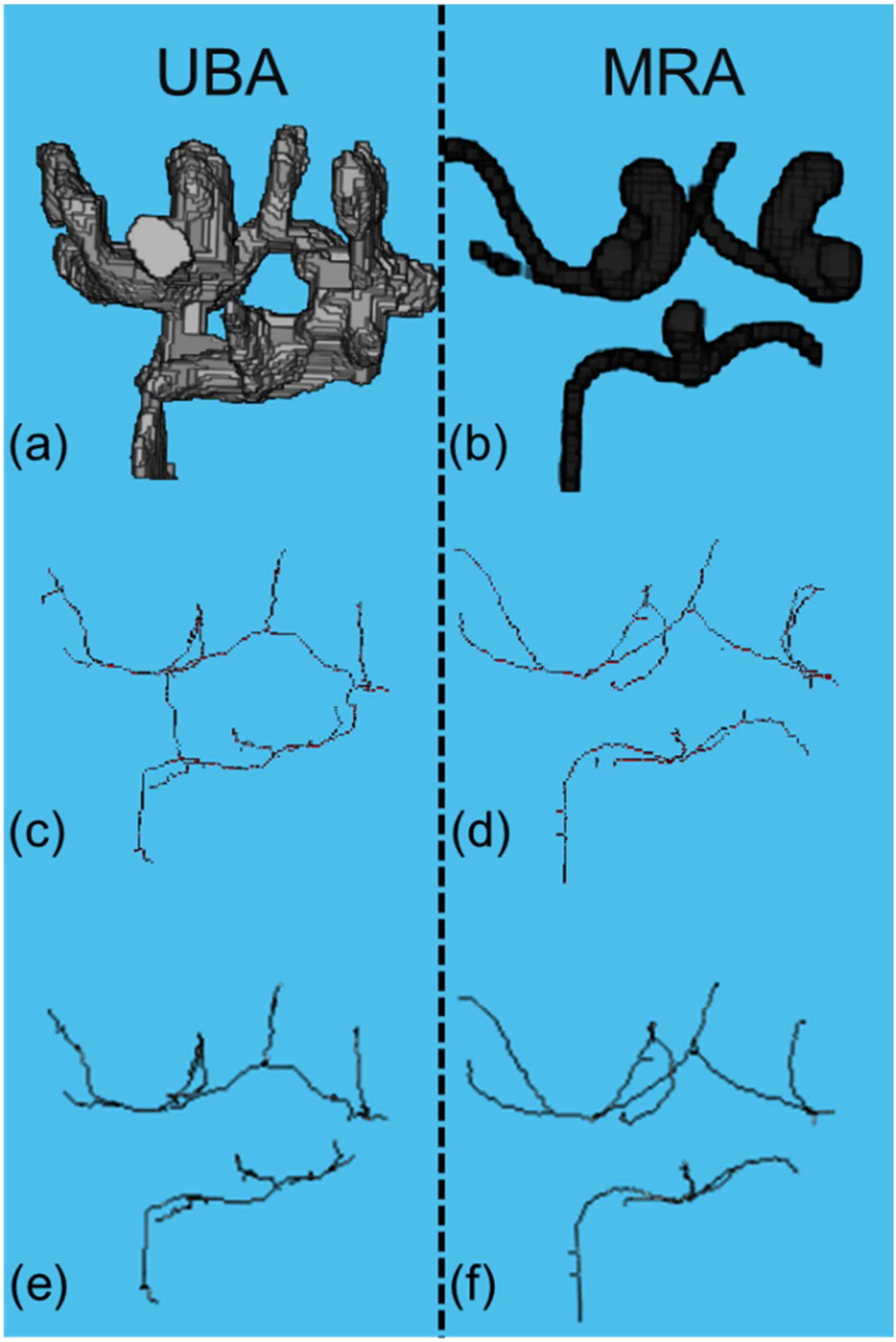

Figure 5-2. (a-b) Indication that two sets of point clouds of ROI were respectively downsampled into a 3D matrix of 150*91*130 by dividing the DPM of 0.33 mm/voxel. (c-d) the first step of skeletonization by extracting the centerline but preserving the topology. (e-f) the last step of skeletonization by removing the outliers of some branches for further quantitative comparison.

5.2.2 Strategy to test the performance of UBA: the similarity measure

The Hausdorff distance is a metric that calculates the greatest distance between each point in one set and its closest point in another set. It is commonly employed in the field of geometry to measure the similarity between two-dimensional and three-dimensional objects (Zhang et al., 2017; Ryu & Kamata, 2021). Nevertheless, the utilization of the Hausdorff distance as the metric was constrained due to its sole provision of the maximum discrepancy between two geometric entities. The present study utilized the average Hausdorff distance metric to consider all the closest distances between pairs of points, as previously specified in a prior study (Aydin et al., 2021).

Following the process of skeletonization, the optimal skeletal structures of the CoW were preserved in two distinct sets of coordinates. The flowchart depicted in **Figure 5-3** outlines the approach for rectifying the positional accuracy of the coordinate set of UBA. The mean distance, in this context, is the same as the average Hausdorff distance.

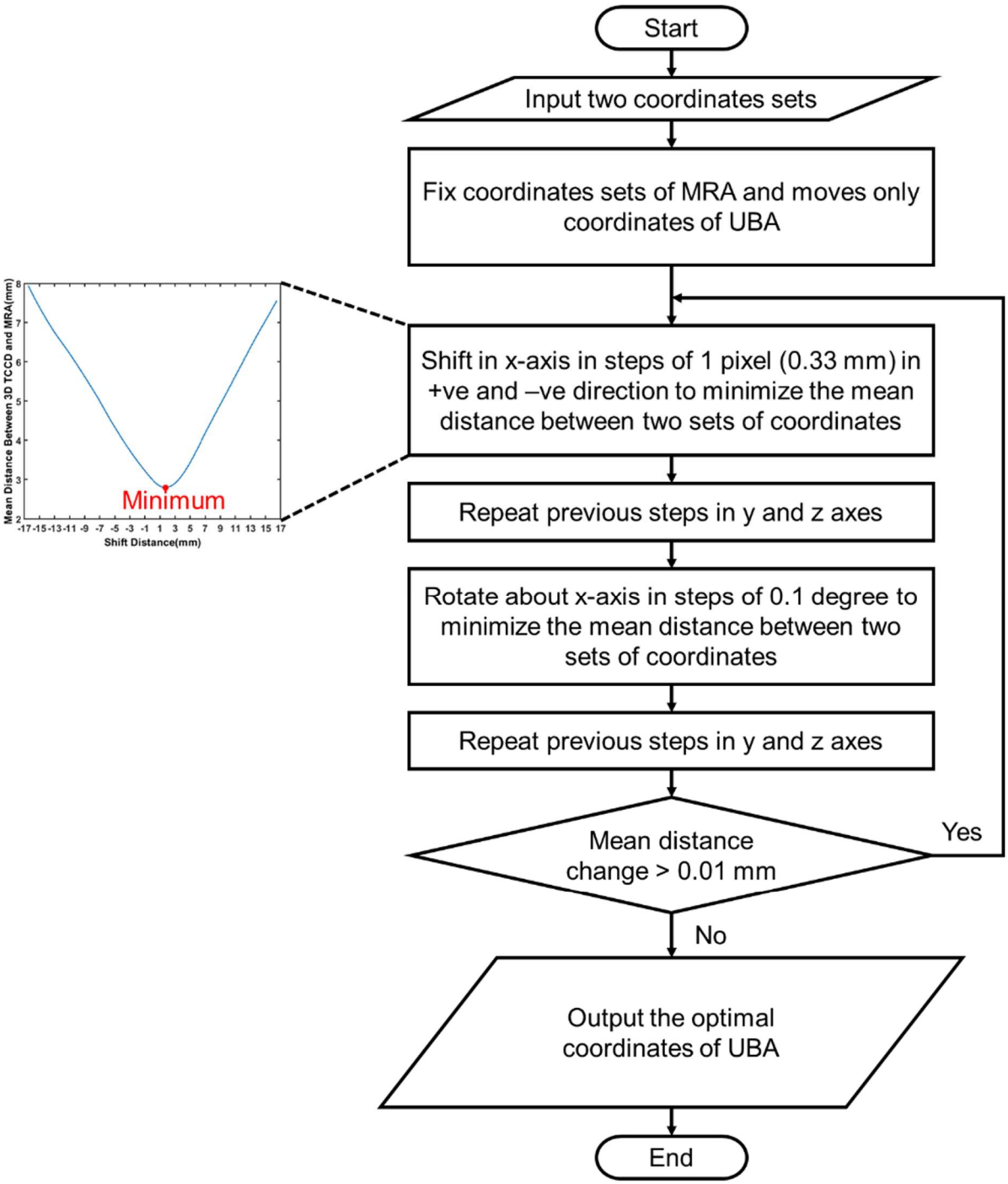

Figure 5-3. The flowchart demonstrates the procedure to correct the location of the CoW generated by UBA. The coordinate set of MRA was fixed as the reference, and then the coordinate set of UBA was shifted and rotated in the x, y, z axes with steps of 0.33 mm and 0.1 degree respectively until the change of the average Hausdorff distance was less than 0.01 mm. The outputs were the optimized coordinate set of UBA, and its Hausdorff distance and average Hausdorff distance refer to MRA.

5.2.3 Data analysis and statistics

The skeletonization and similarity measure were performed using a custom MATLAB script (MathWorks Inc., Natick, MA, USA). The statistical analyses were conducted using GraphPad Prism 9 software (GraphPad Software Inc., LaJolla, CA, USA).

5.3 Results

5.3.1 The similarity measure between UBA and MRA: average Hausdorff distance

Following the adjustment of the location, the optimum set of coordinates for UBA was graphed and subsequently compared to MRA, as depicted in **Figure 5-4**. The data obtained from a sample of six human individuals were subjected to analysis. The average Hausdorff distance was then computed: the average Hausdorff distance obtained for subject one was 1.91 mm, subject two gave an average Hausdorff distance of 2.24 mm, subject three gave an average Hausdorff distance of 1.97 mm, subject four gave an average Hausdorff distance of 2.81 mm, subject five gave an average Hausdorff distance of 2.57 mm, and subject six gave an average Hausdorff distance of 2.21 mm.

Hence, an average discrepancy of 2.29 mm was found in terms of distance between UBA and MRA.

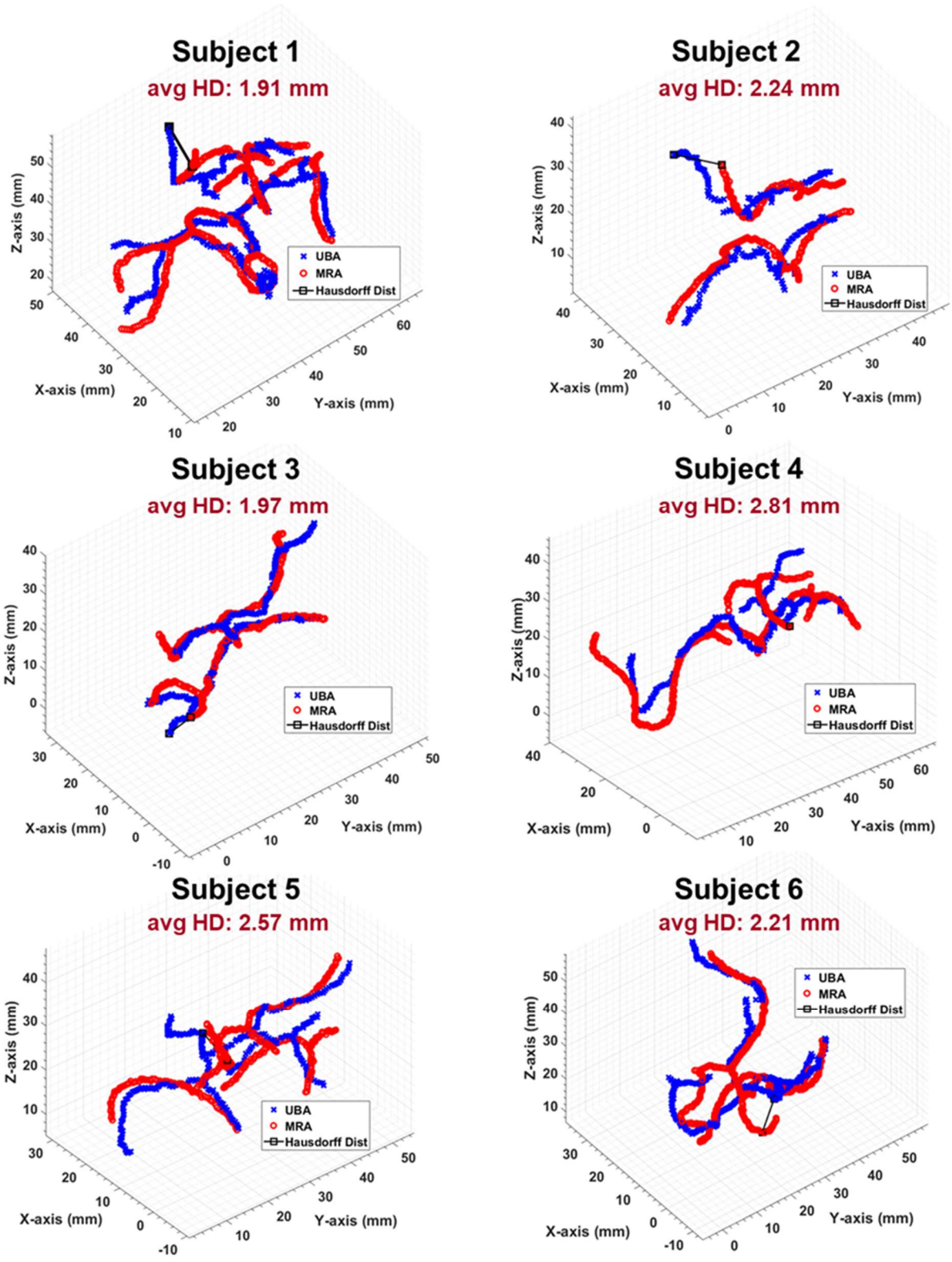

Figure 5-4. The plots show the optimal similarity measure after the location correction of the coordinate set of UBA. The blue line with cross markers is the coordinate set of UBA, and the red line with circle markers represent the coordinate set of MRA. The Hausdorff distance is also highlighted to demonstrate the location of the largest distance difference between UBA and MRA.

5.3.2 Visualizing Distribution and Probability Density: violin plot

Additional information regarding the distribution of the shortest distance can be observed in **Figure 5-5**, wherein the violin plots are depicted. The location of the Hausdorff distance is evident in its definition, which states that it represents the maximum distance between points in the point set of UBA/MRA and their nearest neighbor points in the point set of MRA/UBA. Significantly, the line of median indicates that the majority of closest distances, regardless of the calculation direction from UBA to MRA or from MRA to UBA, were less than 2 mm.

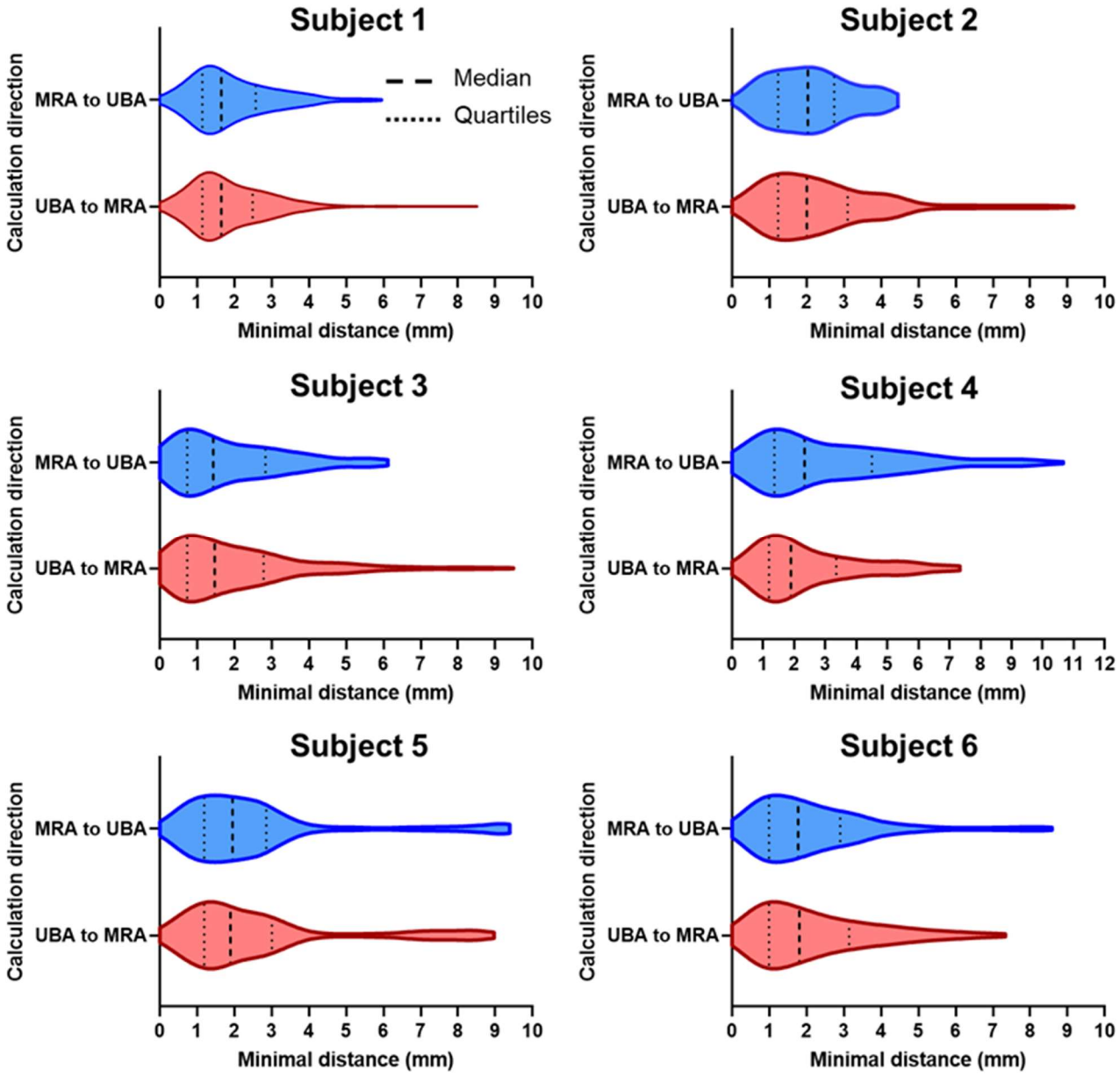

Figure 5-5. The violin plots demonstrate the detailed distribution of the closest distances between two sets of point cloud. The thick dotted line is the line of the median, and the thin dotted lines indicate the quartile distribution of 25% and 75%.

5.4 Discussion

This work represents the first attempt to compare 3D TCCD with standardized cerebral MRA. The results demonstrate that there was an average difference of 2.29 mm in the distance between

UBA and MRA. Meanwhile, the violin plots consistently indicated that the majority of closest distances, irrespective of the direction of computation (from UBA to MRA or from MRA to UBA), were found to be less than 2 mm. This would serve as empirical evidence of the heightened reliability of UBA and offer strong support for its appropriateness in prospective clinical applications. Noteworthy is that this mean difference was most likely affected by the color overrepresentation/enlargement, as investigated in Chapter 3. Therefore, it is worth exploring more how the size of the reconstructed CoW can be improved by refining interdependent or independent factors and any calibration method using ratio values. Besides the factors of vascular diameter, flow velocity, Doppler interrogation depth, the settings speed/velocity scale and color gain studied in Chapter 3, more factors, such as wall filter, transducer frequency, frame rate, etc., should be included to determine their effects on color overrepresentation. Moreover, the alignment strategy used to test the performance of UBA is somehow a brute-force approach. Our UBA system may perform better than 2.29 mm of mean difference if a more proper alignment method could be applied.

On the other hand, UBA may offer a potential advantage in terms of offering more information about PCoA, as illustrated in **Figure 5-6**. This advantage arises due to the challenges faced by MRA in accurately capturing PCoA, mostly due to its limited dimensions and orientation that is typically perpendicular to the direction of MRA scanning. Consequently, the skeletal component of PCoA in UBA was primarily eliminated throughout the process of skeletonization.

Limitations: the sample size of the subjects who underwent both UBA and MRA should be increased, as only six were included in this study. Meanwhile, all the subjects recruited in this study were healthy, so more patients with cerebral aneurysms or symptoms of a stroke should be

involved in future studies. There is a need for more clinical investigations to establish its efficacy in diagnosing various illnesses associated with CoW abnormalities.

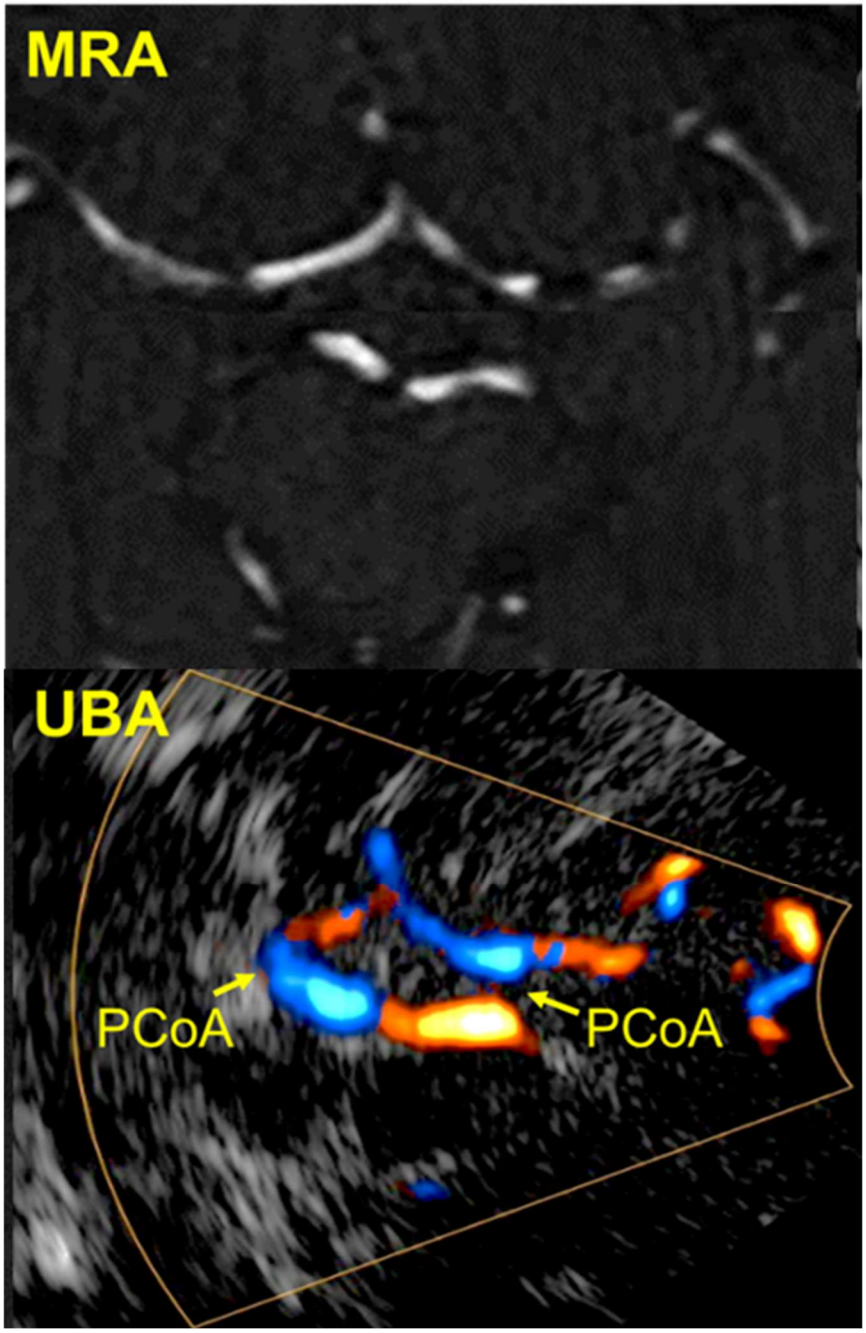

Figure 5-6. The thin vessel, PCoA, was captured by UBA, but MRA could not do so. The 2D raw images via MRA and UBA were from one representative subject.

5.5 Summary

Since few studies have examined the quantitative differences in transcranial 3D reconstruction using 3D TCCD systems, there is an urgent need to quantitatively analyze the reconstructed CoW generated by 3D TCCD.

In this section, a quantitative comparison was undertaken to evaluate the difference between UBA and standardized cerebral MRA. Six individuals underwent MRA scanning. The process of skeletonization was utilized to acquire the centerline of both UBA and MRA, while simultaneously maintaining the preservation of their topology. Following this, an evaluation was carried out to assess the performance of UBA, in comparison with MRA. This evaluation involved the use of a similarity metric, namely the average Hausdorff distance. In conclusion, the analysis demonstrated a mean difference of 2.29 mm in the average Hausdorff distance between UBA and MRA. The findings of our study indicate a high level of reliability for UBA and provide solid evidence for its potential compatibility in forthcoming clinical applications.

Chapter 6 Conclusions and Future Directions

The present study aimed to develop a novel 3D TCCD imaging system, referred to as ultrasound brain angiography, UBA. This system utilized a phased array transducer made of a single crystal to improve the sensitivity of Doppler ultrasound. Additionally, an advanced color mode known as directional color power imaging, dCPI, was implemented, which combined better sensitivity of CPI/PDI with the directional information provided by CFI.

In the first part, a phantom study was conducted to examine the effects of several factors related to flow imaging, including vascular diameter (2 mm, 4 mm, 6 mm), flow velocity (20.33 cm/s, 29.67 cm/s, 38.91 cm/s, 50.24 cm/s), Doppler interrogation depth (3 cm, 6 cm, 9 cm), and settings of color gain and velocity scale (matched group and unmatched group), on the occurrence of color overrepresentation/enlargement on the 3D reconstruction generated by UBA. Meanwhile, the absolute error and the ratio of the reconstructed diameter to the actual diameter were calculated for comparison. In the second part, the UBA system was employed to scan a cohort of 32 older healthy adults to determine the performance of the UBA system, in comparison with MRI. The detection rates of cerebral vessels within the CoW were computed and compared to those reported in earlier studies, specifically using 3D-PDI and 3D-CFI via a 2D-array transducer. In addition, our UBA system was utilized to assess hemodynamic information, including blood flow direction and velocity. The final part of the study aimed to explore the quantitative difference in transcranial 3D reconstruction generated by UBA systems in comparison with MRI results. A total of six participants, who were earlier scanned by the UBA system, received an MRA scan. The technique of skeletonization was executed in order to extract the centerline of both UBA and MRA, while

ensuring the preservation of their respective topology. Subsequently, the performance of UBA was assessed, which computed a similarity metric known as the average Hausdorff distance.

In summary, the following achievements have been made in this study:

- In developing the UBA system, a single-crystal phased array transducer and imaging mode of dCPI were employed to achieve good Doppler sensitivity together with the capability of hemodynamic capture. Additionally, rotational scanning was used for data acquisition to provide a more comprehensive view of imaging.
- There is a persistent phenomenon of color overrepresentation in the reconstructed objects. However, it may be conceivable that this limitation can be overcome through the refinement of interdependent or independent factors or by implementing calibration methods that leverage ratio values.
- The UBA system gives a relatively complete anatomical structure of the CoW, along with more comprehensive information on its hemodynamics.
- A mean difference of 2.29 mm in average Hausdorff distance between UBA and MRA would suggest a great reliability of the UBA system.

Based on what has been achieved in this study, future research works can be followed up in the areas of enhancing scanning and processing techniques to realize the potential of the proposed UBA system as a clinical tool. The data acquisition by UBA in this study was limited to the temporal window on the optimal side (either left or right). By utilizing spatial sensors and two sets of scanning setups, it may be feasible to perform 3D TCCD concurrently on both the left and right sides. This approach may offer a more comprehensive anatomical structure of the CoW due to the typically higher vascular detection rates on the ipsilateral side. During the data collection from

subjects, we noted that the Doppler signals for some cases were relatively low due to the large attenuation caused by the skull, leading to poor images of the vessels. Injecting contrast agent is an additional approach to enhance the detection rates of cerebral vessels in future studies. It is essential to evaluate the vascular detection rate and similarity measure in comparison with MRA with and without the use of the contrast. Moreover, the DICOM image format with 12 – 16 bits per pixel is more precise than AVI-based data (8 bits per pixel). Using DICOM-based data in future would potentially mitigate or minimize color overrepresentation by applying the thresholding method.

Another critical research direction is the accuracy improvement in the structure of the reconstructed CoW. The mean difference reported in Chapter 5 is most likely affected by the color overrepresentation/enlargement. The factors of vascular diameter, flow velocity, Doppler interrogation depth, and settings of speed/velocity scale and color gain were investigated in Chapter 3 to determine their effects on color overrepresentation. It may be essential to explore more how the size of the reconstructed CoW can be improved by the refinement of interdependent or independent factors and any calibration method using ratio values. Meanwhile, more factors, such as wall filter, transducer frequency, frame rate, etc., should be included for study as well.

Furthermore, there is a need for more clinical investigations to establish the efficacy of UBA system in diagnosing various illnesses associated with CoW abnormalities. On one hand, the sample size of the subjects who underwent both UBA and MRA should be increased, as only six were included in this study. On the other hand, more patients (with cerebral aneurysms or symptoms of a stroke) should be involved in future studies to validate the performance of the UBA system as a tool for stroke risk assessment.

References

Aaslid, R., Markwalder, T.-M., & Nornes, H. (1982). Noninvasive transcranial Doppler ultrasound recording of flow velocity in basal cerebral arteries. *Journal of neurosurgery*, *57*(6), 769-774.

Adams Jr, H. P., Bendixen, B. H., Kappelle, L. J., Biller, J., Love, B. B., Gordon, D. L., & Marsh 3rd, E. (1993). Classification of subtype of acute ischemic stroke. Definitions for use in a multicenter clinical trial. TOAST. Trial of Org 10172 in Acute Stroke Treatment. *Stroke*, *24*(1), 35-41.

Agarwal, N., & Carare, R. O. (2021). Cerebral vessels: an overview of anatomy, physiology, and role in the drainage of fluids and solutes. *Frontiers in neurology*, *11*, 611485.

Agarwal, N., Contarino, C., & Toro, E. F. (2019). Neurofluids: a holistic approach to their physiology, interactive dynamics and clinical implications for neurological diseases. *Veins and Lymphatics*, *8*(3).

Alexandrov, A. V., Sloan, M. A., Wong, L. K., Douville, C., Razumovsky, A. Y., Koroshetz, W. J., Kaps, M., Tegeler, C. H., & Committee, A. S. o. N. P. G. (2007). Practice standards for transcranial Doppler ultrasound: part I—test performance. *Journal of Neuroimaging*, *17*(1), 11-18.

Alfidi, R., Masaryk, T., Haacke, E., Lenz, G., Ross, J., Modic, M., Nelson, A., LiPuma, J., & Cohen, A. (1987). MR angiography of peripheral, carotid, and coronary arteries. *American Journal of Roentgenology*, *149*(6), 1097-1109.

Allendoerfer, J., Goertler, M., & von Reutern, G.-M. (2006). Prognostic relevance of ultra-early doppler sonography in acute ischaemic stroke: a prospective multicentre study. *The Lancet Neurology*, *5*(10), 835-840.

Anselmino, M., Malmberg, K., Öhrvik, J., Rydén, L., & Investigators, E. H. S. (2008). Evidence-based medication and revascularization: powerful tools in the management of patients with diabetes and coronary artery disease: a report from the Euro Heart Survey on diabetes and the heart. *European Journal of Preventive Cardiology*, *15*(2), 216-223.

Anxionnat, R., Bracard, S., Ducrocq, X., Trousset, Y., Launay, L., Kerrien, E., Braun, M., Vaillant, R., Scomazzoni, F., & Lebedinsky, A. (2001). Intracranial aneurysms: clinical

value of 3D digital subtraction angiography in the therapeutic decision and endovascular treatment. *Radiology*, *218*(3), 799-808.

Appel, L. J., Brands, M. W., Daniels, S. R., Karanja, N., Elmer, P. J., & Sacks, F. M. (2006). Dietary approaches to prevent and treat hypertension: a scientific statement from the American Heart Association. *Hypertension*, *47*(2), 296-308.

Aviv, R., Shelef, I., Malam, S., Chakraborty, S., Sahlas, D., Tomlinson, G., Symons, S., & Fox, A. (2007). Early stroke detection and extent: impact of experience and the role of computed tomography angiography source images. *Clinical radiology*, *62*(5), 447-452.

Aydin, O. U., Taha, A. A., Hilbert, A., Khalil, A. A., Galinovic, I., Fiebach, J. B., Frey, D., & Madai, V. I. (2021). On the usage of average Hausdorff distance for segmentation performance assessment: hidden error when used for ranking. *European radiology experimental*, *5*, 1-7.

Balami, J., Chen, R., & Buchan, A. (2013). Stroke syndromes and clinical management. *QJM: An International Journal of Medicine*, *106*(7), 607-615.

Banerjee, C., Moon, Y. P., Paik, M. C., Rundek, T., Mora-McLaughlin, C., Vieira, J. R., Sacco, R. L., & Elkind, M. S. (2012). Duration of diabetes and risk of ischemic stroke: the Northern Manhattan Study. *Stroke*, *43*(5), 1212-1217.

Banga, P. V., Varga, A., Csobay-Novák, C., Kolossváry, M., Szántó, E., Oderich, G. S., Entz, L., & Sótonyi, P. (2018). Incomplete circle of Willis is associated with a higher incidence of neurologic events during carotid eversion endarterectomy without shunting. *Journal of Vascular Surgery*, *68*(6), 1764-1771.

Bartels, E. (2012). Transcranial color-coded duplex ultrasonography in routine cerebrovascular diagnostics. *Perspectives in Medicine*, *1*(1-12), 325-330.

Baskin, A., Buchegger, F., Seimbille, Y., Ratib, O., & Garibotto, V. (2015). PET molecular imaging of hypoxia in ischemic stroke: an update. *Current vascular pharmacology*, *13*(2), 209-217.

Bauer, A., Bogdahn, U., Haase, A., & Schlief, R. (1998). 3-Dimensional echo-enhanced transcranial Doppler ultrasound diagnosis. *Der Radiologe*, *38*(5), 394-398.

Baumgartner, R. W., Arnold, M., Gönner, F., Staikow, I., Herrmann, C., Rivoir, A., & Müri, R. M. (1997). Contrast-enhanced transcranial color-coded duplex sonography in ischemic cerebrovascular disease. *Stroke*, *28*(12), 2473-2478.

Baumgartner, R. W., Mattle, H. P., & Schroth, G. (1999). Assessment of≥ 50% and< 50% intracranial stenoses by transcranial color-coded duplex sonography. *Stroke*, *30*(1), 87-92.

Becks, M. J., Manniesing, R., Vister, J., Pegge, S. A., Steens, S. C., van Dijk, E. J., Prokop, M., & Meijer, F. J. (2019). Brain CT perfusion improves intracranial vessel occlusion detection on CT angiography. *Journal of Neuroradiology*, *46*(2), 124-129.

Bergman, R. A., Afifi, A. K., & Miyauchi, R. (2005). Circle of Willis. *Illustrated Encyclopedia of Human Anatomic Variation: Opus II: Cardiovascular System: Arteries: Head, Neck, and Thorax.[Electronic resource]. URL: https://www. anatomyatlases. org/AnatomicVariants/Cardiovascular/Text/Arteries/CircleofWillis. shtml (last accessed data: 26.05. 2020)*.

Berland, L. L., Bryan, C. R., Sekar, B. C., & Moss, C. N. (1988). Sonographic examination of the adult brain. *Journal of Clinical Ultrasound*, *16*(5), 337-345.

Boehme, A. K., Esenwa, C., & Elkind, M. S. (2017). Stroke risk factors, genetics, and prevention. *Circulation research*, *120*(3), 472-495.

Bogdahn, U., Becker, G., Winkler, J., Greiner, K., Perez, J., & Meurers, B. (1990). Transcranial color-coded real-time sonography in adults. *Stroke*, *21*(12), 1680-1688.

Boujan, T., Neuberger, U., Pfaff, J., Nagel, S., Herweh, C., Bendszus, M., & Möhlenbruch, M. (2018). Value of contrast-enhanced MRA versus time-of-flight MRA in acute ischemic stroke MRI. *American Journal of Neuroradiology*, *39*(9), 1710-1716.

Brisman, J. L., Song, J. K., & Newell, D. W. (2006). Cerebral aneurysms. *New England Journal of Medicine*, *355*(9), 928-939.

Burgess, R. E., & Kidwell, C. S. (2011). Use of MRI in the assessment of patients with stroke. *Current neurology and neuroscience reports*, *11*, 28-34.

Carrizosa, J. (2021). Transcranial Doppler (TCD/TCCS) Approaches: Acoustic Windows. In *Neurosonology in Critical Care: Monitoring the Neurological Impact of the Critical Pathology* (pp. 177-194). Springer.

Cavalcanti, D. D., Feindel, W., Goodrich, J. T., Dagi, T. F., Prestigiacomo, C. J., & Preul, M. C. (2009). Anatomy, technology, art, and culture: toward a realistic perspective of the brain. *Neurosurgical focus*, *27*(3), E2.

Cereda, C., & Carrera, E. (2012). Posterior cerebral artery territory infarctions. *Manifestations of Stroke*, *30*, 128-131.

Chan, M. Y.-M., Ling, Y. T., Chen, X.-Y., Chan, S.-T., Kwong, K. K., & Zheng, Y.-P. (2023). Success Rate of Transcranial Doppler Scanning of Cerebral Arteries at Different Transtemporal Windows in Healthy Elderly Individuals. *Ultrasound in medicine & biology*, *49*(2), 588-598.

Chandra, A., Li, W. A., Stone, C. R., Geng, X., & Ding, Y. (2017). The cerebral circulation and cerebrovascular disease I: Anatomy. *Brain circulation*, *3*(2), 45.

Chobanian, A. V. (2003). National heart, lung, and blood institute joint national committee on prevention, detection, evaluation, and treatment of high blood pressure; national high blood pressure education program coordinating committee. The seventh report of the joint national committee on prevention, detection, evaluation, and treatment of high blood pressure: the JNC 7 report. *Jama*, *289*, 2560-2572.

Cruz-Flores, S., Rabinstein, A., Biller, J., Elkind, M. S., Griffith, P., Gorelick, P. B., Howard, G., Leira, E. C., Morgenstern, L. B., & Ovbiagele, B. (2011). Racial-ethnic disparities in stroke care: the American experience: a statement for healthcare professionals from the American Heart Association/American Stroke Association. *Stroke*, *42*(7), 2091-2116.

Davenport, M. S., Perazella, M. A., Yee, J., Dillman, J. R., Fine, D., McDonald, R. J., Rodby, R. A., Wang, C. L., & Weinreb, J. C. (2020). Use of intravenous iodinated contrast media in patients with kidney disease: consensus statements from the American College of Radiology and the National Kidney Foundation. *Radiology*, *294*(3), 660-668.

De Caro, J., Ciacciarelli, A., Tessitore, A., Buonomo, O., Calzoni, A., Francalanza, I., Dell'Aera, C., Cosenza, D., Currò, C. T., & Granata, F. (2021). Variants of the circle of Willis in ischemic stroke patients. *Journal of neurology*, 1-9.

de Galiza Barbosa, F., Delso, G., Ter Voert, E., Huellner, M., Herrmann, K., & Veit-Haibach, P. (2016). Multi-technique hybrid imaging in PET/CT and PET/MR: what does the future hold? *Clinical radiology*, *71*(7), 660-672.

De Silva, K. R. D., Silva, R., Gunasekera, W. L., & Jayesekera, R. (2009). Prevalence of typical circle of Willis and the variation in the anterior communicating artery: A study of a Sri Lankan population. *Annals of Indian Academy of Neurology*, *12*(3), 157.

Deane, C. (2017). Doppler in Obstetrics: book by K Nicolaides, G Rizzo, K Hecher.

Delcker, A., & Turowski, B. (1997). Diagnostic value of three-dimensional transcranial contrast duplex sonography. *Journal of Neuroimaging*, *7*(3), 139-144.

Demené, C., Robin, J., Dizeux, A., Heiles, B., Pernot, M., Tanter, M., & Perren, F. (2021). Transcranial ultrafast ultrasound localization microscopy of brain vasculature in patients. *Nature biomedical engineering*, *5*(3), 219-228.

Deng, Z., Wang, Z., Yang, X., Luo, Q., & Gong, H. (2012). In vivo imaging of hemodynamics and oxygen metabolism in acute focal cerebral ischemic rats with laser speckle imaging and functional photoacoustic microscopy. *Journal of biomedical optics*, *17*(8), 081415-081415.

Dong, Y., Dobkin, B. H., Cen, S. Y., Wu, A. D., & Winstein, C. J. (2006). Motor cortex activation during treatment may predict therapeutic gains in paretic hand function after stroke. *Stroke*, *37*(6), 1552-1555.

Donkor, E. S. (2018). Stroke in the century: a snapshot of the burden, epidemiology, and quality of life. *Stroke research and treatment*, *2018*.

Easton, J. D., Saver, J. L., Albers, G. W., Alberts, M. J., Chaturvedi, S., Feldmann, E., Hatsukami, T. S., Higashida, R. T., Johnston, S. C., & Kidwell, C. S. (2009). Definition and evaluation of transient ischemic attack: a scientific statement for healthcare professionals from the American Heart Association/American Stroke Association Stroke Council; Council on Cardiovascular Surgery and Anesthesia; Council on Cardiovascular Radiology and Intervention; Council on Cardiovascular Nursing; and the Interdisciplinary Council on Peripheral Vascular Disease: the American Academy of Neurology affirms the value of this statement as an educational tool for neurologists. *Stroke*, *40*(6), 2276-2293.

Edelman, R. R., & Koktzoglou, I. (2019). Noncontrast MR angiography: an update. *Journal of Magnetic Resonance Imaging*, *49*(2), 355-373.

Eftekhar, B., Dadmehr, M., Ansari, S., Ghodsi, M., Nazparvar, B., & Ketabchi, E. (2006). Are the distributions of variations of circle of Willis different in different populations?–Results of an anatomical study and review of literature. *BMC neurology*, *6*(1), 1-9.

Ell, P. (2006). The contribution of PET/CT to improved patient management. *The British journal of radiology*, *79*(937), 32-36.

Feigin, V. L., Brainin, M., Norrving, B., Martins, S., Sacco, R. L., Hacke, W., Fisher, M., Pandian, J., & Lindsay, P. (2022). World Stroke Organization (WSO): global stroke fact sheet 2022. *International Journal of Stroke*, *17*(1), 18-29.

Feigin, V. L., Stark, B. A., Johnson, C. O., Roth, G. A., Bisignano, C., Abady, G. G., Abbasifard, M., Abbasi-Kangevari, M., Abd-Allah, F., & Abedi, V. (2021). Global, regional, and national burden of stroke and its risk factors, 1990–2019: a systematic analysis for the Global Burden of Disease Study 2019. *The Lancet Neurology*, *20*(10), 795-820.

Forgo, B., Tarnoki, A. D., Tarnoki, D. L., Kovacs, D. T., Szalontai, L., Persely, A., Hernyes, A., Szily, M., Littvay, L., & Medda, E. (2018). Are the Variants of the circle of Willis determined by genetic or environmental factors? Results of a twin study and review of the literature. *Twin Research and Human Genetics*, *21*(5), 384-393.

Fu, Q., Zhu, R., Song, J., Yang, H., & Chen, X. (2019). Photoacoustic imaging: contrast agents and their biomedical applications. *Advanced Materials*, *31*(6), 1805875.

FURUHATA, H. (1989). New Evolution of Transcranial Tomography (TCT) and Transcranial Color Dopplar Tomography (TCDT). *Neurosonology*, *2*(1), 8-15.

Gæde, P., Lund-Andersen, H., Parving, H.-H., & Pedersen, O. (2008). Effect of a multifactorial intervention on mortality in type 2 diabetes. *New England Journal of Medicine*, *358*(6), 580-591.

Garrigue, P., Giacomino, L., Bucci, C., Muzio, V., Filannino, M. A., Sabatier, F., Dignat-George, F., Pisano, P., & Guillet, B. (2016). Single photon emission computed tomography imaging of cerebral blood flow, blood–brain barrier disruption, and apoptosis time course after focal cerebral ischemia in rats. *International Journal of Stroke*, *11*(1), 117-126.

Gerriets, T., Postert, T., Goertler, M., Stolz, E., Schlachetzki, F., Sliwka, U., Seidel, G., Weber, S., & Kaps, M. (2000). DIAS I: duplex-sonographic assessment of the cerebrovascular status in acute stroke: a useful tool for future stroke trials. *Stroke*, *31*(10), 2342-2345.

Gray, C. S., Hildreth, A. J., Sandercock, P. A., O'Connell, J. E., Johnston, D. E., Cartlidge, N. E., Bamford, J. M., James, O. F., & Alberti, K. G. M. (2007). Glucose-potassium-insulin infusions in the management of post-stroke hyperglycaemia: the UK Glucose Insulin in Stroke Trial (GIST-UK). *The Lancet Neurology*, *6*(5), 397-406.

Grobner, T. (2006). Gadolinium–a specific trigger for the development of nephrogenic fibrosing dermopathy and nephrogenic systemic fibrosis? *Nephrology Dialysis Transplantation*, *21*(4), 1104-1108.

Hany, T. F., Schmidt, M., Hilfiker, P. R., Steiner, P., Bachmann, U., & Debatin, J. o. F. (1998). Optimization of contrast dosage for gadolinium-enhanced 3D MRA of the pulmonary and renal arteries. *Magnetic resonance imaging*, *16*(8), 901-906.

Harrington, D. P., Boxt, L. M., & Murray, P. D. (1982). Digital subtraction angiography: overview of technical principles. *American Journal of Roentgenology*, *139*(4), 781-786.

Heiss, W.-D. (2014). PET imaging in ischemic cerebrovascular disease: current status and future directions. *Neuroscience bulletin*, *30*, 713-732.

Hennerici, M., Rautenberg, W., Sitzer, G., & Schwartz, A. (1987). Transcranial Doppler ultrasound for the assessment of intracranial arterial flow velocity—Part 1. Examination technique and normal values. *Surgical neurology*, *27*(5), 439-448.

Hentsch, A., Aschauer, M. A., Balzer, J. O., Brossmann, J., Busch, H. P., Davis, K., Douek, P., Ebner, F., van Engelshoven, J. M., & Gregor, M. (2003). Gadobutrol-enhanced moving-table magnetic resonance angiography in patients with peripheral vascular disease: a prospective, multi-centre blinded comparison with digital subtraction angiography. *European radiology*, *13*, 2103-2114.

Hoksbergen, A. W., Majoie, C. B., Hulsmans, F.-J. H., & Legemate, D. A. (2003). Assessment of the collateral function of the circle of Willis: three-dimensional time-of-flight MR angiography compared with transcranial color-coded duplex sonography. *American Journal of Neuroradiology*, *24*(3), 456-462.

Holman, R. R., Paul, S. K., Bethel, M. A., Matthews, D. R., & Neil, H. A. W. (2008). 10-year follow-up of intensive glucose control in type 2 diabetes. *New England Journal of Medicine*, *359*(15), 1577-1589.

Hope, M. D., Hope, T. A., Zhu, C., Faraji, F., Haraldsson, H., Ordovas, K. G., & Saloner, D. (2015). Vascular imaging with ferumoxytol as a contrast agent. *AJR. American journal of roentgenology*, *205*(3), W366.

Hoskins, P. R., Martin, K., & Thrush, A. (2019). *Diagnostic ultrasound: physics and equipment*. CRC Press.

Huang, Q., & Zeng, Z. (2017). A review on real-time 3D ultrasound imaging technology. *BioMed research international*, *2017*.

Ivancevich, N. M., Pinton, G. F., Nicoletto, H. A., Bennett, E., Laskowitz, D. T., & Smith, S. W. (2008). Real-time 3-D contrast-enhanced transcranial ultrasound and aberration correction. *Ultrasound in medicine & biology*, *34*(9), 1387-1395.

Jadvar, H., & Colletti, P. M. (2014). Competitive advantage of PET/MRI. *European Journal of Radiology*, *83*(1), 84-94.

Kakou, M., Destrieux, C., & Velut, S. (2000). Microanatomy of the pericallosal arterial complex. *Journal of neurosurgery*, *93*(4), 667-675.

Kapoor, K., Singh, B., & Dewan, I. J. (2008). Variations in the configuration of the circle of Willis. *Anatomical science international*, *83*, 96-106.

Kapral, M. K., Fang, J., Hill, M. D., Silver, F., Richards, J., Jaigobin, C., & Cheung, A. M. (2005). Sex differences in stroke care and outcomes: results from the Registry of the Canadian Stroke Network. *Stroke*, *36*(4), 809-814.

Khare, S. (2016). Risk factors of transient ischemic attack: An overview. *Journal of mid-life health*, *7*(1), 2.

Kidwell, C. S., & Wintermark, M. (2008). Imaging of intracranial haemorrhage. *The Lancet Neurology*, *7*(3), 256-267.

Kleindorfer, D. O., Miller, R., Moomaw, C. J., Alwell, K., Broderick, J. P., Khoury, J., Woo, D., Flaherty, M. L., Zakaria, T., & Kissela, B. M. (2007). Designing a message for public education regarding stroke: does FAST capture enough stroke? *Stroke*, *38*(10), 2864-2868.

Kleindorfer, D. O., Towfighi, A., Chaturvedi, S., Cockroft, K. M., Gutierrez, J., Lombardi-Hill, D., Kamel, H., Kernan, W. N., Kittner, S. J., & Leira, E. C. (2021). 2021 guideline for the prevention of stroke in patients with stroke and transient ischemic attack: a guideline from the American Heart Association/American Stroke Association. *Stroke*, *52*(7), e364-e467.

Klötzsch, C., Bozzato, A., Lammers, G., Mull, M., Lennartz, B., & Noth, J. (1999). Three-dimensional transcranial color-coded sonography of cerebral aneurysms. *Stroke*, *30*(11), 2285-2290.

Klötzsch, C., Bozzato, A., Lammers, G., Mull, M., & Noth, J. (2002). Contrast-enhanced three-dimensional transcranial color-coded sonography of intracranial stenoses. *American Journal of Neuroradiology*, *23*(2), 208-212.

Kneipp, M., Turner, J., Hambauer, S., Krieg, S. M., Lehmberg, J., Lindauer, U., & Razansky, D. (2014). Functional real-time optoacoustic imaging of middle cerebral artery occlusion in mice. *PloS one*, *9*(4), e96118.

Kollmann, C. (2015). Diagnostic ultrasound imaging: Inside out. *Ultrasound in Medicine and Biology*, *41*(2), 622.

Kothari, R. U., Pancioli, A., Liu, T., Brott, T., & Broderick, J. (1999). Cincinnati prehospital stroke scale: reproducibility and validity. *Annals of emergency medicine*, *33*(4), 373-378.

Krabbe-Hartkamp, M. J., Van der Grond, J., De Leeuw, F., de Groot, J. C., Algra, A., Hillen, B., Breteler, M., & Mali, W. (1998). Circle of Willis: morphologic variation on three-dimensional time-of-flight MR angiograms. *Radiology*, *207*(1), 103-111.

Kukulska-Pawluczuk, B., Książkiewicz, B., & Nowaczewska, M. (2012). Imaging of spontaneous intracerebral hemorrhages by means of transcranial color-coded sonography. *European Journal of Radiology*, *81*(6), 1253-1258.

Laviña, B. (2016). Brain vascular imaging techniques. *International journal of molecular sciences*, *18*(1), 70.

Lell, M. M., Wildberger, J. E., Alkadhi, H., Damilakis, J., & Kachelriess, M. (2015). Evolution in computed tomography: the battle for speed and dose. *Investigative radiology*, *50*(9), 629-644.

Li, Q., Li, J., Lv, F., Li, K., Luo, T., & Xie, P. (2011). A multidetector CT angiography study of variations in the circle of Willis in a Chinese population. *Journal of Clinical Neuroscience*, *18*(3), 379-383.

Li, W., Tutton, S., Vu, A. T., Pierchala, L., Li, B. S., Lewis, J. M., Prasad, P. V., & Edelman, R. R. (2005). First‐pass contrast‐enhanced magnetic resonance angiography in humans using ferumoxytol, a novel ultrasmall superparamagnetic iron oxide (USPIO)‐based blood pool agent. *Journal of Magnetic Resonance Imaging: An Official Journal of the International Society for Magnetic Resonance in Medicine*, *21*(1), 46-52.

Li, X., & Zhang, X. (2019). Annual data set on national mortality surveillance 2018. In: Beijing: China Science and Technology Press.

Lindsey, B. D., Ivancevich, N. M., Light, E. D., Smith, S. W., Nicoletto, H. A., Bennett, E., & Laskowitz, D. T. (2009). The ultrasound brain helmet for 3D transcranial Doppler imaging. 2009 IEEE International Ultrasonics Symposium,

Logothetis, N. K. (2008). What we can do and what we cannot do with fMRI. *Nature*, *453*(7197), 869-878.

Lu, F.-M., & Yuan, Z. (2015). PET/SPECT molecular imaging in clinical neuroscience: recent advances in the investigation of CNS diseases. *Quantitative imaging in medicine and surgery*, *5*(3), 433.

Lu, Y., Hajifathalian, K., Ezzati, M., Woodward, M., Rimm, E. B., Danaei, G., & D'Este, C. (2014). Metabolic mediators of the eff ects of body-mass index, overweight, and obesity on coronary heart disease and stroke: a pooled analysis of 97 prospective cohorts with 1.8 million participants.

Lv, Q., Xu, G., Pan, Y., Liu, T., Liu, X., Miao, L., Chen, X., Jiang, L., Chen, J., & He, Y. (2021). Effect of acupuncture on neuroplasticity of stroke patients with motor dysfunction: a meta-analysis of fMRI studies. *Neural Plasticity*, *2021*, 1-10.

Maaly, M. A., & Ismail, A. A. (2011). Three dimensional magnetic resonance angiography of the circle of Willis: Anatomical variations in general Egyptian population. *The Egyptian journal of radiology and nuclear medicine*, *42*(3-4), 405-412.

Malek, A. M., Cushman, M., Lackland, D. T., Howard, G., & McClure, L. A. (2015). Secondhand smoke exposure and stroke: the reasons for geographic and racial differences in stroke (REGARDS) study. *American journal of preventive medicine*, *49*(6), e89-e97.

Matarin, M., Brown, W. M., Singleton, A., Hardy, J. A., & Meschia, J. F. (2008). Whole genome analyses suggest ischemic stroke and heart disease share an association with polymorphisms on chromosome 9p21. *Stroke*, *39*(5), 1586-1589.

Maulik, D. (2005). Sonographic color flow mapping: basic principles. In *Doppler Ultrasound in Obstetrics and Gynecology* (pp. 69-84). Springer.

Maurer, M., Shambal, S., Berg, D., Woydt, M., Hofmann, E., Georgiadis, D., Lindner, A., & Becker, G. (1998). Differentiation between intracerebral hemorrhage and ischemic stroke by transcranial color-coded duplex-sonography. *Stroke*, *29*(12), 2563-2567.

McKiernan, S., & Selmes, C. (2017). Transcranial colour‐coded duplex of the intracranial large arteries. *Sonography*, *4*(4), 156-165.

Members, W. G., Roger, V. L., Go, A. S., Lloyd-Jones, D. M., Benjamin, E. J., Berry, J. D., Borden, W. B., Bravata, D. M., Dai, S., & Ford, E. S. (2012). Heart disease and stroke statistics—2012 update: a report from the American Heart Association. *Circulation*, *125*(1), e2-e220.

Moraga, A., Gómez-Vallejo, V., Cuartero, M. I., Szczupak, B., San Sebastián, E., Markuerkiaga, I., Pradillo, J. M., Higuchi, M., Llop, J., & Moro, M. Á. (2016). Imaging the role of toll-like receptor 4 on cell proliferation and inflammation after cerebral ischemia by positron emission tomography. *Journal of Cerebral Blood Flow & Metabolism*, *36*(4), 702-708.

Mousa, A. E., Elrakhawy, M. M., & Zaher, A. A. (2013). Multimodal CT assessment of acute ischemic stroke. *The Egyptian journal of radiology and nuclear medicine*, *44*(1), 71-81.

Nordon David, G., & Rodrigues Junior, O. F. (2012). Variations in the brain circulation: the circle of Willis. *Braz. j. morphol. sci*, 243-247.

O'donnell, M. J., Xavier, D., Liu, L., Zhang, H., Chin, S. L., Rao-Melacini, P., Rangarajan, S., Islam, S., Pais, P., & McQueen, M. J. (2010). Risk factors for ischaemic and intracerebral haemorrhagic stroke in 22 countries (the INTERSTROKE study): a case-control study. *The Lancet*, *376*(9735), 112-123.

Olatunji, R. B., Ogbole, G. I., Atalabi, O. M., Adeyinka, A. O., Lagunju, I., Oyinlade, A., Ogun, O., Owolabi, M. O., Ogunseyinde, O. A., & Ogunniyi, A. (2015). Role of transcranial colour-coded duplex sonography in stroke management-Review article. *West African journal of ultrasound*, *16*(1), 33.

Ouwendijk, R., Kock, M. C., van Dijk, L. C., van Sambeek, M. R., Stijnen, T., & Hunink, M. M. (2006). Vessel wall calcifications at multi–detector row CT angiography in patients with peripheral arterial disease: effect on clinical utility and clinical predictors. *Radiology*, *241*(2), 603-608.

Ovesen, C., Christensen, A. F., Krieger, D. W., Rosenbaum, S., Havsteen, I., & Christensen, H. (2014). Time course of early postadmission hematoma expansion in spontaneous intracerebral hemorrhage. *Stroke*, *45*(4), 994-999.

Perlmutter, D., & Rhoton, A. L. (1978). Microsurgical anatomy of the distal anterior cerebral artery. *Journal of neurosurgery*, *49*(2), 204-228.

Philipp, L. R., McCracken, D. J., McCracken, C. E., Halani, S. H., Lovasik, B. P., Salehani, A. A., Boulter, J. H., Cawley, C. M., Grossberg, J. A., & Barrow, D. L. (2017). Comparison

between CTA and digital subtraction angiography in the diagnosis of ruptured aneurysms. *Neurosurgery*, *80*(5), 769-777.

Pinton, G., Aubry, J. F., Bossy, E., Muller, M., Pernot, M., & Tanter, M. (2012). Attenuation, scattering, and absorption of ultrasound in the skull bone. *Medical physics*, *39*(1), 299-307.

Prince, M. R. (1994). Gadolinium-enhanced MR aortography. *Radiology*, *191*(1), 155-164.

Rai, A. T., Hogg, J. P., Cline, B., & Hobbs, G. (2013). Cerebrovascular geometry in the anterior circulation: an analysis of diameter, length and the vessel taper. *Journal of neurointerventional surgery*, *5*(4), 371-375.

Rantakömi, S. H., Laukkanen, J. A., Sivenius, J., Kauhanen, J., & Kurl, S. (2013). Alcohol consumption and the risk of stroke among hypertensive and overweight men. *Journal of neurology*, *260*, 534-539.

Reeves, M. J., Fonarow, G. C., Zhao, X., Smith, E. E., & Schwamm, L. H. (2009). Quality of care in women with ischemic stroke in the GWTG program. *Stroke*, *40*(4), 1127-1133.

Reutern, G. (1991). Zerebraler Zirkulationsstillstand. Diagnostik mit der Dopplersonographie. *Dt Ärzteblatt*, *88*, 55-65.

Riggs, H. E., & Rupp, C. (1963). Variation in form of circle of Willis: the relation of the variations to collateral circulation: anatomic analysis. *Archives of Neurology*, *8*(1), 8-14.

Rosner, J., Reddy, V., & Lui, F. (2018). Neuroanatomy, circle of Willis.

Ryu, J., & Kamata, S.-i. (2021). An efficient computational algorithm for Hausdorff distance based on points-ruling-out and systematic random sampling. *Pattern Recognition*, *114*, 107857.

Sabarudin, A., Subramaniam, C., & Sun, Z. (2014). Cerebral CT angiography and CT perfusion in acute stroke detection: a systematic review of diagnostic value. *Quantitative imaging in medicine and surgery*, *4*(4), 282.

Sacco, R. L., Kasner, S. E., Broderick, J. P., Caplan, L. R., Connors, J., Culebras, A., Elkind, M. S., George, M. G., Hamdan, A. D., & Higashida, R. T. (2013). An updated definition of stroke for the 21st century: a statement for healthcare professionals from the American Heart Association/American Stroke Association. *Stroke*, *44*(7), 2064-2089.

Santamarina Pérez, E., Delgado-Mederos, R., Rubiera, M., Delgado, P., Ribó, M., Maisterra, O., Ortega, G., Alvarez-Sabin, J., & Molina, C. A. (2009). Transcranial duplex sonography for monitoring hyperacute intracerebral hemorrhage. *Stroke*, *40*(3), 987-990.

Sarkar, S., Ghosh, S., Ghosh, S. K., & Collier, A. (2007). Role of transcranial Doppler ultrasonography in stroke. *Postgraduate Medical Journal*, *83*(985), 683-689.

Schminke, U., Motsch, L., von Smekal, U., Griewing, B., & Kessler, C. (2000). Three-Dimensional Transcranial Color-Coded Sonographyforthe Examination of the Arteries of the Circle of Willis. *Journal of Neuroimaging*, *10*(3), 173-176.

Schöder, H., Erdi, Y. E., Larson, S. M., & Yeung, H. W. (2003). PET/CT: a new imaging technology in nuclear medicine. *European journal of nuclear medicine and molecular imaging*, *30*, 1419-1437.

Schöning, M., Grunert, D., & Stier, B. (1988). Transkranielle real-time-sonographie bei Kindern und Jugendlichen, Ultraschallanatomie des Gehirns. *Ultraschall in der Medizin*, *9*(06), 286-292.

Seidel, G., Kaps, M., & Dorndorf, W. (1993). Transcranial color-coded duplex sonography of intracerebral hematomas in adults. *Stroke*, *24*(10), 1519-1527.

Seshadri, S., Beiser, A., Pikula, A., Himali, J. J., Kelly-Hayes, M., Debette, S., DeStefano, A. L., Romero, J. R., Kase, C. S., & Wolf, P. A. (2010). Parental occurrence of stroke and risk of stroke in their children: the Framingham study. *Circulation*, *121*(11), 1304-1312.

Stansbury, J. P., Jia, H., Williams, L. S., Vogel, W. B., & Duncan, P. W. (2005). Ethnic disparities in stroke: epidemiology, acute care, and postacute outcomes. *Stroke*, *36*(2), 374-386.

Strazzullo, P., D'Elia, L., Kandala, N.-B., & Cappuccio, F. P. (2009). Salt intake, stroke, and cardiovascular disease: meta-analysis of prospective studies. *Bmj*, *339*.

Sui, X., Lavie, C. J., Hooker, S. P., Lee, D.-C., Colabianchi, N., Lee, C.-D., & Blair, S. N. (2011). A prospective study of fasting plasma glucose and risk of stroke in asymptomatic men. Mayo Clinic Proceedings,

Suk, S.-H., Sacco, R. L., Boden-Albala, B., Cheun, J. F., Pittman, J. G., Elkind, M. S., & Paik, M. C. (2003). Abdominal obesity and risk of ischemic stroke: the Northern Manhattan Stroke Study. *Stroke*, *34*(7), 1586-1592.

Tang, S.-C., Jeng, J.-S., Yip, P.-K., Lu, C.-J., Hwang, B.-S., Lin, W.-H., & Liu, H.-M. (2005). Transcranial color-coded sonography for the detection of middle cerebral artery stenosis. *Journal of ultrasound in medicine*, *24*(4), 451-457.

Tanoue, S., Kiyosue, H., Kenai, H., Nakamura, T., Yamashita, M., & Mori, H. (2000). Three-dimensional reconstructed images after rotational angiography in the evaluation of intracranial aneurysms: surgical correlation. *Neurosurgery*, *47*(4), 866-871.

Thun, M. J., Apicella, L. F., & Henley, S. J. (2000). Smoking vs other risk factors as the cause of smoking-attributable deaths: confounding in the courtroom. *Jama*, *284*(6), 706-712.

US-FDA. (2007). Gadolinium-based contrast agents for magnetic resonance imaging (marketed as Magnevist, MultiHance, Omniscan, OptiMARK, ProHance). *Rockville, MD: FDA*.

van Seeters, T., Hendrikse, J., Biessels, G. J., Velthuis, B. K., Mali, W. P., Kappelle, L. J., van der Graaf, Y., & Group, S. S. (2015). Completeness of the circle of Willis and risk of ischemic stroke in patients without cerebrovascular disease. *Neuroradiology*, *57*, 1247-1251.

Virani, S. S., Alonso, A., Aparicio, H. J., Benjamin, E. J., Bittencourt, M. S., Callaway, C. W., Carson, A. P., Chamberlain, A. M., Cheng, S., & Delling, F. N. (2021). Heart disease and stroke statistics-2021 update: a report from the American Heart Association. *Circulation*, *143*(8), CIR0000000000000950.

Vrselja, Z., Brkic, H., Mrdenovic, S., Radic, R., & Curic, G. (2014). Function of circle of Willis. *Journal of Cerebral Blood Flow & Metabolism*, *34*(4), 578-584.

Wang, Y.-J., Li, Z.-X., Gu, H.-Q., Zhai, Y., Jiang, Y., Zhao, X.-Q., Wang, Y.-L., Yang, X., Wang, C.-J., & Meng, X. (2020). China stroke statistics 2019: a report from the National center for healthcare quality management in neurological diseases, China national clinical research center for neurological diseases, the Chinese stroke association, National center for chronic and non-communicable disease control and prevention, Chinese center for disease control and prevention and Institute for global neuroscience and stroke collaborations. *Stroke and vascular neurology*, *5*(3).

Wannamethee, S. G., & Shaper, A. G. (1996). Patterns of alcohol intake and risk of stroke in middle-aged British men. *Stroke*, *27*(6), 1033-1039.

Ward, N., Brown, M., Thompson, A., & Frackowiak, R. (2003). Neural correlates of motor recovery after stroke: a longitudinal fMRI study. *Brain*, *126*(11), 2476-2496.

Weisstein, E. W. (2003). Rotation matrix. *https://mathworld. wolfram. com/*.

Wheaton, A. J., & Miyazaki, M. (2012). Non‐contrast enhanced MR angiography: physical principles. *Journal of Magnetic Resonance Imaging*, *36*(2), 286-304.

Xi, G., Keep, R. F., & Hoff, J. T. (2006). Mechanisms of brain injury after intracerebral haemorrhage. *The Lancet Neurology*, *5*(1), 53-63.

Xing, C.-Y., Tarumi, T., Liu, J., Zhang, Y., Turner, M., Riley, J., Tinajero, C. D., Yuan, L.-J., & Zhang, R. (2017). Distribution of cardiac output to the brain across the adult lifespan. *Journal of Cerebral Blood Flow & Metabolism*, *37*(8), 2848-2856.

Xu, M., & Wang, L. V. (2006). Photoacoustic imaging in biomedicine. *Review of scientific instruments*, *77*(4).

Yang, X., Chen, Y.-H., Xia, F., & Sawan, M. (2021). Photoacoustic imaging for monitoring of stroke diseases: A review. *Photoacoustics*, *23*, 100287.

Ye, Z.-G. (2008). *Handbook of advanced dielectric, piezoelectric and ferroelectric materials: Synthesis, properties and applications*. Elsevier.

Yen, J. T., Steinberg, J. P., & Smith, S. W. (2000). Sparse 2-D array design for real time rectilinear volumetric imaging. *IEEE transactions on ultrasonics, ferroelectrics, and frequency control*, *47*(1), 93-110.

Zhang, D., He, F., Han, S., Zou, L., Wu, Y., & Chen, Y. (2017). An efficient approach to directly compute the exact Hausdorff distance for 3D point sets. *Integrated Computer-Aided Engineering*, *24*(3), 261-277.

Zhou, C., Yuan, C., Li, R., Wang, W., Li, C., Zhao, X., & Collaborators, C.-I. S. (2018). Association Between Incomplete Circle of Willis and Carotid Vulnerable Atherosclerotic Plaques: A Chinese Atherosclerosis Risk Evaluation Study. *Arteriosclerosis, thrombosis, and vascular biology*, *38*(11), 2744-2749.

Zipper, S. G., & Stolz, E. (2002). Clinical application of transcranial colour-coded duplex sonography--a review. *European Journal of Neurology*, *9*(1), 1-8.